Electromagnetic modeling and imaging of damages of fiber-reinforced composite laminates

Zicheng Liu

▶ **To cite this version:**

Zicheng Liu. Electromagnetic modeling and imaging of damages of fiber-reinforced composite laminates. Electromagnetism. Université Paris Saclay (COmUE), 2017. English. NNT : 2017SACLS332 . tel-03411098

HAL Id: tel-03411098

https://theses.hal.science/tel-03411098v1

Submitted on 2 Nov 2021

HAL is a multi-disciplinary open access archive for the deposit and dissemination of scientific research documents, whether they are published or not. The documents may come from teaching and research institutions in France or abroad, or from public or private research centers.

L'archive ouverte pluridisciplinaire **HAL**, est destinée au dépôt et à la diffusion de documents scientifiques de niveau recherche, publiés ou non, émanant des établissements d'enseignement et de recherche français ou étrangers, des laboratoires publics ou privés.

université PARIS-SACLAY

NNT : 2017SACLS332

Thèse de doctorat

UNIVERSITÉ PARIS SUD
Comprendre le monde, construire l'avenir

Electromagnetic modeling and imaging of damages of fiber-reinforced composite laminates

Thèse de doctorat de l'Université Paris-Saclay
préparée à Université Paris-Sud

École doctorale n°580 Sciences et Technologies de l'Information et de la Communication (STIC)
Spécialité de doctorat : Traitement du Signal et des Images

Thèse présentée et soutenue à Gif-sur-Yvette, 3 octobre 2017, par

Zicheng Liu

Composition du Jury :

André Nicolet Professeur, Université de Marseille	Président
Amélie Litman Maître de Conférences, Université de Marseille	Rapportrice
Olivier Dazel Professeur, Université du Maine	Rapporteur
Sonia Fliss Enseignante-Chercheure, ENSTA	Examinatrice
Philippe Lalanne Directeur de recherche, CNRS	Examinateur
Jean-Philippe Groby Chargé de recherche, CNRS	Examinateur
Dominique Lesselier Directeur de recherche, CNRS	Directeur de thèse
Edouard Demaldent Ingénieur de recherche, CEA LIST	Invité
Yu Zhong Senior scientist, A*STAR Singapour	Invité

Acknowledgements

I wish to express my sincere appreciation to my supervisor Dr. Dominique Lesselier, Directeur de Recherche, Centre National de la Recherche Scientifique (CNRS), for leading me to the electromagnetic area. My research view gets widely broadened during the PhD years which should thanks to communication opportunities strongly supported by Dr. Lesselier. This appreciation is also for many helps and cares on my private life.

I also would like to give my many thanks to my co-supervisor Dr. Yu Zhong, now at the Institute of High Performance Computing, A*STAR, Singapore, for smart suggestions and deep discussions on the research direction, technical details and paper manuscripts. My warm thanks are given to my colleague and friend Changyou Li, who is now at Northwestern Polytechnical University. This thesis is in succession of his works. Thanks to him for providing me a good starting point and the very much help in these three years.

During the days at the Laboratoire des signaux et systèmes (L2S), I have been feeling really lucky to study in the same office with nice colleagues Hidayet Zaimaga who encouraged me to open myself and communicate with international friends, and Wajih Ben Abdallah who saved me a lot from language problems. I thank them a lot for the precious friendships. I am grateful to Dr. Marc Lambert, Dr. Vincent Lescarret and Mr Djibrilla Adamou for sharing interesting things to me on the way to our delicious CESFO restaurant.

I also wish to express thanks to my Chinese friends Xiang Liu, Xi Cheng, Pingping Ding, Caifang Cai and Jian Song at L2S, Yanpei Liu at Institut des Sciences des Plantes de Paris-Saclay (IPS2), Zhan Wang at Laboratoire de Recherche en Informatique (LRI), and Yonghao Chen at Institut de Physique Nucléaire (IPN). They have accompanied me and brought me happiness and help in these three years.

I would like to thank Dr. Sonia Fliss, Dr. Philippe Lalanne, Dr. Jean-Philippe Groby and Professor André Nicolet for serving as my jury members, Dr. Amélie Litman and Professor Olivier Dazel as referees, Dr. Edouard Demaldent and Dr Yu Zhong as invited members.

My great appreciation goes to my parents, wife, brother and sister for their never-ending love and confidence.

Résumé et introduction en Français

Résumé

La modélisation rapide et l'imagerie haute résolution des défauts dans les stratifiés multi-couches renforcés par des fibres sont l'objet de l'attention des travaux de cette thèse. On suppose, ce qui est reconnu comme une certaine approximation de la réalité, que chaque couche du stratifié est composée de fibres cylindriques circulaires périodiquement placées dans une dalle homogène. Les orientations des fibres dans les couches adjacentes sont limitées dans le cas considéré à être identiques, le cas d'orientations différentes restant à considérer plus avant (en s'appuyant sur les présents travaux et des travaux proches qui ont été menés au laboratoire). La modélisation des stratifiés monocouches avec des fibres qui peuvent être déplacées, qui peuvent être manquantes, ou qui peuvent aussi être rétrécies (moindres rayons) ou élargies (rayons plus grands) voire aussi présenter des inclusions en leur sein ou dans la matrice les contenant, est le sujet d'intérêt au départ. En raison de tels défauts, la périodicité de la structure est détruite et les méthodes développées pour des structures périodiques deviennent inapplicables de manière directe. La méthodologie dite "Supercell" ou super-cellule fournit une structure périodique fictive, de sorte que la solution de champ électromagnétique partout dans l'espace peut être modélisée avec précision, à condition que ladite super-cellule soit suffisamment grande. Cependant, l'efficacité de l'approche basée sur cette super-cellule n'est pas garantie en raison de sa grande taille possible. Par conséquent, une approche alternative basée sur une théorie d'équivalence est mise en œuvre, où les défauts sont équivalents électromagnétiquement à des sources à l'intérieur des fibres initialement intactes, et la solution résulte d'une sommation des réponses vis-à-vis de l'onde incidente et de ces sources équivalentes. L'extension des travaux pour les stratifiés monocouches à ceux pour des multicouches est facilement réalisée avec la méthode basée sur la matrice de diffusion (matrice S). Les champs sont développés en ondes planaires, et les coefficients des ces développements sont obtenus à partir d'un ensemble d'équations linéaires établies pour les matrices S. Puis les valeurs du champ dans l'ensemble de l'espace suivent le calcul de ces développements. La fonction de Green est

construite grâce à une méthode de balayage de réseau ("array scanning method"), dans laquelle des sources fictives sont fabriquées afin de produire une distribution de champ quasi périodique. En analysant l'excitation du réseau source avec des méthodes basées sur le théorème de Floquet, la solution suit une intégration de Sommerfeld, à travers de laquelle les effets des sources fictives sont annulés. Sur la base de la théorie de l'équivalence, l'emplacement des dommages se retrouve par recherche de sources équivalentes. Avec plusieurs sources et récepteurs en cours d'utilisation, quatre algorithmes de reconstruction, comprenant une solution moindres carrés, une solution "basic matching pursuit", une solution du type MUSIC, et une approche itérative explorant la parcimonie conjointe de la solution désirée permettent de déterminer les indices des fibres endommagées. Divers résultats numériques illustrent la disponibilité et la précision de l'approche de la modélisation et des performances d'imagerie haute résolution. On s'attend à ce que les travaux réalisés enrichissent la compréhension des comportements électromagnétiques en raison de défauts et de performances de détection avec plusieurs algorithmes d'imagerie.

Introduction et contexte de recherche

Les matériaux composites composés de deux constituants ou plus avec des propriétés physiques significativement différentes sont largement utilisés en raison des avantages que la partie individuelle ne peut apporter. Un bon exemple de composites, également celui concerné ici, est le matériau multicouche fibré, les caractères intéressants associés en termes de poids, de rigidité et de résistance à la corrosion augmentant l'application dans les industries de l'aéronautique et de l'automobile. Chaque couche du matériau concerné est composée d'une dalle diélectrique homogène et d'un agencement périodique de fibres cylindriques longues possédant les mêmes sections circulaires finies, toutes orientées dans la même direction et dont les matériaux constitutifs diffèrent de la matrice qu'ils renforcent. Le matériau fibreux pourrait être du verre, du graphite ou du métal, tandis que la dalle pourrait être en époxy ou en polyester. En prenant la dalle renforcée comme bloc de construction, une pile peut être construite en plaçant les dalles l'une sur l'autre et les orientations des fibres peuvent posséder, afin de fournir de la force et de la rigidité, plusieurs directions [1, 2]. Tester les piles ainsi fabriquées jusqu'à ce que le composite ait les propriétés souhaitées génère le stratifié utilisé. Une telle structure a un bon exemple en tant que pile de bois ("wood pile") où la pile est constituée de deux couches et les fibres incorporées dans chaque couche sont orthogonales à celles de la couche adjacente.

Les avantages des stratifiés peuvent être détruits par des dommages à l'intérieur, tels que des fibres manquantes, des fibres déplacées, rétrécies ou élargies, ou des inclusions

volumétriques et/ou des fissures. Ceux-ci peuvent se produire pendant la fabrication ou en service et leur détection est nécessaire afin d'éviter d'éventuels accidents et de prolonger la durée de vie utile. Cependant, les dommages sont généralement invisibles et, par conséquent, les tests non destructifs doivent détecter, localiser et, au mieux, les cartographier (en fournissant une image interprétable).

Sans recherche de l'exhaustivité, on peut distinguer un certain nombre de méthodes populaires. Les méthodes ultrasonores sont souvent appliquées pour la caractérisation des métaux et des alliages [3], mais en plus du milieu de couplage requis (tel que l'eau), une atténuation significative des composants à haute fréquence ou dans une région proche pourrait provoquer une mauvaise détection des défauts [4]. La thermographie infrarouge peut également être une bonne option, mais ne correspond pas aux matériaux à faibles pertes [5]. Les tests électromagnétiques semblent posséder un bon potentiel, à partir de l'exploration au MHz pour les composites à fibres de graphite [2], en micro-ondes et en ondes millimétriques voire au delà pour les cas à faibles pertes [6].

Comme les sources et les capteurs ne voient qu'une partie limitée du stratifié testé, la longueur de la fibre et la surface de la dalle sont idéalisées pour être infinies. En outre, pour réduire les difficultés du présent travail, les périodes des fibres et les orientations dans différentes couches sont choisies identiques, et en conséquence l'analyse peut être menée sur une structure périodique 2D, au lieu de la très demandeuse structure 3D. Tout d'abord, la modélisation électromagnétique informatique des stratifiés sains ou endommagés est nécessaire si l'on souhaite mieux comprendre les avantages et les inconvénients d'un contrôle, et de dériver des algorithmes d'imagerie efficaces pour l'utilisateur final.

Pour les structures intactes, de nombreuses recherches ont été entreprises. À grande échelle (longueur d'onde locale assez grande par rapport aux caractéristiques géométriques principales), la technique d'homogénéisation [7] est souvent appliquée en remplaçant l'objet étudié par des couches anisotropes homogènes planaires homogènes, le matériau de chaque couche étant alors caractérisé par les paramètres électromagnétiques d'un tenseur de moyenne, puis le milieu homogénéisé peut être analysé selon la méthode [8], qui induit un calcul stable de la réponse électromagnétique de tels composites à une source électrique active située soit à l'intérieur soit à l'extérieur. Cependant, alors que l'homogénéisation du stratifié monocouche peut se référer à [9], celui pour la structure multicouche reste un problème difficile à aborder.

À petite échelle (longueur d'onde locale assez petite par rapport à la géométrie), chaque couche dans le stratifié est périodique et l'unité élémentaire contient une fibre. Un modèle de champ de résonance complexe correspond. Les codes de force brute en différence finies temps-espace (FDTD) [10, 11] ou la méthode des éléments finis (FEM) [12] peuvent fournir

une solution en configurant le module mis en œuvre avec des conditions périodiques, mais la précision n'est pas nécessairement garantie. Et un choix judicieux de paramètres est nécessaire, alors que le poids du calcul peut être lourd. Dans [13], une solution efficace et précise est fournie par une approche de modélisation analytique et la bande efficace est très large. En se concentrant sur une couche de la structure, puisque la structure est périodique, le théorème de Floquet est facilement utilisé, et le problème se réduit au traitement d'une cellule unitaire. Grâce à l'analyse du couplage de champ dans ladite cellule unitaire, "fibre à fibre" et "fibre à dalle", le champ de la région entière suit la duplication quasi-périodique sur chaque couche et des matrices de diffraction bien établies lient les couches l'une à l'autre. On se réfèrera à des travaux pionniers en élasticité [14] dans lesquels les modes d'une plaque poreuse et les anomalies de Wood sont étudiés, des cristaux photoniques étant approchés de la même manière, par exemple [15], entre autres références.

En présence de dommages, il n'y a pas beaucoup de travaux qui ont été entrepris jusqu'ici. Comme la périodicité de la structure est détruite, en principe, toute la structure doit être modélisée. À grande échelle, puisque la longueur d'onde à l'intérieur de la dalle est habituellement, comme indiqué ci-dessus, beaucoup plus grande que la taille des fibres et qu'aucune résonance ne devrait apparaître à l'intérieur de la structure, les méthodes d'approximation valent la peine, par exemple, l'homogénéisation [7] et avec un degré plus élevé de précision, l'approximation du dipôle couplé [16]. À petite échelle, des solutions approchées peuvent être fournies par FDTD et FEM, mais l'objet étudié est alors remplacé par une troncature du stratifié avec tous les dommages inclus dans la zone centrale. En plus des paramètres complexes impliqués et du coût de calcul élevé possible, l'erreur de l'approximation est difficile à estimer puisqu'il n'y a pas de référence de vraie solution. Les contributions disponibles ont proposé une analyse précise du champ pour les distributions de fibres endommagées [17, 18] et les cristaux photoniques [19]. Cependant, les dommages sont encore limités à des fibres manquantes sans extension aux stratifiés. Par conséquent, l'élaboration d'une solution de champ rapide et précise pour des stratifiés endommagés est l'un des principaux objectifs de ce doctorat.

Le travail débute à partir du stratifié à une seule couche avec des fibres manquantes, déplacées, étendues, rétrécies, ainsi que des inclusions circulaires à l'intérieur de la fibre. Une nouvelle structure périodique auxiliaire est alors introduite, avec chaque unité étant la dénommée super-cellule, qui est en fait une idée très populaire [20, 21], incluant un nombre limité de fibres et les défauts dans la zone centrale. En élargissant la taille de la cellule dans la direction transverse ou le nombre d'éléments inclus (comme dit, les fibres sonores et endommagées), le champ calculé à l'intérieur, au-dessus et au-dessous (au moins assez proche de la surface stratifiée) de la région centrale de la super-cellule

devrait converger vers le vrai champ. Les conditions de convergence appropriées doivent naturellement être définies et respectées, en fonction des fréquences de fonctionnement, des illuminations, des caractéristiques du matériau et de la géométrie. Ici, les ondes TM et TE avec des illuminations par onde plane ou par ligne source sont considérées.

Cependant, avec des matériaux à faible perte ou sans perte et des ondes de basse fréquence (à nouveau à considérer en termes de longueur d'onde en fonction des caractéristiques géométriques/électriques de la structure), la taille de la zone tronquée doit être assez importante. Puisque la complexité de calcul est un cube de la taille de la super-cellule [22], des coûts de calcul importants doivent être supportés [23]. Ceci conduit à la demande d'une nouvelle approche de modélisation, qui devrait être non seulement précise, mais rapide, surtout si elle doit être utilisée dans la procédure d'imagerie, comme on le voit ci-dessous.

Avant d'accéder à cette étape, la fonction de Green, qui est la solution à une source ligne, est d'abord calculée, compte tenu du rôle de la nouvelle approche de modélisation et du modèle d'imagerie (test) suivi. La position de la source ligne peut être n'importe où dans l'espace entier et la méthode de balayage de réseau ("array scanning method") [24] est utilisée afin de surmonter le problème de singularité lorsque la source est à l'intérieur du stratifié. En bref, un réseau fictif de source de phases choisies est fabriqué de manière à ce que la distribution du champ devienne périodique. En analysant le réseau source avec des méthodes valides pour des structures périodiques, le champ suit en tant qu'intégration sur la première zone de Brillouin, à travers de laquelle les effets des sources fictives sont annulés [25].

Les analyses dans la nouvelle approche de modélisation sont pertinentes pour la structure intacte, au lieu de la troncature de la structure endommagée, en traitant les fibres endommagées comme des fibres saines mais avec des sources fictives équivalentes établies à l'intérieur, ce qui résulte en la vraie solution de champ en tant que somme des réponses de champ pour la source incidente extérieure et les sources équivalentes intérieures. Alors que le premier terme peut être calculé avec des méthodes comme celles pour les structures périodiques, le second est obtenu en tant que combinaison linéaire de solutions associées à un développement en ondes cylindriques ("cylindrical-wave-expansion" ou CWE) en supposant que le champ causé par une source interne soit exprimé en CWE. En outre, étant donné que la structure intacte et évidemment le champ incident sont connues, la solution de champ pour la source extérieure et celles pour les bases CWE peuvent être calculées à l'avance et stockées, tandis que les bases CWE sont traitées en suivant les mêmes procédures que pour la La fonction de Green. Une telle modélisation conduit à une analyse rapide

(peu de dépendance à l'égard des matériaux) et précise (aucune erreur d'approximation due à la troncature du stratifié).

Sans beaucoup de difficulté, l'extension à l'analyse de stratifiés à couches multicouches avec la théorie de l'équivalence peut être menée. En décomposant les champs au-dessus et au-dessous de la frontière de la dalle en ondes planes, les coefficients de développement pour les composantes réfléchies et les composantes incidentes (par rapport à ladite frontière) sont liés linéairement par la matrice de diffraction (matrice S) dont le calcul est réalisé par l'utilisation des conditions aux limites appropriées à la dalle. En analysant les comportements des réseaux de fibres avec la méthode multipolaire, la diffraction associée peut également être obtenue [26]. En fait, le réseau de fibres peut être traité comme une plaque plane en appliquant des coefficients PWE au-dessus et au-dessous de celle-ci satisfaisant la même matrice de diffraction. Ensuite, le schéma récursif, qui est largement utilisé dans l'analyse des plaques planaires en couches [8], peut être choisi pour obtenir tous les coefficients de développement ainsi que les valeurs des champs dans l'espace entier.

Sur la base des travaux réalisés sur la modélisation directe, des recherches ont été effectuées pour localiser les fibres endommagées. La théorie de l'équivalence offre en effet la possibilité de localiser différents types de défauts en recherchant des fibres incluant des sources équivalentes. Comme on ignore l'emplacement des vraies fibres endommagées, l'ensemble des fibres soumis à la détection doit être considéré comme un candidat, et un dictionnaire constitué de vecteurs de base (même rôle que la fonction de Green) est alors construit, chaque vecteur de base correspondant à une fibre. En plaçant un nombre fini de sources et de récepteurs au-dessus du stratifié pour collecter l'information, pour chaque source, les données collectées par les récepteurs donnent un vecteur de données et la matrice de données est obtenue en prenant tous les vecteurs de données comme colonnes. Ensuite, quatre algorithmes sont utilisés pour trouver l'indice des fibres endommagées à partir de la matrice de données.

(i) Une corruption des données peut se produire en raison de l'incertitude des paramètres matériels ou des positions géométriques d'une structure en cours de modélisation. Dans les cas avec de faibles corruptions, la minimisation d'une norme 2 du résidu des données (la différence entre les données saines et corrompues) conduit à la solution aux moindres carrés [27].

(ii) Via la séparation des vecteurs propres de la matrice de données en espaces de signal et de bruit, l'orthogonalité de l'espace de bruit aux vecteurs de base correspondant aux fibres endommagées donne lieu à l'estimateur MUSIC [28].

(iii) Trouver l'indice des fibres endommagées signifie sélectionner un sous-ensemble de vecteurs de base pour représenter les données. En projetant la matrice de données sur

chaque vecteur de base, le résidu est généré en supprimant la projection de la matrice de données et le vecteur de base atteignant le plus petit résidu est sélectionné. En répétant la procédure ci-dessus, mais en remplaçant la matrice de données par le résidu, une séquence de vecteurs de base est sélectionnée. Une telle méthodologie est appelée recherche de base (BMP) dans [29].

(iv) Les trois méthodes ci-dessus n'ont exploité que l'information de la matrice de données, mais rien sur le stratifié. Comme, en général, le nombre de fibres endommagées est faible, les éléments non nuls (correspondant aux fibres endommagées) de la solution souhaitée sont peu nombreux, c'est-à-dire que la solution est parcimonieuse. De plus, en raison de l'indépendance de l'emplacement des fibres endommagées avec les sources, les solutions par rapport à différentes sources doivent avoir un profil de parcimonie commun ou la même position d'éléments non nuls. Ce profil de parcimonie commun est appelé parcimonie conjointe [30]. Grâce à la mesure appropriée de la parcimonie conjointe [31], une fonction de pénalité est conçue, pour laquelle la corruption des données et le niveau de parcimonie de la solution souhaitée sont considérés simultanément. La solution consiste alors à minimiser (ou à maximiser en fonction de la pénalité positive ou négative) la fonction de pénalité.

Table of contents

List of figures

List of tables

Chapter 1

Introduction

1.1 Background

Composite materials consisting of two or more constituents with significantly different physical properties are widely used due to the preferred advantages which the individual part cannot support. A good example of composites, also the one concerned here, is the fibered multi-layered materials, the associated advantageous characters in terms of weight, stiffness and corrosion resistance increasing the application in aerospace and automotive industries. Each layer of the concerned material is composed of a homogeneous dielectric planar slab and a periodic arrangement of long cylindrical fibers with same finite circular sections, all orientated into the same direction and whose constitutive material differs from the slab which they are reinforcing. The fiber material might be glass, graphite, or metal, while the slab could be made of epoxy or polyester. Taking the reinforced slab as a building block, a stack can be built by pilling up the slabs one over the other and fiber orientations might change from slab to slab in order to provide strength and stiffness along multiple directions [1, 2]. The laminate in use is generated by pilling up the fabricated stacks until the composite is of the desired properties. Such structure has a good example as woodpiles, where the stack consists of two layers and the embedded fibers in each layer are perpendicular to those in adjacent layers.

The advantages of the laminates can be destroyed by damages inside, such as missing fibers, displaced, shrinked, expanded fibers, volumetric inclusions and/or cracks. They might happen during manufacture or in service and their detection is required to prevent possible accidents and prolong the service life. However, the damages are usually invisible and thus nondestructive testing is in need to detect, locate and at best map (image) them.

Without pursuit to exhaustivity, one can distinguish a number of popular methods. Ultrasonic methods are often applied for the characterization of metals and alloys [3], but

in addition to the required coupling medium (like water), significant attenuation of the high-frequency components or in near region might cause mis-detection of the defects [4]. Infrared thermography can also be a good option, however not fit with the low lossy medium [5]. Electromagnetic testing appears to have good potential, from MHz exploration for graphite-fiber composites [2] to microwave and millimeter wave one for low-loss cases [6].

Since sources and sensors view only a limited portion of the laminate under test, the fiber length and slab surface is idealized to be infinite. Moreover, to reduce the difficulties of the investigation, fiber periods and orientations in different layers are assumed to be the same in this thesis so that the analysis can be operated on the 2D periodic structure.

First, the computational electromagnetic modeling of both sound and damaged laminates is required if one wishes to better understand pluses and minuses of the testing, and to derive efficient imaging algorithms for the end-user.

For undamaged structures, plenty of investigations have been reported. At large scale (large enough local wavelength vs. main geometric features), the technique of homogenization [7] is often applied by replacing the investigated object as planar homogeneous anisotropic (due to the anisotropy of the fiber material, like graphite) layers while the material in each layer is characterized by the locally averaged tensor electromagnetic parameters, then the homogenized medium can be analyzed with the method in [8], which provides a stable calculation of the electromagnetic response of planar anisotropic composite panels to an active electric source located either inside or outside it. However, while the homogenization of the single-layer laminate can refer to [9], the one for the multilayer structure is still a difficult issue to tackle.

At small scale (small enough local wavelength vs. geometry), each layer in the laminate is taken periodic and the elementary unit contains a fiber. A complex resonance field pattern is expected in this case. Brute-force codes running finite-difference-time-domain (FDTD) [10, 11] or finite-element method (FEM) [12] can provide a solution by configuring the fabricated module with periodic conditions, but accuracy is not necessarily guaranteed and careful choice of parameters is needed, while the computational burden might be heavy. In [13], an efficient and accurate solution is provided by an analytical modeling approach and the effective band is proved broad. Focusing on one layer of the structure, since the structure is periodic, the Floquet theorem is readily used, and the problem reduces to treating an unit cell. Through analysis of field coupling within the unit cell, "fiber to fiber" and "fiber to slab", the field of the whole region follows the quasi-periodic duplication on each layer and the mapping by scattering matrices to other layers. So doing refers to

pioneering works in elasticity [14] wherein modes of a porous plate and Wood anomalies are studied, photonic crystals being approached likewise e.g. [15], among other references.

In the presence of damages, not many works appear to have been reported so far. Since the periodicity of the structure is destroyed, in principle, the whole structure has to be modeled. At large scale, since the wavelength inside the slab is usually, as indicated above, much larger than the fibers' size and no resonances are expected to arise inside the structure, approximation methods are worthwhile, e.g., homogenization [7] and with higher degree of accuracy the coupled dipole approximation [16]. At small scale, approximated solutions can be provided by FDTD and FEM, but the studied object is replaced by a truncation of the laminate with all damages included in the central area. In addition to the involved complex parameters and possible high computational cost, the approximated error is hard to estimate since one has no benchmark of the true solution. Available contributions have proposed accurate field analysis for damaged fiber distributions [17, 18] and photonic crystals [19]. However, the damages are yet limited to missing fibers with no extension to laminates. Hence, developing a fast and accurate field solution of damaged laminates becomes one of the main goals of this thesis.

The work starts from the single-layer laminate with missing, displaced, expanded, shrunk fibers, as well as circular inclusions inside the fiber. An auxiliary new periodic structure is introduced, with each unit the so-called supercell, in effect quite popular an idea, [20, 21] including a limited number of fibers and the defects within the central area. Enlarging the transverse cell size or the number of included elements (as said, both sound and damaged fibers), the field computed inside, above and below (at least close enough to the laminate surface) the central region of the supercell is expected to converge to the true field. Proper conditions of convergence should be set and met, depending upon operation frequencies, illuminations, material characteristics, and geometry. Here, TM electric and TE magnetic waves under the plane wave or line source illuminations are considered.

However, with low-loss or lossless materials and low-frequency waves (again to be looked at in terms of wavelength with respect to the geometric/electric features of the structure), the size of the truncated area is to be quite large. Since the computational complexity is a cube of the supercell size [22], high computational costs have to be borne [23]. This leads to the demand of new modeling approach, which should be no only accurate, but fast, especially if to be employed in the imaging procedure, as seen below.

Before going to that stage, the Green's function, which is the solution to a line source, is first calculated, in view of the role in the new modeling approach and the followed imaging (testing) model. While aligning along the fiber direction, the position of the line source can be anywhere in the whole space and the array scanning method [24] is

employed to overcome the singularity problem when the source is inside the laminate. In short, a fictitious phased source array is fabricated so that the field distribution becomes quasi-periodic again. Analyzing the source array with methods for periodic structures, the field follows as integration over the first Brillouin zone, through which the effects of the fictitious sources are canceled [25].

Analyses in the new modeling approach are relevant to the undamaged structure, instead of the truncation of the damaged one as one did in the supercell-based approach, by treating damaged fibers as sound ones with equivalent fictitious sources set inside, which results into the true field solution as a summation of field responses due to the exterior exciting source and to the inner equivalent ones. While the former can be computed with methods as for periodic structures, the latter is decomposed as a linear combination of solutions due to cylindrical-wave-expansion (CWE) bases assuming the field scattered by an inner source be expressed into CWE. Moreover, since the undamaged structure and obviously the incident field are known, the field solution for the exterior source and CWE bases can be computed in advance and stored, while the CWE bases are handled with the array scanning method following the same procedures as for the Green's function. Such modeling successfully avoids the test of field convergence and approximation errors in the supercell methodology and leads to a fast and accurate analysis.

Without much difficulty, the extension to the analysis of multilayer damaged laminates with the equivalence theory is made. Expanding fields above and below the slab boundary into plane waves, the expansion coefficients standing for the reflected components and incident ones (relative to the boundary), they are linearly linked by the scattering matrix, the computation of which is via the utilization of the slab boundary conditions. Analyzing the behaviors of fiber arrays with the multipole method, the associated scattering can be obtained as well [26]. In fact, the fiber array can be treated as a planar plane by enforcing PWE coefficients above and below it satisfying the same scattering matrix. Then, the recursive scheme, which is widely used in the analysis of layered planar plates [8], can be borrowed to retrieve all expansion coefficients as well as the field values in the whole space.

Based on the achieved works on direct modeling, numerical investigations are made to locate damaged fibers. The equivalence theory provides the possibility to locate various types of defects via seeking fibers including equivalent sources. As the location of the true damaged fibers is unknown, the whole set of fibers in detection should be considered as candidate, based on which a dictionary consisting of basis vectors (same role as the Green's function) is built, each basis vector corresponding to one fiber. Putting a finite number of sources and receivers above the laminate to collect the information, for each source, the

data collected by receivers yields a data vector and the data matrix is obtained by taking all data vectors as columns. Then, four algorithms are used to retrieve the index of damaged fibers from the data matrix.

(i) Data corruption might happen because of the uncertainty of the material parameters or the geometric positions of a structure being modeled. In cases with small corruptions, the minimization of the l_2-norm of the data residual (the difference between the neat data and corrupted one) leads to the least square solution [27].

(ii) Dividing the eigenvectors of the data matrix into signal and noise spaces, the orthogonality of the noise space to the basis vectors corresponding to damaged fibers gives rise to the multiple signal classification (MUSIC) estimator [28].

(iii) Finding the index of damaged fibers means selecting a subset of basis vectors to represent the data. Projecting the data matrix upon each basis vector, the residual is generated by removing the projection from the data matrix and the basis vector reaching the smallest residual is selected. Repeating the above procedure, but replacing the data matrix by the residual, a sequence of basis vectors are selected. Such methodology is named as basic matching pursuit (BMP) in [29].

(iv) The above three methods only exploited the information from the data matrix, but nothing about the laminate. Since, generally, the number of damaged fibers is small, the nonzero elements (corresponding to damaged fibers) of the desired solution are few, *i.e.* the solution is sparse. Also, due to the independence of the location of damaged fibers with sources, solutions with respect to different sources should have a common sparse profile, or the same position of nonzero elements. This common sparse profile is called joint sparsity in [30]. Through the proper measurement of the joint sparsity [31], a penalty function is designed, in which the data corruption and the sparsity level of the desired solution are both considered. Then the solution is the one minimizing (or maximizing depending on the positive or negative penalty) the penalty function.

1.2 Overview of the thesis

The thesis is divided into six chapters. The first one introduces the research background and the contributions of this thesis. Chapter 2 illustrates the supercell-based modeling approach on the single-layer laminate where the fundamental concepts including PWE/CWE expansions, Rayleigh identities and mode matching are illustrated in detail. The computation of the Green's function and the fast modeling approach based on equivalence theory are described in Chapter 3. This chapter helps to understand the way of treating defects as equivalent sources. The application of equivalence theory on multilayer laminates is carried

out in Chapter 4, while the computation of scattering matrices is introduced as a key factor. In Chapter 5, the imaging methodology with the four candidate reconstruction algorithms is interpreted and corresponding performances are illustrated by a set of numerical results. Chapter 6 summarizes the achieved works and sets forth some perspectives. Appendices provides supplementary materials, including the published/submitted contributions.

Chapter 2

Modeling of single-layer fiber-based laminate with supercell concept

Computational modeling of a composite laminate made of a homogeneous planar slab wherein circular cylindrical fibers are periodically embedded is carried out when various damages affect the structure and destroy the periodicity. Methods based on the Floquet theorem [13, 32] are inapplicable in direct manner. Supercell methodology yields a fictitious periodic structure, so as the electromagnetic field solution everywhere in space can be accurately modeled, provided the supercell be large enough. Damages include missing, displaced, shrunk and/or expanded fibers, and cylindrical homogeneous inclusions. Plane wave and line source illuminations are accounted for in both TE and TM polarizations. A set of simulations is proposed, with comparison to a standard finite-element approach, and modeling accuracy and efficiency are discussed. The works presented in this chapter have been published in [20, 21]

2.1 Configuration and formulation

The single-layer laminate is sandwiched between two homogeneous half spaces and taken as a homogeneous slab bounded by planes $z = a$ and $z = b$, and reinforced by periodically organized, infinitely-long, similarly-orientated (along y) circular cylindrical fibers, refer to Fig. 2.1 (with missing fibers depicted as well). Their embedding period, along the x direction, is d. Their common radius is c. Several types of damages, missing fibers, fiber displacement and shrinkage/expansion, cylindrically-modeled inclusions inside/outside fibers are to be considered (Fig. 2.2). Isotropy and linearity of all media are assumed.

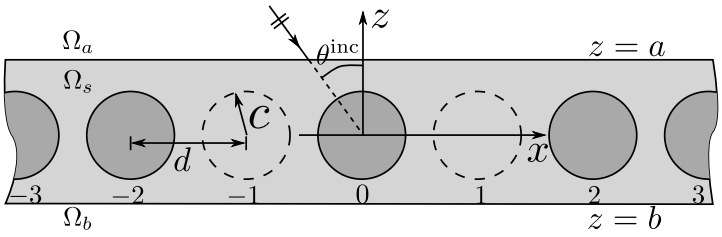

Fig. 2.1 A single-layer laminate with missing fibers and the plane-wave illumination.

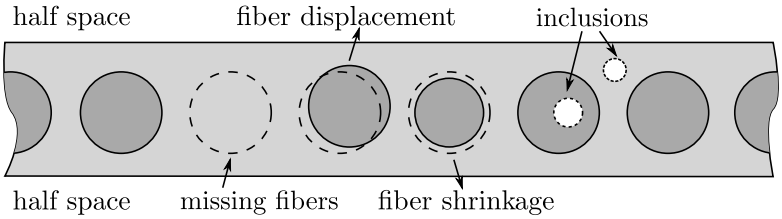

Fig. 2.2 Illustration of various potential damages.

Computational modeling of the field observed when the above laminate is illuminated by time-harmonic plane waves of $(x-z)$ plane of incidence or line sources orientated along y, with either TM or TE field polarization, is the aim of the study, this configuration leading to tackle as already indicated a two-dimensional scalar scattering problem.

Labelling fibers by integers as shown in Fig. 2.1, the whole space divides into the Ω_a region above the laminate, Ω_b below it, the slab Ω_s, and the cross-section Ω_l of the l-th fiber, $l \in \mathbb{Z}$. Each zone is with possibly complex-valued permittivity ϵ_j and permeability μ_j, $j = a, b, s, l$. $\epsilon_l = \epsilon_s$ and $\mu_l = \mu_s$ if the l-th fiber is missing. Relative values are denoted as ϵ_{rj} and μ_{rj}. The wavenumber in each region is k_j. The TM electric field has a y-component only, the same with the TE magnetic field.

Time dependence $e^{-i\omega t}$ is implied, ω angular frequency, i imaginary unit. Let the wave vector of an obliquely incident plane wave be $\mathbf{k}^{inc} = k_a^x \hat{x} - k_a^z \hat{z}$, where $k_a^x = k_a \sin\theta^{inc}$ is the x-component of k_a, θ^{inc} angle of incidence, $k_a^z = \sqrt{k_a^2 - (k_a^x)^2}$ in top Riemann sheet ($\Im(k_a^z) > 0$) [33], $\hat{x}$ and $\hat{z}$ unit vectors. The incident field at observation point $\mathbf{r}$ or (x,z) reads as $V^{inc}(\mathbf{r}) = A^{inc} e^{i\left[k_a^x x - k_a^z (z-a)\right]}$ where V stands for the y-component of the TM electric field or of the TE magnetic one, A^{inc} as the amplitude of the incident wave taken as unity.

As for the incident field due to a line source, it reads as $V^{inc}(\mathbf{r}, \mathbf{o}_s) = H_0^{(1)}(k_a |\mathbf{r} - \mathbf{o}_s|)/4i$, which is the solution to the Helmholtz equation

$$(\nabla^2 + k_a^2) V^{inc}(\mathbf{r}) = \delta(\mathbf{r} - \mathbf{o}_s). \tag{2.1}$$

$H_0^{(1)}$ is the first-kind 0-th mode Hankel function and $\mathbf{o}_s$ denotes the source position.

2.2 Supercell concept

The undamaged laminate is periodic along the transverse direction x. This periodicity is destroyed by occurrence of damages and methods dealing with periodic structures are not directly applicable. To still apply them, the concept of supercell is introduced. The original supercell is obtained by truncating the laminate such that all damages are covered and located in its middle area. Repeating it to infinity on either side along the line connecting the centers of the fibers, a new (though fictitious) periodic structure is established. The new units, like the regions bounded by dashed lines in Fig. 2.3, are the supercells. Then, modeling approaches dedicated to periodic structures can be applied again [20, 23].

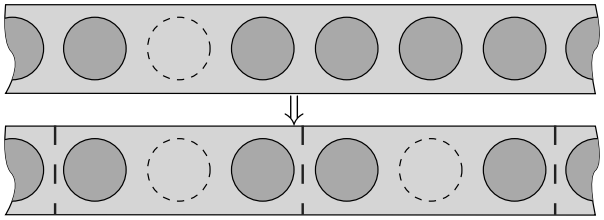

Fig. 2.3 Supercell periodic structure with missing fiber, number of included fibers $L = 3$.

It is expected that the field associated with the truly damaged laminate follows from proper enlargement of the supercell size, *i.e.*, by increasing the number L of fibers included within the supercells.

Physically speaking, in a testing procedure fields scattered near the damaged zone are collected, and if the central supercell is wide enough, impact of the fictitiously introduced damages outside it should be small on those sources that are effectively induced within this central part, and consequently on such scattered fields. This should be quite accurate when the source itself is local, like a line source set somewhere above the central supercell, a plane wave which illuminates the structure to infinity being a priori less favorable.

2.3 Field expansions

The modeling theory is based on the proper representations of fields everywhere. To facilitate the field matching on boundaries in section 2.4, the field near slab and fibers is expressed in plane-wave expansions (PWEs) and cylindrical-wave expansions (CWEs), respectively. Thus the derivation of PWE and CWE expressions is illustrated below, where the periodicity of the field distribution gives rise to fields quantified by discrete-Fourier-transformation (DFT) series [34].

2.3.1 Plane-wave expansion

The period of the fabricated periodic structure $D = Ld$. From the Floquet theorem, we have $V(\mathbf{r} + uD\hat{x}) = V(\mathbf{r})e^{ik_a^x uD}$. Let $V(\mathbf{r}) = e^{ik_a^x x}P(\mathbf{r})$, then $P(\mathbf{r})$ is a periodic function with period $D\hat{x}$. Reading the DFT of $P(\mathbf{r})$ as

$$P(\mathbf{r}) = \sum_{p\in\mathbb{Z}} h_p(z)e^{ip\frac{2\pi}{D}x}, \tag{2.2}$$

$V(\mathbf{r})$ has the reformulation

$$V(\mathbf{r}) = \sum_{p\in\mathbb{Z}} h_p(z)e^{i\alpha_p x} \tag{2.3}$$

where $\alpha_p = k_a^x + p2\pi/D$. The Fourier series expansion indicates that the field is expressible in terms of an infinite number of traveling waves. Components with $\alpha_p > 0$ are forward traveling and all those with $\alpha_p < 0$ are backward traveling.

The substitution of (2.3) into the Helmholtz equation,

$$(\nabla^2 + k_j^2)V(\mathbf{r}) = 0, \tag{2.4}$$

$j = s$, b, or a, depending the position of $\mathbf{r}$ in Ω_s, Ω_f or Ω_a, leads to

$$\sum_{p\in\mathbb{Z}}\left[(\frac{\partial}{\partial z^2} + k_j^2 - \alpha_p^2)h_p(z)\right]e^{i\alpha_p x} = 0. \tag{2.5}$$

Thus $h_p(z)$ has the general solution

$$h_p(z) = f_p e^{-i\beta_p^j z} + g_p e^{i\beta_p^j z}. \tag{2.6}$$

Back to (2.3), V has the PWE expression

$$V(\mathbf{r}) = \sum_{p\in\mathbb{Z}}\left[f_p e^{-i\beta_p^j z} + g_p e^{i\beta_p^j z}\right]e^{i\alpha_p x}, \tag{2.7}$$

where $\beta_p^j = \sqrt{k_j^2 - \alpha_p^2}$ defined in the top Riemann sheet. f_p and g_p stand for upward and downward waves, respectively.

Note that the imaginary part of β_p^j is the attenuation constant. As $|p| \to \infty$, $h_p(z)$ would tends to zero and a proper truncation of the infinite series (2.7) can guarantee the high accuracy of the field solution. The approach to make this truncation is illustrated in subsection 2.7.1.

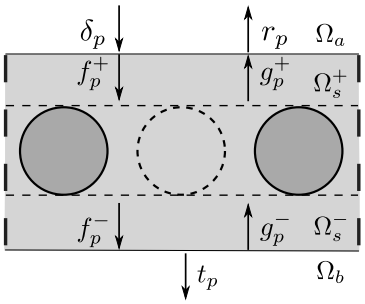

Fig. 2.4 Planar-wave-expansion coefficients for fields near slab boundaries.

Setting $r_p = g_p e^{i\beta_p^a a}$, $\delta_p = f_p e^{-i\beta_p^a a}$, (2.7) is written as

$$V(\mathbf{r}) = \sum_{p\in\mathbb{Z}} \left[\delta_p e^{-i\beta_p^a (z-a)} + r_p e^{i\beta_p^a (z-a)}\right] e^{i\alpha_p x}, \text{ for } \mathbf{r}\in\Omega_a \tag{2.8}$$

for the case with plane-wave-illumination. δ_p is the Kronecker delta function standing for the incident wave, and r_p are coefficients denoting the reflected wave. Likewise, see Fig. 2.4, other regions could be expanded in PWEs as

$$V(\mathbf{r}) = \sum_{p\in\mathbb{Z}} \left[f_p^+ e^{-i\beta_p^s z} + g_p^+ e^{i\beta_p^s z}\right] e^{i\alpha_p x}, \text{ for } \mathbf{r}\in\Omega_s^+ \tag{2.9a}$$

$$V(\mathbf{r}) = \sum_{p\in\mathbb{Z}} \left[f_p^- e^{-i\beta_p^s z} + g_p^- e^{i\beta_p^s z}\right] e^{i\alpha_p x}, \text{ for } \mathbf{r}\in\Omega_s^- \tag{2.9b}$$

$$V(\mathbf{r}) = \sum_{p\in\mathbb{Z}} t_p e^{i(\alpha_p x - \beta_p^b (z-b))}, \text{ for } \mathbf{r}\in\Omega_b. \tag{2.9c}$$

where signs + and − denote slices above the fiber array and below it. The downward component is not included in (2.9c) considering no illuminating wave from the bottom and the Sommerfeld radiation condition.

2.3.2 Cylindrical-wave expansion

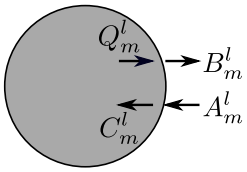

Fig. 2.5 Cylindrical-wave-expansion coefficients for fields around the fiber.

Another periodicity is exploited to express the field near fiber boundaries in CWEs. The field at $\mathbf{r}_l$, which is the relative position of $\mathbf{r}$ to $\mathbf{o}_l$, *i.e.*, $\mathbf{r}_l = \mathbf{r} - \mathbf{o}_l$, $\mathbf{o}_l$ the center of the l-th

fiber, enjoys the periodicity in angular dimension with period 2π. Assume (r_l, θ_l) are polar coordinates of $\mathbf{r}_l$, then $V(r_l, \theta_l + 2\pi) = V(r_l, \theta_l)$, based on which V can be represented by a DFT series

$$V(\mathbf{r}_l) = \sum_{m\in\mathbb{Z}} V_m(r_l) e^{im\theta_l}. \tag{2.10}$$

V_m being the Fourier coefficients satisfying the Helmholtz equation

$$(\nabla^2 + k_j^2) V_m(r_l) = 0, \tag{2.11}$$

$j = s$ for $\mathbf{r}_l \in \Omega_s$ and f for $\mathbf{r}_l \in \Omega_l$. The general solution [15] to (2.11) in polar coordinates is given by

$$V_m(r_l) = A_m^l J_m(k_s r_l) + B_m^l H_m^{(1)}(k_s r_l) \text{ for } \mathbf{r}_l \in \Omega_s, \tag{2.12a}$$
$$V_m(r_l) = C_m^l J_m(k_f r_l) + Q_m^l H_m^{(1)}(k_f r_l) \text{ for } \mathbf{r}_l \in \Omega_l, \tag{2.12b}$$

where J_m is the Bessel function of the m-th order and $H_m^{(1)}$ the first-kind Hankel function. Then the CWE expression of $V(\mathbf{r}_l)$ reads as

$$V(\mathbf{r}_l) = \sum_{m\in\mathbb{Z}} \left[A_m^l J_m(k_s r_l) + B_m^l H_m^{(1)}(k_s r_l)\right] e^{im\theta_l} \text{ for } \mathbf{r}_l \in \Omega_s, \tag{2.13a}$$
$$V(\mathbf{r}_l) = \sum_{m\in\mathbb{Z}} \left[C_m^l J_m(k_f r_l) + Q_m^l H_m^{(1)}(k_f r_l)\right] e^{im\theta_l} \text{ for } \mathbf{r}_l \in \Omega_l. \tag{2.13b}$$

While terms with J_m stand for incoming waves to the fiber center, $H_m^{(1)}$ are for outgoing components. Ones with coefficients B_m^l, Q_m^l are due to the reflection by the fiber and the inner (equivalent) source, respectively, and A_m^l, C_m^l denotes the incident wave upon the fiber and the transmitted one into the fiber. Letting $g_m^Z(k_s, \mathbf{r}_l) = Z_m(k_s r_l) e^{im\theta_l}$, (2.13) has the simpler form

$$V(\mathbf{r}_l) = \sum_{m\in\mathbb{Z}} \left[A_m^l g_m^J(k_s, \mathbf{r}_l) + B_m^l g_m^{H^{(1)}}(k_s, \mathbf{r}_l)\right] \text{ for } \mathbf{r}_l \in \Omega_s, \tag{2.14a}$$
$$V(\mathbf{r}_l) = \sum_{m\in\mathbb{Z}} \left[C_m^l g_m^J(k_f, \mathbf{r}_l) + Q_m^l g_m^{H^{(1)}}(k_s, \mathbf{r}_l)\right] \text{ for } \mathbf{r}_l \in \Omega_l. \tag{2.14b}$$

2.4 Analysis of missing fibers case with plane-wave illumination

To carry out the supercell-based analysis, the method in [20] is followed due to its high efficiency and accuracy. The illustration is detailed in the missing fibers case in this section and formulas made compatible to the other cases in section 2.5.

Fields are expressed in CWEs or PWEs in different regions as described in section 2.3. To get the full-field solution, the involved expansion coefficients, including r_p, t_p, $f_p^{\pm}$, $g_p^{\pm}$ and A_m^l, B_m^l, C_m^l, are to be computed via the utilization of the slab and fiber boundary conditions, Rayleigh identities and analyzing mutual scatterings between slab and fibers.

2.4.1 Mutual scatterings and matching fields on slab boundaries

The total field in region Ω_s is the sum of fields scattered by the slab boundaries and the whole set of fibers. As described above, field components with PWE coefficients f_p^+ and g_p^- stand for the field scattered by the upper and lower slab boundary, respectively. With the field scattered by the l-th fiber in the u-th supercell,

$$V_{l,u}^f(\mathbf{r}) = \sum_{m\in\mathbb{Z}} B_m^l g_m^{H^{(1)}}(k_s,(x_l-uD,z_l))e^{i\alpha_0 uD}, \tag{2.15}$$

where (x_l,z_l) are Cartesian coordinates of $\mathbf{r}_l$, the contribution from fibers is

$$V^f(\mathbf{r}) = \sum_{u\in\mathbb{Z}} e^{i\alpha_0 uD} \sum_{l\in\mathbb{L}}\sum_{m\in\mathbb{Z}} B_m^l g_m^{H^{(1)}}(k_s,(x_l-uD,z_l)). \tag{2.16}$$

$\mathbb{L}$ is the set of fiber indexes within the central supercell and the fact that $B_m^{l+uL} = B_m^l e^{i\alpha_0 uD}$ from the Floquet theorem is implied. Thus the total field in Ω_s has the expression

$$\begin{aligned} V(\mathbf{r}) = &\sum_{p\in\mathbb{Z}}\left[f_p^+ e^{-i\beta_p^s z} + g_p^- e^{i\beta_p^s z}\right]e^{i\alpha_p x} + \\ &\sum_{u\in\mathbb{Z}} e^{i\alpha_0 uD}\sum_{l\in\mathbb{L}}\sum_{m\in\mathbb{Z}} B_m^l g_m^{H^{(1)}}(k_s,(x_l-uD,z_l)),\ \ \mathbf{r}\in\Omega_s. \end{aligned} \tag{2.17}$$

However, (2.17) is in mixed form of PWE and CWE and not convenient for further operations. Thus a transformation between PWEs and CWEs is carried out.

To facilitate field matching on the slab boundaries, the field in the slab is expressed in full PWE form. Setting $K_{m,p}^{\pm} = 2(-i)^m e^{\pm im\theta_p}/(D\beta_p^s)$ and $\cos\theta_p = \alpha_p/k_s$, and applying

identity [35]

$$\sum_{u\in\mathbb{Z}} e^{i\alpha_0 uD} g_m^{H^{(1)}}(k_s,(x_l-uD,z_l)) = \sum_{p\in\mathbb{Z}} K_{m,p}^{\pm} e^{i\left(\alpha_p x_l \pm \beta_p^s z_l\right)}, \tag{2.18}$$

(2.17) can be rewritten as

$$V(\mathbf{r}) = \sum_{p\in\mathbb{Z}} \left[f_p^+ e^{-i\beta_p^s z} + g_p^- e^{i\beta_p^s z} \right] e^{i\alpha_p x} + \sum_{p\in\mathbb{Z}} \left(\sum_{m\in\mathbb{Z}} K_{m,p}^{\pm} F_m^p \right) e^{i\left(\alpha_p x \pm \beta_p^s z\right)}, \tag{2.19}$$

where $F_m^p = \sum_{l\in\mathbb{L}} B_m^l e^{-i\alpha_p l d}$ is the discrete Fourier transform of B_m^l, signs + and − corresponding to $z \geq 0$ and $z < 0$, respectively. Defining $X_p^{\pm} = \sum_{m\in\mathbb{Z}} K_{m,p}^{\pm} F_m^p$ and comparing the equation form with (2.9a) and (2.9b), two relations about PWE coefficients are obtained,

$$f_p^- = f_p^+ + X_p^-, \tag{2.20a}$$

$$g_p^+ = g_p^- + X_p^+, \tag{2.20b}$$

which indicate that the field incident upon the upper slab boundary in the slab is composed of the field reflected by the lower slab boundary and scattered by fibers, and vice versa.

Slab boundary conditions [33, 36] state that tangential components of electric and magnetic fields are continuous across the boundary, *i.e.*, $E_y^a|_{z=a} = E_y^{s+}|_{z=a}$, $H_x^a|_{z=a} = H_x^{s+}|_{z=a}$ for the upper boundary in TM case, where $E_y^a|_{z=a}$, $H_y^a|_{z=a}$ is the y-component of the electric and magnetic field strength along $z = a$ on the Ω_a side, respectively. Exchanging E and H, equations for the TE case are obtained. Boundary conditions for the lower boundary are similarly defined.

With PWE expressions of fields near upper and lower slab boundaries, four equations are obtained from the slab boundary conditions, as

$$\delta_p + r_p = X_p^+ e^{i\beta_p^s a} + g_p^- e^{i\beta_p^s a} + f_p^+ e^{-i\beta_p^s a}, \tag{2.21a}$$

$$t_p = X_p^- e^{-i\beta_p^s b} + g_p^- e^{i\beta_p^s b} + f_p^+ e^{-i\beta_p^s b}, \tag{2.21b}$$

$$w_p^a\left(-\delta_p + r_p\right) = w_p^s\left(X_p^+ e^{i\beta_p^s a} + g_p^- e^{i\beta_p^s a} - f_p^+ e^{-i\beta_p^s a}\right), \tag{2.21c}$$

$$-w_p^b t_p = w_p^s\left(-X_p^- e^{-i\beta_p^s b} + g_p^- e^{i\beta_p^s b} - f_p^+ e^{-i\beta_p^s b}\right), \tag{2.21d}$$

which yields r_p, t_p, f_p^+ and g_p^- as functions of $X_p^\pm$ as

$$\begin{aligned} g_p^- =&(w_p^s - w_p^b)\left\{(w_p^s + w_p^a)X_p^- e^{-i\beta_p^s(a+b)} + \right. \\ &\left.(w_p^s - w_p^a)X_p^+ e^{i\beta_p^s(a-b)} + 2w_p^a\delta_p e^{-i\beta_p^s b}\right\}/\Lambda_p, \end{aligned} \tag{2.22a}$$

$$\begin{aligned} f_p^+ =&\left\{(w_p^s - w_p^b)(w_p^s - w_p^a)X_p^- e^{i\beta_p^s(a-b)} + \right. \\ &\left.(w_p^s + w_p^b)(w_p^s - w_p^a)X_p^+ e^{i\beta_p^s(a+b)} + 2w_p^a(w_p^s + w_p^b)\delta_p e^{i\beta_p^s b}\right\}/\Lambda_p, \end{aligned} \tag{2.22b}$$

$$\begin{aligned} r_p =&\left\{2w_p^s(w_p^s - w_p^b)X_p^- e^{-i\beta_p^s b} + 2w_p^s(w_p^s + w_p^b)X_p^+ e^{i\beta_p^s b}\right. \\ &\left. + 2\delta_p\left[w_p^s(w_p^a - w_p^b)\cos(\beta_p^s\zeta) + i((w_p^s)^2 - w_p^a w_p^b)\sin(\beta_p^s\zeta)\right]\right\}/\Lambda_p, \end{aligned} \tag{2.22c}$$

$$t_p = \left\{4\delta_p w_p^a w_p^s + 2w_p^s(w_p^s + w_p^a)X_p^- e^{-i\beta_p^s a} + 2w_p^s(w_p^s - w_p^a)X_p^+ e^{i\beta_p^s a}\right\}/\Lambda_p, \tag{2.22d}$$

where $\zeta = a - b$, $\Lambda_p = 2w_p^s(w_p^a + w_p^b)\cos(\beta_p^s\zeta) - 2i((w_p^s)^2 + w_p^a w_p^b)\sin(\beta_p^s\zeta)$, $w_p^j = \beta_p^j/\mu_j$ (TM) and $w_p^j = \beta_p^j/\epsilon_j$ (TE). g_p^-, f_p^+, r_p and t_p have been expressed as functions of $X_p^\pm$ (or B_m^l). So it remains to get the B_m^l.

2.4.2 Rayleigh identities

B_m^l are coefficients of the field scattered by the l-th fiber, the solution of which is deduced from the combination of Rayleigh identities and fiber boundary conditions, as commonly used in the field analysis of photonic crystals [15].

From the Jacobi-Anger expansion,

$$e^{ir\cos\theta} = \sum_{m\in\mathbb{Z}} i^m J_m(r)e^{im\theta}, \tag{2.23}$$

(2.17) can be fully expressed in CWE as

$$\begin{aligned} V(\mathbf{r}) = &\sum_{m\in\mathbb{Z}} g_m^J(k_s, \mathbf{r}_l)\sum_{p\in\mathbb{Z}} e^{i\alpha_p ld}\left(J_{m,p}^+ f_p^{b+} + J_{m,p}^- f_p^{a-}\right) + \\ &\sum_{m\in\mathbb{Z}}\sum_{l\in\mathbb{L}} B_m^l \sum_{u\in\mathbb{Z}} e^{i\alpha_0 uD} g_m^{H^{(1)}}(k_s, (x_l - uD, z_l)), \end{aligned} \tag{2.24}$$

where $J_{m,p}^\pm = (i)^m\exp(\mp im\theta_p)$ and $\cos\theta_p = \alpha_p/k_s$. Applying the Graf's addition theorem (see Appendix A) on the second part of (2.24) with condition $r_l < d$, it can be reformulated

[23] as

$$\begin{aligned} V(\mathbf{r}) = &\sum_{m\in\mathbb{Z}} g_m^J(k_s,\mathbf{r}_l)\sum_{p\in\mathbb{Z}} e^{i\alpha_p ld}\left(J_{m,p}^{+} f_p^{b+} + J_{m,p}^{-} f_p^{a-}\right) \\ &+ \sum_{m\in\mathbb{Z}} g_m^J(k_s,\mathbf{r}_l)\sum_{j\in\mathbb{L}\setminus\{l\}}\sum_{n\in\mathbb{Z}} S_{m-n,j-l}^1 B_n^j \\ &+ \sum_{m\in\mathbb{Z}} g_m^J(k_s,\mathbf{r}_l)\sum_{j\in\mathbb{L}}\sum_{n\in\mathbb{Z}} S_{m-n,j-l}^2 B_n^j + \sum_{m\in\mathbb{Z}} g_m^{H^{(1)}}(k_s,\mathbf{r}_l) B_m^l. \end{aligned} \tag{2.25}$$

$S_{m-n,j-l}^1 = h_{m-n,j-l}^0$ and $S_{m-n,j-l}^2 = \sum_{u\in\mathbb{Z}\setminus\{0\}} h_{m-n,j-l}^u$, in which $h_{m-n,j-l}^u$ are defined by

$$h_{m,j}^u = H_m^{(1)}(k_s|uD+jd|)e^{i(\alpha_0 uD - m\arg(uD+jd))}. \tag{2.26}$$

The making of the total field in the vicinity of the l-th fiber is clearly indicated by (2.25). The first term is the field scattered by the slab boundaries, the second is the field contribution from fibers in the central cell, the third is the field contribution from all fibers in other cells ($u \neq 0$), the last is the field scattered by the l-th fiber itself.

Using the relative lattice sums [23] $S_m^j = S_{m,j}^1 + S_{m,j}^2\delta_j$, the total field in the vicinity of the l-th fiber is expanded as

$$V(\mathbf{r}) = \sum_{m\in\mathbb{Z}}\left[A_m^l g_m^J(k_s,\mathbf{r}_l) + B_m^l g_m^{H^{(1)}}(k_s,\mathbf{r}_l)\right] \tag{2.27}$$

where

$$A_m^l = \sum_{p\in\mathbb{Z}} e^{i\alpha_p ld}\left(J_{m,p}^{+} f_p^{b+} + J_{m,p}^{-} f_p^{a-}\right) + \sum_{j\in\mathbb{L}}\sum_{n\in\mathbb{Z}} S_{m-n}^{j-l} B_n^j, \tag{2.28}$$

which is known as the Rayleigh identity and indicates that the incident wave upon the l-th fiber is composed of reflection waves from slab boundaries and other fibers.

In (2.22a) and (2.22b), f_p^{b+} and f_p^{a-} are given as functions of B_m^l. Substitution into (2.28) yields a linear relation between A_m^l and B_m^l:

$$A_m^l = \sum_{j\in\mathbb{L}}\sum_{n\in\mathbb{Z}} \Psi_{m,n}^{l-j} B_n^j + \sum_{j\in\mathbb{L}}\sum_{n\in\mathbb{Z}} S_{m-n}^{j-l} B_n^j + K_m^l. \tag{2.29}$$

where

$$\begin{aligned}\Psi_{m,n}^{l-j} =& \frac{4}{D}\sum_{p\in\mathbb{Z}}\frac{1}{\beta_p^s}(-i)^n e^{i\alpha_p(l-j)d}\left\{J_{m,p}^{+}e^{-i\beta_p^s b}(w_p^s-w_p^b)\Big[w_p^s\cos(n\theta_p+\beta_p^s a)-\right.\\ & iw_p^a\sin(n\theta_p+\beta_p^s a)\Big]+J_{m,p}^{-}e^{i\beta_p^s a}(w_p^s-w_p^a)\Big[w_p^s\cos(n\theta_p+\beta_p^s b)+\\ & \left.iw_p^b\sin(n\theta_p+\beta_p^s b)\Big]\right\}/\Lambda_p,\end{aligned} \tag{2.30}$$

$$K_m^l = 2\sum_{p\in\mathbb{Z}}e^{i\alpha_p ld}\delta_p\left[J_{m,p}^{+}w_p^a(w_p^s-w_p^b)e^{-i\beta_p^s b}+J_{m,p}^{-}w_p^a(w_p^s+w_p^b)e^{i\beta_p^s b}\right]/\Lambda_p. \tag{2.31}$$

Another linear relation between A_m^l and B_m^l is established from the fiber boundary conditions,

$$\begin{cases} E_y^f|_{r_l=c} = E_y^s|_{r_l=c} \\ H_{\theta_l}^f|_{r_l=c} = H_{\theta_l}^s|_{r_l=c} \end{cases} \tag{2.32}$$

for TM polarized waves,

$$\begin{cases} H_y^f|_{r_l=c} = H_y^s|_{r_l=c} \\ E_{\theta_l}^f|_{r_l=c} = E_{\theta_l}^s|_{r_l=c} \end{cases} \tag{2.33}$$

for TE cases, where $H_{\theta_l}^f|_{r_l=c}$ is the angular component of the magnetic field strength on the fiber side while the observation radius equals c, other notations being similarly defined. Substituting the CWE expressions of inside and in the vicinity of the fiber, we have

$$B_m^l = R_{m,l}A_m^l + T_{m,l}Q_m^l, \tag{2.34a}$$

$$C_m^l = T_{m,l}^{'}A_m^l + R_{m,l}^{'}Q_m^l, \tag{2.34b}$$

where for TM

$$R_{m,l} = \frac{\eta_s J_m(k_s c)\dot{J}_m(k_l c)-\eta_l\dot{J}_m(k_s c)J_m(k_l c)}{\eta_l J_m(k_l c)\dot{H}_m^{(1)}(k_s c)-\eta_s\dot{J}_m(k_l c)H_m^{(1)}(k_s c)}, \tag{2.35a}$$

$$T_{m,l} = \frac{2i\eta_s}{\pi c k_l}\frac{1}{\eta_l J_m(k_l c)\dot{H}_m^{(1)}(k_s c)-\eta_s\dot{J}_m(k_l c)H_m^{(1)}(k_s c)}, \tag{2.35b}$$

$$T_{m,l}^{'} = \frac{2i\eta_l}{\pi c k_s}\frac{1}{\eta_l J_m(k_l c)\dot{H}_m^{(1)}(k_s c)-\eta_s\dot{J}_m(k_l c)H_m^{(1)}(k_s c)}, \tag{2.35c}$$

$$R_{m,l}^{'} = \frac{\eta_s H_m^{(1)}(k_s c)\dot{H}_m^{(1)}(k_l c)-\eta_l\dot{H}_m^{(1)}(k_s c)H_m^{(1)}(k_l c)}{\eta_l J_m(k_l c)\dot{H}_m^{(1)}(k_s c)-\eta_s\dot{J}_m(k_l c)H_m^{(1)}(k_s c)}. \tag{2.35d}$$

c is the fiber radius, and η_l and η_s are characteristic impedances of the l-th fiber and matrix material. Exchanging positions of η_l and η_s yields the TE formulas.

Setting Q_m^l in (2.34) as zeros since no inner sources are considered and combining them with (2.29), the solution of B_m^l is obtained, as

$$\mathbf{B} = (\mathbf{I} - \mathbf{RS} - \mathbf{R}\Psi)^{-1}\mathbf{RK} \tag{2.36}$$

where vectors $\mathbf{B} = [B_m^l]$, $\mathbf{K} = [K_m^l]$, and matrices are $\mathbf{I}$ as the identity matrix, $\mathbf{R} = \text{diag}\{R_{m,l}\}$, $\mathbf{S} = [S_{m-n}^{j-l}]$, and $\Psi = [\Psi_{m,n}^{l-j}]$.

$\mathbf{B}$ is the key to all PWE and CWE coefficients. Its substitution into (2.22) generates the solutions of f_p^+, g_p^-, r_p, t_p, (2.20) for f_p^-, g_p^+, (2.29) for A_m^l, and (2.34b) for C_m^l. The full-field solution follows the computation of involved PWEs or CWEs.

2.5 Other types of defects

The modeling of section 2.4 extends to laminates with other types of damages. For fiber displacement, the missing fibers are replaced by sound ones and changes are enforced on the locations of fiber centers. For fiber shrinkage/expansion and inclusion inside the fibers, the physical structure of the fiber is changed, and the damaged fiber boundary conditions have to be adjusted.

2.5.1 Fiber displacement and shrinkage/expansion

With fiber shrinkage/expansion, the only change is the radii of fibers, thus c is replaced by c_l as the radius of the l-th fiber. The definitions in (2.35) need to be updated accordingly.

For fiber displacements, the fiber centers are not regularly placed anymore and $h_{m-n,j-l}^u$ is reformulated into

$$h_{m,j-l}^u = H_m^{(1)}(k_s|uD\hat{x} + \mathbf{o}_l^j|)e^{i(\alpha_0 uD - m\arg(uD\hat{x}+\mathbf{o}_l^j))}, \tag{2.37}$$

where $\mathbf{o}_l^j = \mathbf{o}_j - \mathbf{o}_l$, $\mathbf{o}_j$ and $\mathbf{o}_l$ being centers of the j-th and l-th fibers, respectively. In addition, the definition of F_m^p in (2.19) changes as $\sum_{l\in\mathbb{L}} B_m^l e^{-i\left[\alpha_p(ld+\Delta x_l)+\beta_p^s \Delta z_l\right]}$, where Δx_l, Δz_l are the displacements along the $\hat{x}$ and $\hat{z}$ direction, respectively.

2.5.2 Inclusions

Inclusions [37] can be in the matrix or inside the fiber. In the first case, they can be treated as air fibers but with shrinkage/expansion and displacement, thus no extra explanation

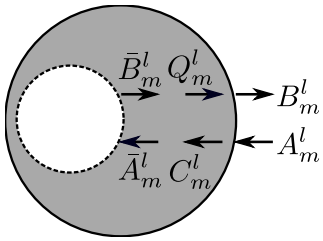

Fig. 2.6 Field representations for analyzing the circular inclusion inside a fiber.

is put here. In the second case, since the damaged fiber becomes inhomogeneous, field coupling inside it requires further analysis.

As shown in Fig. 2.6, the field inside the fiber but outside the inclusion consists of the field scattered by the inclusion and the inner fiber boundary. Upon expressing them in CWEs with coefficients $\bar{B}_m^l$ and C_m^l, respectively,

$$V(\mathbf{r}) = \sum_{m'\in\mathbb{Z}} \left[C_m^l g_m^J(k_l, \mathbf{r}_l) + \bar{B}_m^l g_m^{H^{(1)}}(k_l, \bar{\mathbf{r}}_l) \right]. \tag{2.38}$$

$\bar{\mathbf{r}}_l$ is the relative position of $\mathbf{r}$ in the local coordinate system associated with the inclusion. Let us denote its center as $\bar{\mathbf{o}}_l$ and $\Delta\mathbf{o}_l = \bar{\mathbf{o}}_l - \mathbf{o}_l$. Applying the Graf's addition theorem with condition $|\Delta\mathbf{o}_l| < |\mathbf{r}_l|$, the field scattered by the inclusion can be transformed into

$$V_b^s(\mathbf{r}) = \sum_{m\in\mathbb{Z}} g_m^{H^{(1)}}(k_l, \mathbf{r}_l) \sum_{m'\in\mathbb{Z}} \bar{B}_{m'}^l g_{m'-m}^J(k_l, -\Delta\mathbf{o}_l). \tag{2.39}$$

Then the field near the inner fiber boundary can be expressed as

$$V(\mathbf{r}) = \sum_{m\in\mathbb{Z}} \left[C_m^l g_m^J(k_l, \mathbf{r}_l) + Q_m^l g_m^{H^{(1)}}(k_l, \mathbf{r}_l) \right], \tag{2.40}$$

where

$$Q_m^l = \sum_{m'\in\mathbb{Z}} \bar{B}_{m'}^l g_{m'-m}^J(k_l, -\Delta\mathbf{o}_l). \tag{2.41}$$

Similarly, the field scattered by the fiber inner boundary can be rewritten as

$$V_{f,in}^s(\mathbf{r}) = \sum_{m\in\mathbb{Z}} g_m^J(k_l, \bar{\mathbf{r}}_l) \sum_{n\in\mathbb{Z}} C_n^l g_{n-m}^J(k_l, \Delta\mathbf{o}_l). \tag{2.42}$$

Then the field near the inclusion can be expressed as

$$V(\mathbf{r}) = \sum_{m\in\mathbb{Z}} \left[\bar{A}_{m'}^l g_m^J(k_l, \bar{\mathbf{r}}_l) + \bar{B}_{m'}^l g_m^{H^{(1)}}(k_l, \bar{\mathbf{r}}_l) \right], \tag{2.43}$$

where

$$\bar{A}^l_{m'} = \sum_{n\in\mathbb{Z}} C^l_n g^J_{n-m}(k_l, \Delta\mathbf{o}_l). \tag{2.44}$$

With the linear relation from inclusion boundary conditions

$$\bar{B}^l_m = \bar{R}_{m,l}\bar{A}^l_m, \tag{2.45}$$

$\bar{R}_{m,l}$ similarly defined with $R_{m,l}$ in (2.35), Q^l_m can be linearly represented by C^l_n as

$$Q^l_m = \sum_{n\in\mathbb{Z}} C^l_n t^l_{m,n}, \tag{2.46}$$

where

$$t^l_{m,n} = \sum_{m'\in\mathbb{Z}} \bar{R}_{m',l} g^J_{m'-m}(k_l, -\mathbf{o}^b_l) g^J_{n-m'}(k_l, \Delta\mathbf{o}_l). \tag{2.47}$$

Q^l_m has been expressed as a function of C^l_m. Together with fiber boundary conditions in (2.34), we have the linear relation between B^l_m and A^l_m, as

$$\mathbf{B} = \Phi\mathbf{A}, \tag{2.48}$$

in which $\Phi = \mathrm{diag}\{\Phi_l\}$ and Φ_l is defined by

$$\Phi_l = \mathbf{R}_l + \mathbf{T}_l\mathbf{t}_l(\mathbf{I} - \mathbf{R}'_l\mathbf{t}_l)^{-1}\mathbf{T}'_l\delta^l_b \tag{2.49}$$

where $\mathbf{R}_l$, $\mathbf{T}_l$, $\mathbf{t}_l$, $\mathbf{R}'_l$ and $\mathbf{T}'_l$ are made of elements of $R_{m,l}$, $T_{m,l}$, $t^l_{m,n}$, $R'_{m,l}$ and $T'_{m,l}$ correspond to the l-th fiber, respectively. δ^l_b is 1 if an inclusion exists inside the l-th fiber, otherwise 0. The field analysis then goes back to section 2.4 by replacing (2.29) with (2.48).

2.6 Line source illumination

Set a line source at $\mathbf{o}_s$ in the upper half-space Ω_a, the corresponding incident field being the Green function $H^{(1)}_0(k_a|\mathbf{r}-\mathbf{o}_s|)/(4i)$, which can be expressed as [33]

$$V^s(\mathbf{r}, \mathbf{o}_s) = \frac{1}{i4\pi}\int_{-\infty}^{\infty} \mathrm{d}\alpha_0 \frac{e^{i\alpha_0 x + i\beta^a|z|}}{\beta^a}, \tag{2.50}$$

in which the integrand indicates a plane wave as function of α_0, $\beta^a = \sqrt{k_a^2 - \alpha_0^2}$. Taking $e^{i(\alpha_0 x - \beta^a z)}/\beta^a$ as incident waves, with the modeling approach of section 2.4 and 2.5, the corresponding field solution $V(\alpha_0)$ can be readily obtained. Then the total field due to the

line source is

$$V(\vec{r},\vec{o}_s)=\frac{1}{4i\pi}\int_{-\infty}^{\infty}\mathrm{d}\alpha_0 V(\alpha_0), \tag{2.51}$$

which can be dealt with by numerical methods, such as trapezoidal and Gauss-Legendre scheme [19].

2.7 Computational details

In this section, strategies are proposed for the following three issues. First, as shown above, PWEs and CWEs are infinite series which are not tractable in the computation. Their truncations, as approximated but accurate enough replacement, are used in operations. However, how to do these truncations can be a challenge. Second, carrying out the Sommerfeld integration is required in cases with line-source illumination. Singularities of the integrand prevent computational efficiency and an acceleration strategy is presented. Indeed, imaging procedures often use multiple sources and sensors to achieve the best performances. Upon assumption of a line source illumination, multiple integrations would be involved and their efficient handling becomes important, which is the third issue of concern.

2.7.1 Truncation number

The selection of the truncation number of PWE and CWE matters much on the modeling accuracy and stability. Let us take the truncation number for PWE as M, for CWE as P, *i.e.*, $\sum_{m\in\mathbb{Z}}$ and $\sum_{p\in\mathbb{Z}}$ are replaced by $\sum_{m=-M}^{M}$ and $\sum_{m=-P}^{P}$.

In brief, (a) too small M or P means that not enough high-order components are included in the expression, which results in inaccurate fields, (b) too large a M means that many high-order components are included, which makes the to-be-inverted matrix $(\mathbf{I}-\mathbf{RS}-\mathbf{R}^{-})$ ill-conditioned, (c) a large P means heavy computational burden, the situation becoming worst for line source illumination, where hundreds even thousands samples of α_0 need to be computed. To overcome this problem, a numerical approach is proposed.

Without damage, the handy formulas in [14], $M=\mathrm{Int}\left(\Re\left(4.05\times(k_s c)^{1/3}+k_s c\right)+7\right)$ and $P=\mathrm{Int}\left(d\left(3\Re(k_s)-\alpha_0\right)/2\pi\right)$, can be applied, Int being the integral part. While the selection of M can guarantee the modeling accuracy of CWE, the P formula is from numerical experiments however, and the accuracy of PWE cannot be guaranteed, especially at low frequencies.

Table 2.1 Procedure to decide P and M.

1.	Initialization: $P_1 = 0$, $M = \mathrm{Int}\left(\Re\left(4.05 \times (k_s c)^{1/3} + k_s c\right)\right) + 7$.
2.	Search P_1: set $L = 1$ and compute $\mathrm{d}V$. If $\mathrm{d}V < \nu$, return P_1; otherwise, $P_1 = P_1 + 1$ and repeat step 2.
3.	Search M: let $M = M - 1$. If $\mathrm{d}V > \nu$, $M = M + 1$, return M; otherwise repeat step 3.
4.	Search P I: with true L, set $P = LP_1$ and compute $\mathrm{d}V$. If $\mathrm{d}V < \nu$, $P = P - 1$ and $\gamma_1 = 1$; otherwise $P = P + 1$ and $\gamma_1 = -1$.
5.	Search P II: compute $\mathrm{d}V$. $\gamma_2 = 1$ if $\mathrm{d}V < \nu$; $\gamma_2 = -1$ otherwise. If $\gamma_1 = \gamma_2$, $P = P - \gamma_2$ and repeat step 5; otherwise, stop and return $P = P + (1 - \gamma_2)/2$.

The proposed strategy is based on the observation that the field solution at any point in Ω_s computed from PWE and CWE should be the same. Then, M is first initialized by the above formula. Let us denote V_p, V_c as field solutions from PWE and CWE and $\mathrm{d}V = \left|V_p - V_c\right|$, and increase P from 0 until the criterion $\mathrm{d}V < \nu$ is satisfied, ν being the desired accuracy.

For the damaged structure, the formula about M is unchanged and the search of an optimal P can follow the same procedure as for the undamaged one. However, with the supercell concept, when the number of fibers included in the supercell is large, the optimal P should be large and searching P from 0 inefficient. By numerical testing, we concluded that $P \approx LP_1$, P_1 the truncation number of PWE for the undamaged structure. So the strategy is to find P_1 first, then search for P starting from LP_1. The whole procedure is sketched in Table 2.1, where the effort to decrease M is also made.

2.7.2 Efficient calculation of single integration

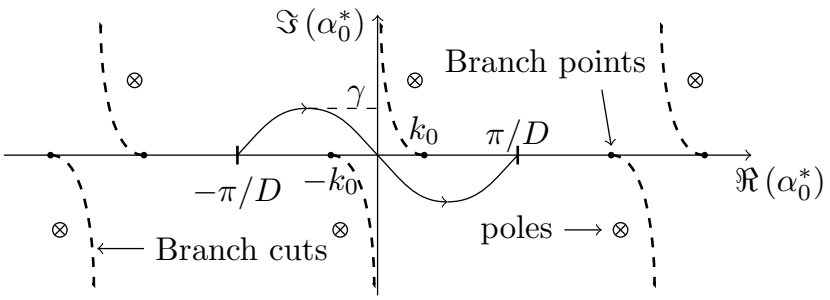

Fig. 2.7 Sketch of branch cuts/points, poles and detoured path in complex α_0^* plane when $k_a = k_b$.

In (2.51), branch points and poles in $V(\alpha_0)$, may complicate the integration, and consequently slow down the convergence sought. Two techniques are adopted to alleviate the above, detouring the integration path and reducing the integration interval. Singularities are periodic with period $2\pi/D$, thus the detoured path is defined as $\alpha_0^* = \alpha_0 - i\gamma\sin(D\alpha_0)$, γ amplitude of the imaginary part, as shown in Fig. 2.7. The complex plane of α_0^* is defined in the top Riemann sheet ($\Im(\beta_j) > 0$). Singularity points are surrounded and the convergent rate benefits from the smoother integrand. The other acceleration comes from the rewritten form of (2.50),

$$\begin{aligned} V^s(\vec{r},\vec{o}_s) &= \frac{1}{4i\pi}\sum_{p\in\mathbb{Z}}\int_{-\pi/D+p\frac{2\pi}{D}}^{\pi/D+p\frac{2\pi}{D}} \mathrm{d}\alpha_0 \frac{e^{i\alpha_0 x+i\beta^a|z|}}{\beta^a} \\ &= \frac{1}{4i\pi}\int_{-\pi/D}^{\pi/D}\mathrm{d}\alpha_0\sum_{p\in\mathbb{Z}}\frac{e^{i\alpha_p x+i\beta_p^a|z|}}{\beta_p^a}. \end{aligned} \tag{2.52}$$

Replacing δ_p in (2.8) by $1/\beta_p^a$, multiple sampling points of α_0 can be computed in a single calculation without additional cost, and the integration interval is reduced from $[-\infty,\infty]$ to $[-\pi/D,\pi/D]$.

2.7.3 Efficient calculation of multiple integrations

Since the Sommerfeld integration has no closed-form solution, a numerical method is applied. However, the integrand is not smooth due to the singularities [14], thus traditional methods, like with trapezoidal schemes, would be inefficient. Recently, a scheme has been proposed [38], within which the distribution of sampling points could adjust to the shape of the integrand, less for smooth segments and more for sharp peaks, in brief. To do so, the corresponding Matlab subroutine, QUADCC [39] is utilized.

Yet only one scalar value is enabled to be computed in one calculation. If multiple field values to compute, similar calculations should be repeated. Below, a strategy is proposed to compute multiple values in one calculation without much additional computational cost by making use of our knowledge about the integrand.

Let us denote the locations of a group of source-sensor as $\mathbf{o}_s$, $\mathbf{r}_o$, and the corresponding integrand as $V(\alpha_0,\mathbf{r}_o,\mathbf{o}_s)$. For another group with locations $\mathbf{o}_s+\mathrm{d}\mathbf{o}_s$ and $\mathbf{r}_o+\mathrm{d}\mathbf{r}_o$, if $|\mathrm{d}\mathbf{o}_s|$ and $|\mathrm{d}\mathbf{r}_o|$ is small enough compared with the wavelength, $V(\alpha_0,\mathbf{r}_o+\mathrm{d}\mathbf{r}_o,\mathbf{o}_s+\mathrm{d}\mathbf{o}_s)$ shares similar behavior with $V(\alpha_0,\mathbf{r}_o,\mathbf{o}_s)$, which means that if $V(\alpha_0,\mathbf{r}_o+\mathrm{d}\mathbf{r}_o,\mathbf{o}_s+\mathrm{d}\mathbf{o}_s)$ and $V(\alpha_0,\mathbf{r}_o,\mathbf{o}_s)$ are integrated with the same sampling points of α_0, two integration values are generated simultaneously. Even more, since $V(\alpha_0,\mathbf{r}_o+\mathrm{d}\mathbf{r}_o,\mathbf{o}_s+\mathrm{d}\mathbf{o}_s)$ and $V(\alpha_0,\mathbf{r}_o,\mathbf{o}_s)$ are involving the same expansion coefficients, there is almost no extra computation cost to compute two group values.

There are still small differences between $V(\alpha_0, \mathbf{r}_o, \mathbf{o}_s)$ and $V(\alpha_0, \mathbf{r}_o + d\mathbf{r}_o, \mathbf{o}_s + d\mathbf{o}_s)$. To be accurate for all values, the group-index set $\mathbf{J}$ is designed. Let us assume that S sources and R receivers are operated. There would be $S \times R$ combinations of source-sensor groups, and $\mathbf{J}$ will be initialized as $\{1, 2, \ldots, S \times R\}$. Upon computing field values for groups in $\mathbf{J}$, once the j-th group satisfies the convergence criterion (set by numerical schemes), $\mathbf{J}$ would be updated as $\mathbf{J} \setminus \{j\}$. And the computation is repeated until $\mathbf{J}$ is empty.

2.8 Numerical simulations

The laminates as considered now are with fiber period $d = 0.1$mm, slab boundaries $a = -b = 0.5d$, graphite (relative permittivity $\Re\left(\epsilon_{rf}\right) = 12$, conductivity $\sigma = 330$ S/m) or glass (relative permittivity $\epsilon_{rf} = 6$) fiber. The fiber radius is $c = 0.25d$, except for fibers that shrink or expand, which will be mentioned specifically. The matrix material is epoxy with $\epsilon_{rs} = 3.6 + 0.072i$, *i.e.*, loss tangent $\tan\delta = 0.02$. The default polarization is TM. Examples with TE are shown also.

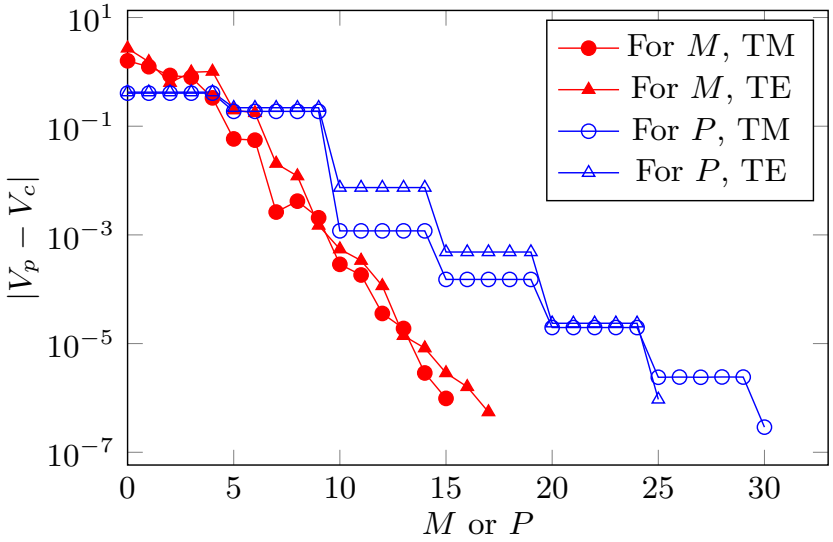

Fig. 2.8 Convergence of field expansion vs. P & M for well-organized glass-fiber laminate, fiber period $d = 0.1$mm, radius $c = 0.25d$, $\lambda^{inc} = d$, number of fibers in the cell $L = 5$.

The truncation of infinite series $\sum_{m\in\mathbb{Z}}$ and $\sum_{p\in\mathbb{Z}}$ is first discussed. When $r_l < d$, the field outside the l-th fiber can be computed by PWE or CWE and $\left|V_p - V_c\right|$ should be zero without truncations of series. Setting the observation point at $(0, (a+c)/2)$, with a well-organized structure, as shown in Fig. 2.8, the value of $\left|V_p - V_c\right|$ decreases fast with increasing P and M and the wave polarization has little impact on the convergence speed. With $M = 17, P = 30$,

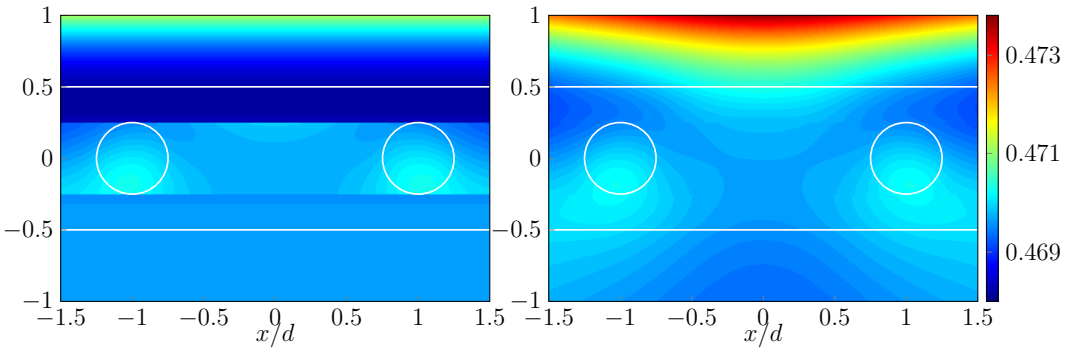

(a) $\lambda^{inc} = 100d$, $P_l = 0$, $P_r = 13$

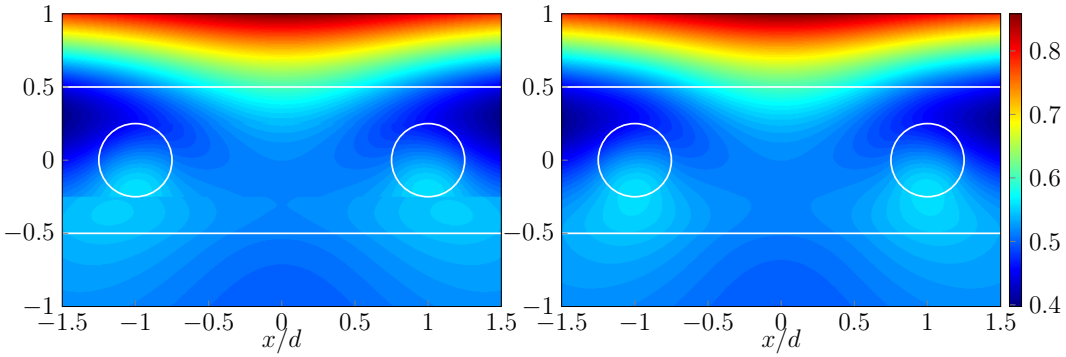

(b) $\lambda^{inc} = 10d$, $P_l = 7$, $P_r = 26$

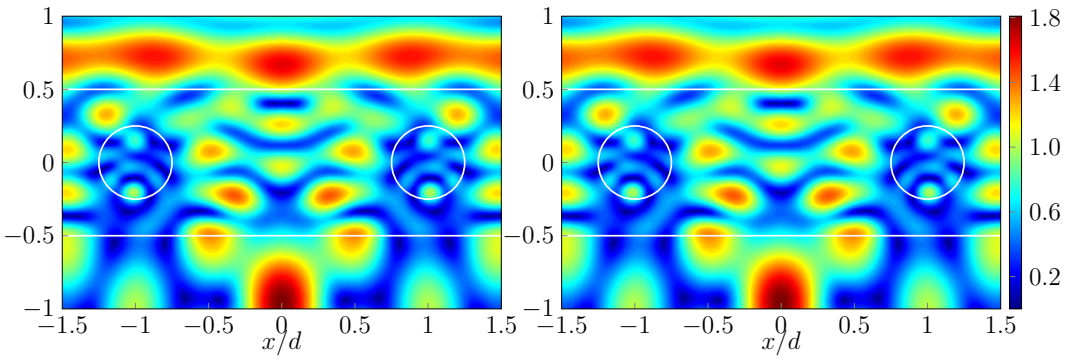

(c) $\lambda^{inc} = d$, $P_l = 74$, $P_r = 65$

Fig. 2.9 Maps of field intensity with TM planar-wave illuminations, truncation number decided by (left) the formula with P_l and (right) the proposed numerical approach with P_r, $L = 13$, epoxy slab and glass fiber, white lines indicating the laminate structure.

$\left|V_p - V_c\right|$ is less than 10^{-6}. Thus, the truncated series as $\sum_{m=-M}^{M}$ and $\sum_{p=-P}^{P}$ can approximate the initial ones $\sum_{m\in\mathbb{Z}}$ and $\sum_{p\in\mathbb{Z}}$ with high accuracy.

For general cases, as described in section 2.7.1, while M is estimated with the formula $M = \mathrm{Int}\left(\Re\left(4.05 \times (k_s c)^{1/3} + k_s c\right) + 3\right)$, P can be obtained two ways, from the formula

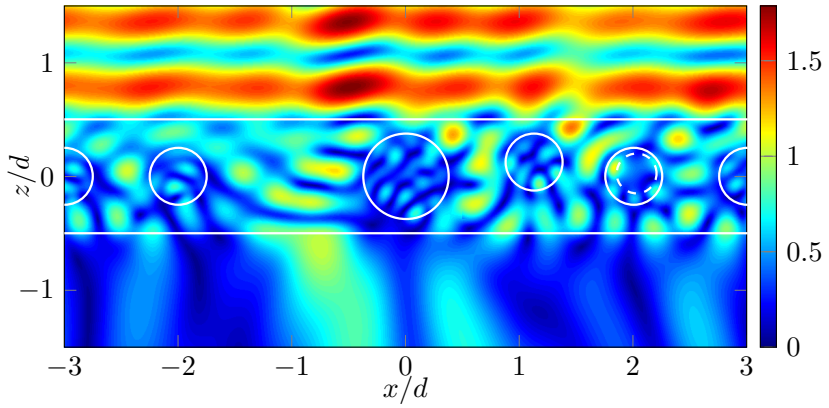

Fig. 2.10 Map of field intensity with a TM planar-wave illumination, which is computed by the supercell approach, $\lambda^{inc} = d$, white lines indicating the laminate structure.

$P = \mathrm{Int}\left(D\left(3\Re\left(k_s\right) - \alpha_0\right)/2\pi\right)$, or from the approach summarized in Table 2.1. Let us assume that the laminate is with the 0-th fiber missing. Illumination is by a plane wave with $\theta^{inc} = 0$ and wavelength λ^{inc}. Each supercell consists of 13 fibers (including missing ones). Maps of field intensity computed with Ps from the two approaches at different λ^{inc}s are in Fig. 2.9.

Let us notice that fields in region $-c < z < c$ are computed via CWEs and in other regions via PWEs. For $\lambda^{inc} = d$, both approaches yield good results, however, for other two cases with P from the formula, fields are discontinuous along the lines $z = c$ and/or $z = -c$. This comes from too small generated Ps, equation (2.18), which is a CWE-to-PWE transformation, being not satisfied. In contrast, with the proposed strategy, this problem is avoided.

A number of validations of our modeling approach is performed by comparing its results with those provided by the finite-element COMSOL software [40]. The latter is run with two configurations depending upon the validation target, the 1st one to exactly model the supercell-based periodic structure by enforcing periodic conditions on the object boundaries, the 2nd one to approximate the true laminate by a finitely-sized yet large enough module without the periodicity constraint.

Validations of the supercell approach are now performed by comparing its results with those of COMSOL with the 1st configuration. Let us assume that all types of defects coexist within a graphite-fiber laminate. Specifically, the -1st fiber is missing, the 0-th fiber is with radius $1.5c$, the 1st one is with displacement with fiber center at $(d + 0.5c, 0.5c)$, and a void inclusion with radius $0.7c$ centered at $(2d + 0.1c, 0.1c)$ is located inside the 2nd fiber. The incident wave is planar with angle $\theta^{inc} = \pi/6$. The TM field intensity map for $\lambda^{inc} = d$ is in Fig. 2.10. Resonances inside the laminate and field disturbances due to

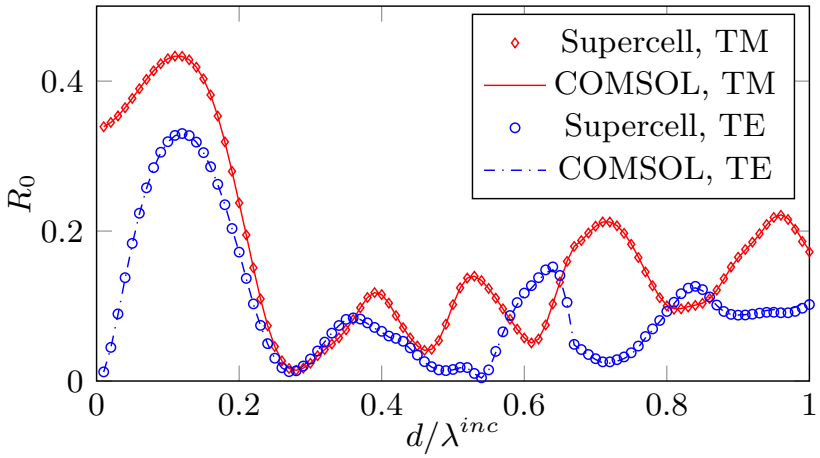

Fig. 2.11 Validation of the supercell approach with planar-wave illumination $\theta^{inc} = \pi/6$, $d = 0.1$mm, $c = 0.25d$, $L = 31$.

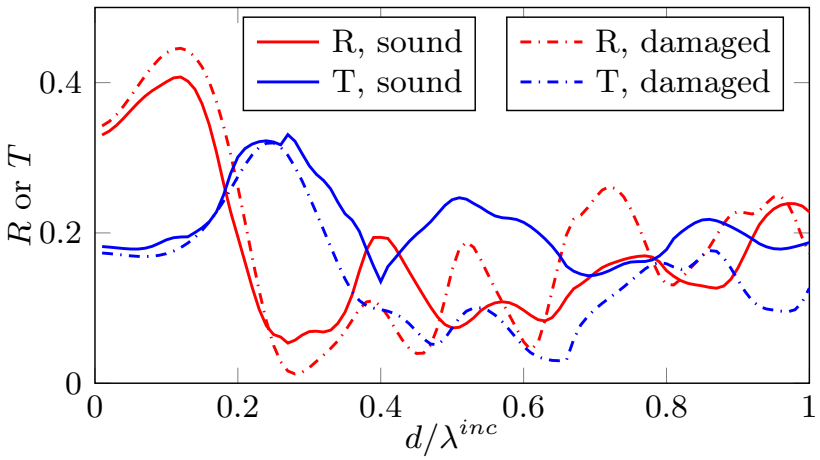

Fig. 2.12 Comparison of R and T between damaged and sound laminates with TM planar-wave illuminations.

damages are observed. Then, let us define the p-th mode of the reflection coefficient as $R_p = \Re\left(\left(\beta_p^a\right)^* r_p r_p^* / \beta_p^a\right)$. R_0 from the two approaches are compared at different frequencies and polarizations in Fig. 2.11, results fitting very well. Damage impact on reflection and transmission are seen in Fig. 2.12, where R and T are defined as $R = \sum_{p\in\mathbb{Z}} R_p$, $T = \sum_{p\in\mathbb{Z}} T_p$.

Changing the fiber material as glass and perfect electrical conductor (PEC), comparisons of R_0 are shown in Fig. 2.13, where multiple missing fibers happen and the supercell has 5 fibers in the modeling. The agreements of results confirm the validity of the supercell modeling approach under various configurations.

In modeling line sources, γ (the amplitude of the imaginary part of the defined detouring path) affects the computation efficiency. The recently introduced package QUADCC, which

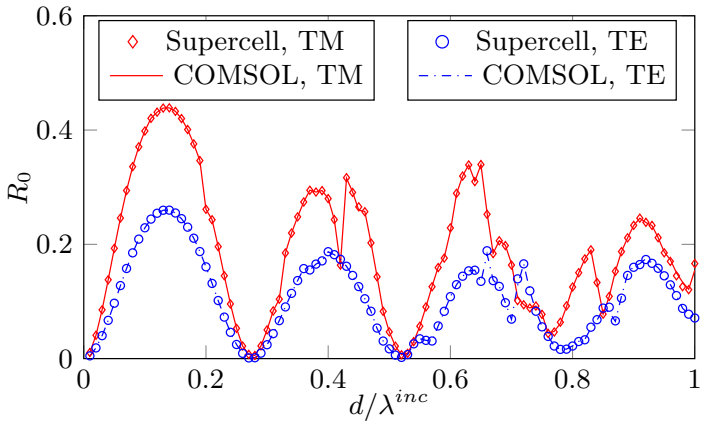

(a) glass fiber

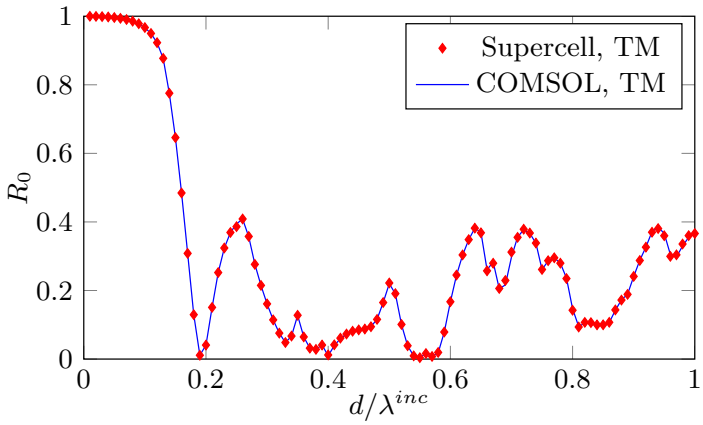

(b) PEC fiber

Fig. 2.13 Validation of the supercell approach with (a) glass and (b) PEC fibers, planar-wave illumination $\theta^{inc} = \pi/6$, $d = 0.1$mm, $c = 0.25d$, $L = 5$, -1st and 1st fibers missing.

in particular obeys Clenshaw-Curtis quadrature rules, is adopted to perform the integration. Testing with an intact structure, Fig. 2.14 shows the number of required samples with different γ. When $\gamma = 10$ and $\gamma = 100$, the sampling number is indeed smaller than by integrating along the real axis ($\gamma = 0$). However, too large a γ may slow down the convergent rate. In time cost, it is 1200s for point $(0, 0.5c)$ with $\gamma = 0$, $\approx 60\%$ with $\gamma = 100$ and $\approx 130\%$ with $\gamma = 1000$.

Validations for the line-source illumination are performed by comparing fields along the line $z = 0.5c$, $-5d \leq x \leq 5d$. Both COMSOL and the supercell approach are run with 81 fibers, save that the periodic condition is not configured anymore in COMSOL, so that it should return the solution for the true laminate. As shown in Fig. 2.15(a) and 2.15(b),

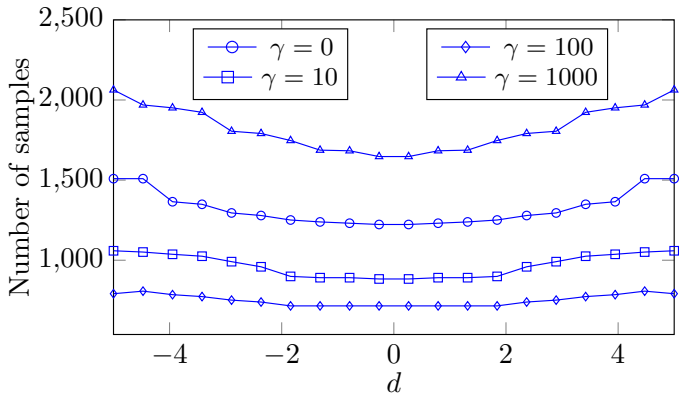

Fig. 2.14 Number of samples in QUADCC with various γ. The line source at $\mathbf{r}_s = (0, a + d)$ illuminates a well-organized graphite-fiber laminate, $d = 0.1$mm, $c = 0.25d$, $\lambda^{inc} = 10d$.

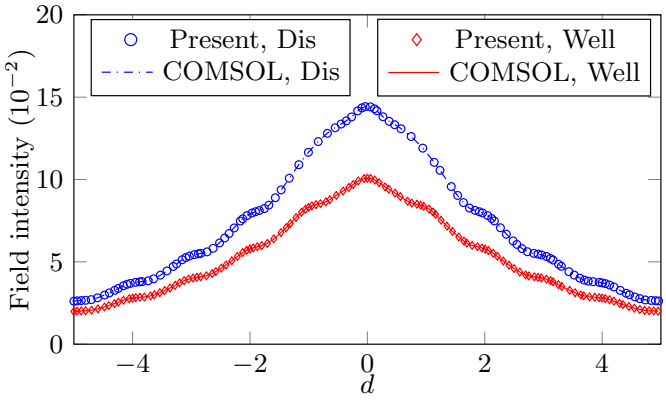

(a) graphite fiber, $\lambda^{inc} = 10d$

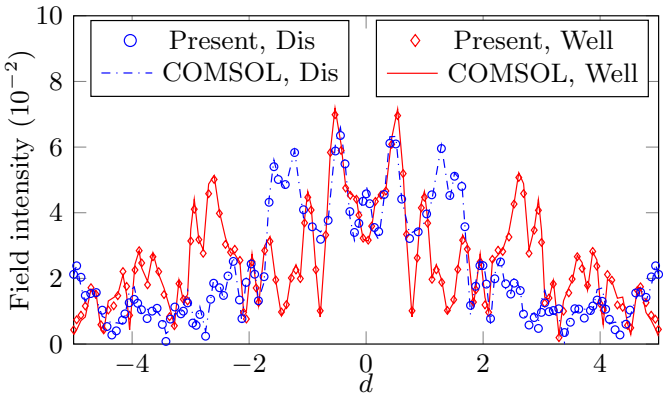

(b) glass fiber, $\lambda^{inc} = d$

Fig. 2.15 Comparisons of fields intensity with the TM line source illumination, $\mathbf{r}_s = (0, a + d)$, $d = 0.1$mm, $c = 0.25d$, $L = 81$, -1st and 1st fibers missing for the disorganized laminate, denoted by “Dis", while “Well" is for the well-organized.

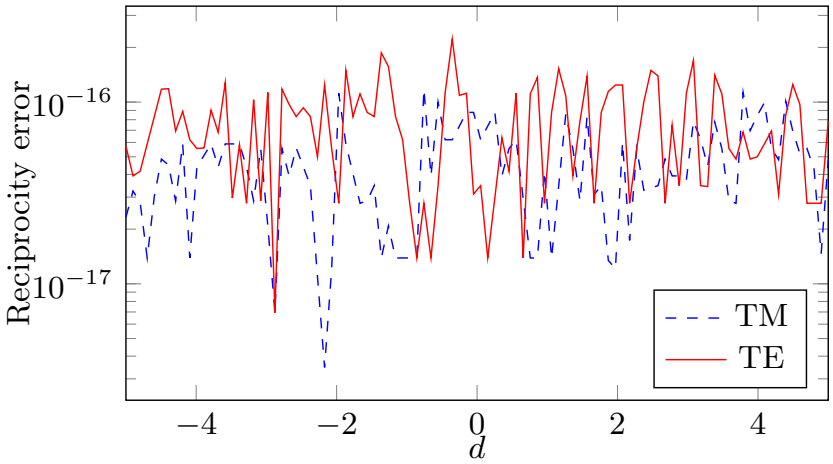

Fig. 2.16 Reciprocity error vs. sampling, graphite-fiber disorganized laminate with −1st and 1st fibers missing, $d = 0.1$mm, $c = 0.25d$, $\lambda^{inc} = 10d$.

with glass or graphite fiber, results for a well-organized and a disorganized structure (−1st and 1st fibers missing) fit well, despite strong resonances in the case of $\lambda^{inc} = d$.

Accuracy of the modeling is also checked by testing reciprocity. The line source above an intact structure is at $(0, a+2d)$ and the field is observed along the line $-5d \le x \le 5d$, $z = a+d$, with V_1 as collected data vector. Exchanging source and observer positions yields V_2. Values of $|V_1 - V_2|$ are drawn as the line graph in Fig. 2.16, with amplitude $\sim 10^{-16}$.

The design of the supercell structure is so as to approximate the field solution of the true laminate, the condition being a supercell size large enough. Let us look at convergence of field values when increasing the supercell size. Tests are with the laminate having two missing fibers, indexed −1 and 1. Fiber material is graphite or glass, wavelength $\lambda^{inc} = 10d$. 100 field values are uniformly sampled along the line $z = a+d$, $-5d \le x \le 5d$. Let us denote ϕ_k^j as field value at the j-th sampling point, the supercell having $L = 2k+1$ fibers. The criterion to stop increasing k is that relative error $\tau(k) = \max\{\left|\phi_{k+1}^j - \phi_k^j\right| / \left|\phi_{k+1}^j\right| : j\}$ is smaller than 10^{-3}.

Fig. 2.17(a) shows results with the plane-wave illumination with $\theta^{inc} = 0$. Fig.2.17(b) is for results with line-source illumination with $\mathbf{o}_s = (0, a+d)$. Because of the lossy character of graphite, the convergence rate with carbon fiber is much better than the one with glass fiber. Since glass is taken lossless (conductivity $\sigma < 10^{-10}$ S/m in practice) and the matrix is low-loss, the field decays slowly along x and L thus stops at a relatively large value. We also observe that convergence with a line source is quicker than with a plane wave, in tune with its localized character.

To show that the supercell-based field solution indeed approximates the true one in low-frequency cases, Born approximation is used to make comparisons.

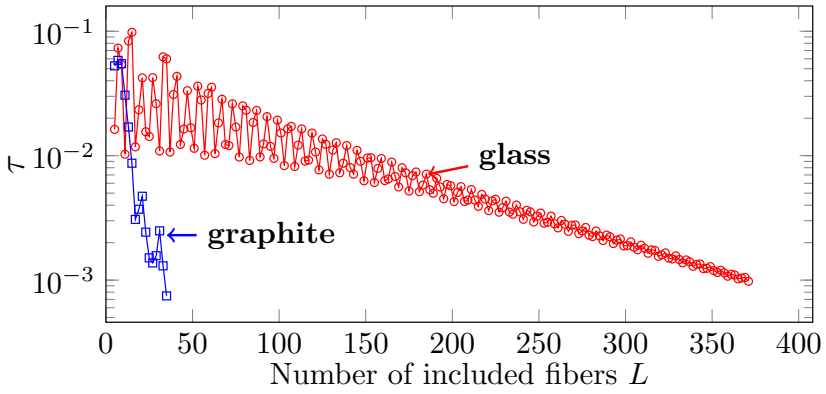

(a)

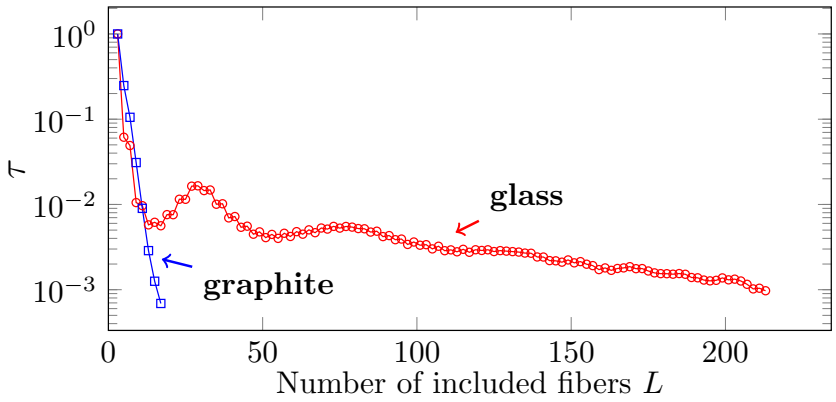

(b)

Fig. 2.17 Field convergence with illumination by (a) plane wave with $\theta^{inc} = 0$, and (b) line source with $\mathbf{o}_s = (0, a+d)$, $\lambda^{inc} = 10d$, $d = 0.1$mm.

From the Lippmann-Schwinger integral formulation,

$$\tilde{V}(\mathbf{r}) - V(\mathbf{r}) = \sum_{l\in\mathbb{Z}} \int_{D_l} G(\mathbf{r}, \mathbf{o}_s) k_s^2 (\epsilon_{rl} - \epsilon_{rs}) V(\mathbf{o}_s) \mathrm{d}\mathbf{o}_s, \tag{2.53}$$

where $\tilde{V}$ stands for the total field with respect to the undamaged structure and G denotes the Green's function. The Born approximation is operated by replacing V by $\tilde{V}$ within the integrand. To simplify the integration further, since the field inside the fiber is smooth, it can be equated to the one at the fiber center. This yields

$$\tilde{V}(\mathbf{r}) - V(\mathbf{r}) \approx \sum_{l\in\mathbb{Z}} \pi c^2 G(\mathbf{r}, \mathbf{o}_l) k_s^2 (\epsilon_{rl} - \epsilon_{rs}) \tilde{V}(\mathbf{o}_l). \tag{2.54}$$

The tests are performed by comparing V with COMSOL and $\tilde{V} - V$ with the Born approximation. Results in Fig. 2.18 is with $\lambda^{inc} = 100d$, plane wave with $\theta^{inc} = 0$ and

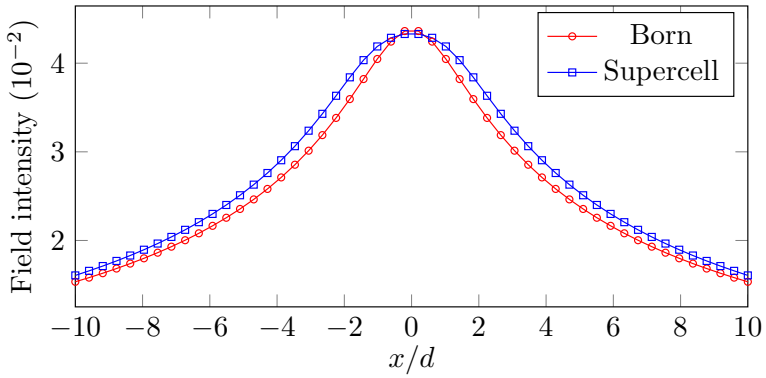

Fig. 2.18 Validation of supercell modeling approach via comparisons with Born approximation, graphite fiber, $\lambda^{inc} = 100d$, normal planar-wave incidence, field values sampled along $z = a + d$, $-10d \leq x \leq 10d$, $L = 257$ for supercell.

$L = 257$. The fiber material is graphite. The true solutions due to line-source and plane-wave illuminations are both well approximated and the effectiveness of the proposed modeling is further validated. Naturally, let us observe that the wavelength when using the Born approximation is large and accuracy follows from that low-frequency assumption.

Table 2.2 Time cost of supercell approach and COMSOL

	Fig. 2.11	**Fig. 2.15(a) (well-organized)**	**Fig. 2.15(b) (disorganized)**
Supercell	22.7 s	23.0 s	315.2 s
COMSOL	51.2 s	18.0 s	29.0 s

With same laptop (dual cores, clock speeds 2.9 GHz, memory 16 GB), average time cost of the supercell approach is shown in Table 2.2, in comparison to COMSOL software in Fig. 2.11, Fig. 2.15(a), and Fig. 2.15(b). With plane-wave illumination, supercell has advantages over COMSOL on modeling efficiency. However, this advantage vanishes for line-source cases, especially with large L. That is because carrying out the Sommerfeld integration needs hundreds, even thousands, plane-wave components to deal with and the computational efficiency is low for large L.

2.9 Summary

By means of an auxiliary supercell periodic structure, fiber-reinforced laminates and alike structures with defects, including missing, displaced, shrunk fibers and circular inclusions, can be successfully dealt with, illuminations by plane waves and line sources in the TM and TE polarization cases being proposed herein.

In the case of plane-wave illumination, benefiting from the structure periodicity and associated quasi-periodic field distribution, fields in the whole region are plane-wave expanded, the cylindrical form being derived from the field periodicity in angular dimension. Matching fields at slab and fiber boundaries generates linear relations among expansion coefficients. Together with Rayleigh identities with respect to the fiber array and the analysis of mutual scatterings between slab and fibers, the solution (the coefficients involved) is obtained and field values follow the computation of expansions.

The field scattered by a line source is decomposed into plane waves and the final field solution indeed is a superposition of scattered fields by plane-wave elements, which can be computed by numerical methods as analyzed. Strategies to determine the truncation number of PWE and CWE and efficiently compute single and multiple Sommerfeld integrations are proposed.

The results are validated by a general-purpose finite-element software and the Born approximation. Modeling accuracy and convergence of the field are exhibited.

Chapter 3

Green's function and analysis of defects with equivalence theory

Playing the key role in modeling and imaging, the full solution of the Green's function, which is the field solution due to a line source in 2D cases, is computed. Three cases depending on the source location are independently considered and analyzed with array scanning method [24], the utilization of which is to overcome the modeling difficulty due to destroyed periodicity by sources. Repeating the line source with period same as that of fibers, field distribution is quasi-periodical with additional specific phases on the fictitious sources. A method based on the Floquet theorem then becomes applicable and the true field solution follows per integration [25], through which the effects from fictitious sources are canceled.

Based on the Green's function, a computationally efficient modeling approach analyzing TM and TE electromagnetic scattering from periodic fiber-reinforced laminates is introduced, when they suffer from missing, shrunk/expanded, displaced fibers, and inclusions. Such damages inside the initially periodic structure (the fibers as organized in a given matrix) are seen as undamaged zones with fictitious sources properly set inside them, and the field results as a summation of responses to the exterior source and equivalent ones. Various numerical results are proposed that are evidencing the interest of this approach. A part of works presented in this chapter has been published in [21].

3.1 Configuration and formulation

The structure of the concerned laminate is the same as described in Chapter 2 and is briefly introduced next considering the completeness of illustration and new notations.

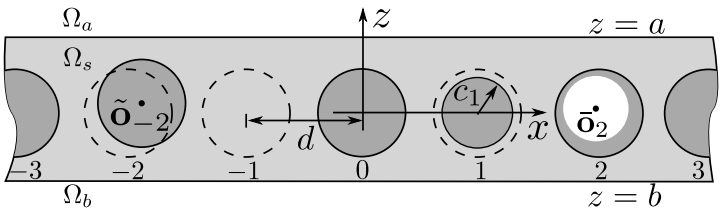

Fig. 3.1 Sketch of the concerned damaged laminate.

The structure of the laminate of concern is sketched in Fig. 3.1. Fibers with infinite length along the y-axis are periodically inserted with period d in a planar slab Ω_s, which is sandwiched by two half spaces Ω_a and Ω_b. Each component is isotropic and homogeneous, with permittivity ϵ_j and permeability μ_j, $j=a,b,s,l$ (relative ones with notations ϵ_{rj} and μ_{rj}), where $j=l$ is for the l-th fiber, $l\in\mathbb{Z}$. Missing, shrunk/expanded, displaced fibers and/or fibers with circular inclusions may exist in the laminate. Labeling fibers as shown in Fig. 3.1, the indexes of damaged fibers compose a set $\mathbb{D}$, *i.e.* the l-th fiber is damaged if $l\in\mathbb{D}$. $\epsilon_l=\epsilon_s$, $\mu_l=\mu_s$ for missing fibers while $\epsilon_l=\epsilon_f$, $\mu_l=\mu_f$, subscript "f" standing for sound fibers. Radius and center of the sound fiber $c_l=c$ and $\mathbf{o}_l=(ld,0)$, putting a tilde above for the notation of the damaged one and a bar instead for the inclusion. With time dependence $\exp(-i\omega t)$, i imaginary unit, ω angular frequency, Transverse Magnetic (TM) electric field and Transverse Electric (TE) magnetic field are investigated, which indicates one remains with a scalar scattering problem.

3.2 Analyze undamaged laminate with supercell method

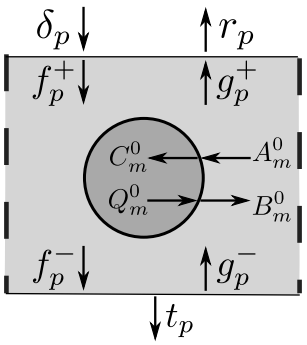

Fig. 3.2 Expansion coefficients of field components within the primary cell.

The Green's function is the field response of the undamaged laminate illuminated by a line source and the solution, illustrated in the next section, will make use of the analysis on

the undamaged periodic structure, which can be reached by simply setting $L = 1$ in the supercell methodology. Accordingly, some formulas or notations need to be reformulated.

Making use of the knowledge $V(\mathbf{r} - ud\hat{x}) = V(\mathbf{r})e^{i\alpha_0 ud}$, $\hat{x}$ the unit vector along x-axis, the investigation could be reduced to the primary periodic cell. As sketched in Fig. 3.2, field in different regions can be expanded in CWEs or PWEs which are similarly defined as in Chapter 2, and exterior plane-wave illumination with unit amplitude and source inside the fiber are considered simultaneously.

With fields scattered by all fibers

$$V_s^f(\mathbf{r}) = \sum_{l\in\mathbb{Z}} e^{i\alpha_0 ld} \sum_{m\in\mathbb{Z}} B_m^0 g_m^{H^{(1)}}(k_s, \mathbf{r}_l), \tag{3.1}$$

the total field in the slab, but outside the fibers, reads as

$$V(\mathbf{r}) = \sum_{p\in\mathbb{Z}} e^{i\alpha_p x}\left(f_p^+ e^{-i\beta_p^s z} + g_p^- e^{i\beta_p^s z}\right) + \sum_{l\in\mathbb{Z}} e^{i\alpha_0 ld} \sum_{m\in\mathbb{Z}} B_m^0 g_m^{H^{(1)}}(k_s, \mathbf{r}_l). \tag{3.2}$$

With Jacobi-Anger expansion and applying the Graf's addition theorem with condition $r < d$, (3.2) can be reformulated as

$$V(\mathbf{r}) = \sum_{m\in\mathbb{Z}} \left[A_m^0 g_m^J(k_s, \mathbf{r}) + B_m^0 g_m^{H^{(1)}}(k_s, \mathbf{r})\right], \tag{3.3}$$

where

$$A_m^0 = \sum_{n\in\mathbb{Z}} S_{m-n} B_n^0 + \sum_{p\in\mathbb{Z}} \left(J_{m,p}^+ g_p^- + J_{m,p}^- f_p^+\right), \tag{3.4}$$

known as the Rayleigh identities [25], $J_{m,p}^{\pm} = (i)^m \exp(\mp im\theta_p)$, $\cos\theta_p = \alpha_p/k_s$. S_{m-n} is the lattice sum defined as

$$S_m = \sum_{l\in\mathbb{Z}\setminus\{0\}} H_m^{(1)}(k_s |l| d) \exp\left[i(\alpha_0 ld - m\arg(l))\right]. \tag{3.5}$$

While S_m can be efficiently computed with a lossy medium, methods for a low-loss or lossless slab should refer to [41, 42].

With the identity

$$\sum_{l\in\mathbb{Z}} e^{i\alpha_0 ld} g_m^{H^{(1)}}(k_s, \mathbf{r}_l) = \sum_{p\in\mathbb{Z}} K_{m,p}^{\pm} e^{i\left(\alpha_p x \pm \beta_p^s z\right)}, \tag{3.6}$$

(3.2) can be fully expressed in PWE form as

$$V(\mathbf{r}) = \sum_{p\in\mathbb{Z}} e^{i\alpha_p x}\left[f_p^+ e^{-i\beta_p^s z} + g_p^- e^{i\beta_p^s z} + \left(\sum_{m\in\mathbb{Z}} K_{m,p}^{\pm} B_m^0\right) e^{\pm i\beta_p^s z}\right] \tag{3.7}$$

where $K_{m,p}^{\pm} = 2(-i)^m \exp\left(\pm im\theta_p\right)/(d\beta_p^s)$, signs + and − corresponding to $z \geq 0$ and $z < 0$, respectively. Setting $X_p^{\pm} = \sum_{m\in\mathbb{Z}} K_{m,p}^{\pm} B_m^0$ and matching fields on slab boundaries yields the solution of $f_p^{a\pm}$, $f_p^{b\pm}$ as a function of $X_p^{\pm}$, as defined in (2.22). Then the substitution into (2.28) generates a linear relation between A_m^0 and B_m^0,

$$A_m^0 = \sum_{n\in\mathbb{Z}} \left(S_{m-n} + \Psi_{m,n}\right) B_n^0 + K_m^0. \tag{3.8}$$

where $\Psi_{m,n}$ is defined as

$$\begin{aligned}\Psi_{m,n} = \sum_{p\in\mathbb{Z}} \Big\{ & J_{m,p}^+ (w_p^b - w_p^s)\left[(w_p^a - w_p^s) e^{i\beta_p^s(a-b)} K_{n,p}^+ - (w_p^a + w_p^s) e^{-i\beta_p^s(a+b)} K_{n,p}^-\right] \\ & - J_{m,p}^- (w_p^a - w_p^s)\left[(w_p^b + w_p^s) e^{i\beta_p^s(a+b)} K_{n,p}^+ - (w_p^b - w_p^s) e^{i\beta_p^s(a-b)} K_{n,p}^-\right]\Big\} / \Lambda_p,\end{aligned} \tag{3.9}$$

the definition of Λ_p, w_p^j, K_m^0 same as in Chapter 2. Together with another relation from the fiber boundary conditions, $B_m^0 = R_m A_m^0 + T_m Q_m^0$, the value of Q_m^0 depending on inner source, the solution of B_m^0 is achieved as

$$\mathbf{B} = \left[\mathbf{I} - \mathbf{R}(\mathbf{S} + \Psi)\right]^{-1} (\mathbf{RK} + \mathbf{TQ}), \tag{3.10}$$

where vectors $\mathbf{B} = [B_m^0]$, $\mathbf{Q} = [Q_m^0]$, matrices $\mathbf{S} = [S_{m-n}]$, $\Psi = [\Psi_{m,n}]$.

The solution of B_m^l follows as

$$B_m^l = B_m^0 \exp(i\alpha_0 l d), \tag{3.11}$$

and $V(\mathbf{r})$ can be easily computed since B_m^l is the key to all expansion coefficients.

3.3 Computation of the Green's function

To get the full solution of the Green's function, meaning that the source and observation position could be anywhere in space, three cases are in consideration, line source outside the laminate, inside the fiber, and in the slab. The first case refers to the approach for the line-source illumination on defectuous laminates in Chapter 2 by assuming no defects. However, the extension to other two cases is stopped by the singularity of the structure

due to the presence of an interior source. Thus the so-called array scanning method [24] is used such that they can be dealt with methods for periodic structures.

3.3.1 Line source outside the laminate

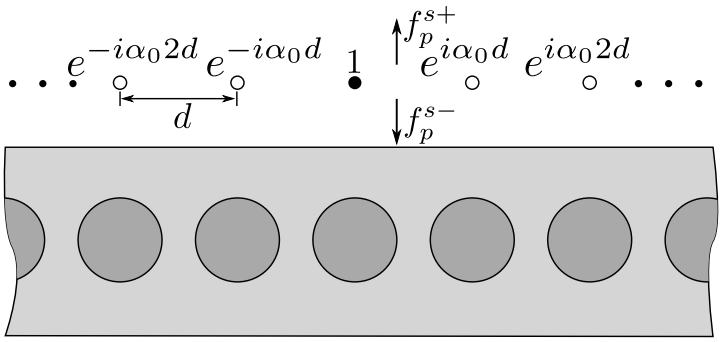

Fig. 3.3 Array scanning method with line source outside the laminate, solid disk denoting the true source and hollow disks the fictitious ones.

The field due to a line source above the laminate is with expression $H_0^{(1)}(k_a|\mathbf{r}-\mathbf{o}_s|)/4i$. In Chapter 2, the PWE of Hankel function has been used. The incident wave simply becomes an integration of plane waves, and the final field is an integration of the field response by each plane-wave component. In contrast, to be consistent with works for a line source inside the fiber or in the slab, the array scanning method (ASM) [24] is used instead.

ASM is run by fabricating an array of quasi-periodic line sources. From both sides of the true line source, fictitious line sources with same current amplitude are periodically positioned along the x-axis with period d. Labeling the true one with 0, the ν-th source is with phase shift $e^{i\alpha_0 \nu d}$. The key then is that, from the identity

$$\frac{d}{2\pi}\int_{-\pi/d}^{\pi/d} e^{i\alpha_0 \nu d}\mathrm{d}\alpha_0 = \delta_\nu, \tag{3.12}$$

the effect of fictitious sources can be canceled, and the true field solution is

$$V(\mathbf{r}) = \frac{d}{2\pi}\int_{-\pi/d}^{\pi/d} V_\infty(\mathbf{r},\alpha_0)\,\mathrm{d}\alpha_0, \tag{3.13}$$

where $V_\infty(\mathbf{r},\alpha_0)$ is the field response to the line-source array. While the integration is carried out via numerical methods, the integrand $V_\infty(\mathbf{r},\alpha_0)$, named the periodic Green's function in [25], can be easily obtained.

The field scattered by the line-source array V_∞^s satisfies the Helmholtz equation

$$\nabla^2 V_\infty^s + k_a^2 V_\infty^s = \sum_{v\in\mathbb{Z}} \delta(\mathbf{r}-\mathbf{o}_s - vd\hat{x}) e^{i\alpha_0 vd}, \tag{3.14}$$

the solution of which in PWE form is

$$V_\infty^s = \sum_{p\in\mathbb{Z}} f_p^{s\pm} e^{i\left[\alpha_p x \pm \beta_p^a (z-a)\right]} \tag{3.15}$$

where $f_p^{s\pm} = \frac{1}{2id\beta_p^a} e^{-i\left[\alpha_p x_s \pm \beta_p^a (z_s - a)\right]}$, $\alpha_p = \alpha_0 + 2\pi/d$, and $\beta_p^a = \sqrt{k_a^2 - (\alpha_p^a)^2}$. "+" and "-" are for $z > z_s$ and $z < z_s$, respectively. Then the field scattered downwards vs. the laminate is treated as incident wave, and V_∞ follows from replacing δ_p in section 3.2 with f_p^{s-} and setting $Q_m^0 = 0$.

3.3.2 Line source inside the fiber

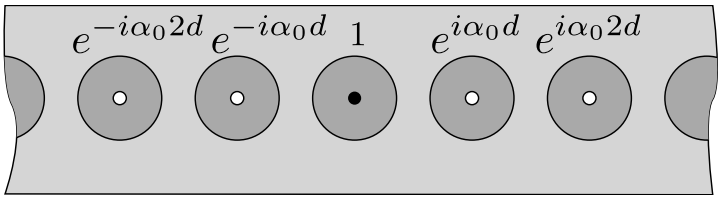

Fig. 3.4 Array scanning method with line source inside the fiber, the solid disk denoting the true source and hollow disks the fictitious ones.

The structure periodicity is destroyed by the additional line source inside the fiber. However, it can be recovered with phased line-source array as an application of ASM as shown in Fig. 3.4. With a phased array, the Floquet theorem is applicable again, *i.e.*, $V(\mathbf{r} + uD\hat{x}) = V(\mathbf{r}) e^{i\alpha_0 uD}$, and the analyzed area can be concentrated on the central cell.

As mentioned before, the scattered field due to the true line source is with expression $V^s = H_0^{(1)}\left(k_f \left|\mathbf{r}-\mathbf{o}_s\right|\right)/4i$, k_f wavenumber of the fiber material. From the Graf's addition theorem with condition $|\mathbf{o}_s| < r_l$, V^s is reformulated as

$$V^s = \sum_{m\in\mathbb{Z}} \left[J_m\left(k_f \left|\mathbf{o}_s\right|\right) e^{-im\arg(\mathbf{o}_s)}/4i\right] g_m^{H^{(1)}}(k_f, \mathbf{r}). \tag{3.16}$$

Remark that $Q_m^l = Q_m^0 e^{i\alpha_0 ld}$ in section 3.2, which indicates that a phased source array is periodically inserted in fibers. Thus V_∞ can be obtained by setting

$$Q_m^0 = J_m\left(k_f \left|\mathbf{o}_s\right|\right) e^{-im\arg(\mathbf{o}_s)}/4i, \tag{3.17}$$

and $\delta_p = 0$ in section 3.2, and the Green's function follows the same integration as (3.13).

3.3.3 Line source in the slab

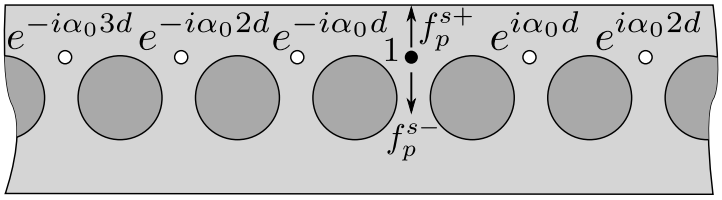

Fig. 3.5 Array scanning method with line source in the slab, the solid disk denoting the true source and hollow disks the fictitious ones.

To apply ASM, the fictitious sources are set as depicted in Fig. 3.5. The additional line-source array disturbs the constitution of the field in the slab. In addition to fields scattered by slab boundaries and the whole set of fibers, the scattered field by the array should be accounted for, which could be expressed as

$$V_\infty^s = \sum_{p\in\mathbb{Z}} f_p^{s\pm} e^{i\left(\alpha_p x \pm \beta_p^s z\right)} \tag{3.18}$$

where $f_p^{s\pm} = \frac{1}{2id\beta_p^s} e^{-i\left(\alpha_p x_s \pm \beta_p^s z_s\right)}$. Thus, the field in the slab is with expression

$$V(\mathbf{r}) = \sum_{p\in\mathbb{Z}} \left[f_p^+ e^{-i\beta_p^s z} + g_p^- e^{i\beta_p^s z} \right] e^{i\alpha_p x} + \sum_{p\in\mathbb{Z}} \left(\sum_{m\in\mathbb{Z}} K_{m,p}^{\pm} B_m^0 + f_p^{s\pm} \right) e^{i\left(\alpha_p x \pm \beta_p^s z\right)}. \tag{3.19}$$

"+" is for $z > \max\{z_s, 0\}$, "-" for $z < \min\{z_s, 0\}$. Since there is no incident wave outside the laminate, δ_p equals 0. Matching the field at slab boundaries, the solution of g_p^-, f_p^+, r_p and t_p is calculated by updating $X_p^{\pm} = \sum_{m\in\mathbb{Z}} K_{m,p}^{\pm} B_m^0 + f_p^{s\pm}$ in (2.22a)–(2.22d).

Changes are also happening on the Rayleigh identities, since the incident wave upon the fiber should include the effect of the array. The scattered field by the ν-th line source in CWE is $H_0^{(1)}(k_s|\mathbf{r}-\mathbf{o}_s|)e^{i\alpha_0 \nu d}/4i$. With the application of the Graf's addition theorem, the field scattered by the array is

$$V_\infty^s = \sum_{m\in\mathbb{Z}} \Pi_m g_m^J(k_s, \mathbf{r}), \tag{3.20}$$

where

$$\Pi_m = \frac{1}{4i} \sum_{\nu\in\mathbb{Z}} H_m^{(1)}(k_s|\mathbf{o}_s|) e^{-im\arg(\mathbf{o}_s)} e^{i\alpha_0 \nu d}.$$

Thus the formula in (3.8) is updated as

$$A_m^0 = \sum_{p\in\mathbb{Z}} \left(J_{m,p}^+ g_p^- + J_{m,p}^- f_p^+ \right) + \sum_{n\in\mathbb{Z}} S_{m-n} B_n^0 + \Pi_m. \tag{3.21}$$

Inserting the expression of g_p^- and f_p^+ into (3.21), we get the new Rayleigh identities,

$$A_m = \sum_{n\in\mathbb{Z}} \Psi_{m,n} B_n + \sum_{n\in\mathbb{Z}} S_{m-n} B_n + \Gamma_m + \Pi_m, \tag{3.22}$$

where $\Psi_{m,n} = \Psi_{m,n}^0$ and the definition of Γ_m is

$$\begin{aligned} \Gamma_m = & i^m \sum_{p\in\mathbb{Z}} \left\{ f_p^{s-} e^{-i\beta_p^s b} \left(w_p^s - w_p^b \right) \left[w_p^s \cos\left(\beta_p^s a + m\theta_p \right) - i w_p^a \sin\left(\beta_p^s a + m\theta_p \right) \right] + \right. \\ & \left. f_p^{s+} e^{i\beta_p^s a} \left(w_p^s - w_p^a \right) \left[w_p^s \cos\left(\beta_p^s b + m\theta_p \right) + i w_p^b \sin\left(\beta_p^s b + m\theta_p \right) \right] \right\} / \Lambda_p. \end{aligned} \tag{3.23}$$

Together with another relation $B_m = R_m A_m$, B_m is such that

$$\mathbf{B} = (\mathbf{I} - \mathbf{RS} - \mathbf{R}\Psi)^{-1} \mathbf{R} (\Gamma + \Pi) \tag{3.24}$$

where vectors $\Gamma = [\Gamma_m]$, $\Pi = [\Pi_m]$.

3.4 Equivalence theory

Let us change the investigated object to the damaged laminate with missing, displaced, expanded, shrunk fibers and circular inclusions. According to the Huygens equivalence theory [43], the effects due to damages is equivalent to adding currents on the surface of anomalous parts. However, the quantification of the currents is not easy. Here, the concerned defects enjoy circular shapes and, benefiting from the proper CWE expressions of fields, simpler equivalence theory is proposed via the utilization of boundary conditions and the Graf's addition theorem.

Assume the l-th fiber is undamaged and express its exterior and interior field in CWEs,

$$V(\mathbf{r}) = \sum_{m\in\mathbb{Z}} \left[a_m^l g_m^J (k_s, \mathbf{r}_l) + b_m^l g_m^{H^{(1)}} (k_s, \mathbf{r}_l) \right], \tag{3.25a}$$

$$V(\mathbf{r}) = \sum_{m\in\mathbb{Z}} \left[c_m^l g_m^J \left(k_f, \mathbf{r}_l \right) + q_m^l g_m^{H^{(1)}} \left(k_f, \mathbf{r}_l \right) \right], \tag{3.25b}$$

Matching fields on the fiber boundary yields linear relations

$$b_m^l = R_m a_m^l + T_m q_m^l \tag{3.26a}$$
$$c_m^l = T_m' a_m^l + R_m' q_m^l, \tag{3.26b}$$

Elements with coefficients b_m^l and q_m^l in (3.25a) and (3.25b) indicate fields scattered by the l-th fiber and the source inside the fiber. q_m^l equal 0 for sound fibers since no inner sources. For damaged ones, defects behave like sources inside corresponding sound fibers, on condition that q_m^l are given required values as seen next.

3.4.1 Scatterings related with defects

For missing fibers, no waves are scattered by them, *i.e.*, $b_m^l = 0$. From (3.26a), we obtain

$$q_m^l = -\frac{R_m}{T_m} a_m^l. \tag{3.27}$$

Since a_m^l are coefficients of the field impinging upon the fiber, it means that if (3.27) is satisfied, in the vicinity of the fiber the reflected field due to the incident wave can be canceled by the transmitted field due to the inner source, and the sound fiber is “missing". Similar relations can be found for other types of defects.

For shrunk/expanded fibers, $c_l \neq c$ and reflection, transmission coefficients are changed, denoted by $\tilde{R}_m^l$ and $\tilde{T}_m^l$ instead. Thus we have

$$b_m^l = \tilde{R}_m^l a_m^l. \tag{3.28}$$

By rewriting it in the form

$$b_m^l = R_m a_m^l + T_m \left[\frac{1}{T_m} \left(\tilde{R}_m^l - R_m \right) \right] a_m^l, \tag{3.29}$$

the expression of q_m^l is obtained as

$$q_m^l = \left[\frac{1}{T_m} \left(\tilde{R}_m^l - R_m \right) \right] a_m^l. \tag{3.30}$$

For the displaced fiber, the center position $\tilde{\mathbf{o}}_l \neq \mathbf{o}_l$. The exterior field of the fiber can be formulated as

$$V(\mathbf{r}) = \sum_{m \in \mathbb{Z}} \left[\tilde{a}_m^l g_m^J (k_s, \tilde{\mathbf{r}}_l) + \tilde{b}_m^l g_m^{H^{(1)}} (k_s, \tilde{\mathbf{r}}_l) \right], \tag{3.31}$$

Applying Graf's addition theorem, (3.31) can be transformed into the expression measured in the local coordinates system originated at $\mathbf{o}_l$, and the expansion coefficients have relations

$$\tilde{a}_m^l = \sum_{n\in\mathbb{Z}} g_{n-m}^J(k_s, \tilde{\mathbf{o}}_l - \mathbf{o}_l) a_n^l, \tag{3.32}$$

$$b_m^l = \sum_{n\in\mathbb{Z}} g_{n-m}^J(k_s, \mathbf{o}_l - \tilde{\mathbf{o}}_l) \tilde{b}_n^l, \tag{3.33}$$

which yields the relation

$$b_m^l = R_m a_m^l + T_m q_m^l, \tag{3.34}$$

where q_m^l satisfies

$$\mathbf{q}^l = \mathbf{T}^{-1}(\mathbf{g}_1 \mathbf{R} \mathbf{g}_2 - \mathbf{R})\,\mathbf{a}^l, \tag{3.35}$$

$\mathbf{q}^l = [q_m^l]$, $\mathbf{g}_1 = [g_{n-m}^J(k_s, \mathbf{o}_l - \tilde{\mathbf{o}}_l]$, $\mathbf{g}_2 = [g_{n-m}^J(k_s, \tilde{\mathbf{o}}_l - \mathbf{o}_l)]$, $\mathbf{R} = \mathrm{diag}\{R_m\}$, $\mathbf{T} = \mathrm{diag}\{T_m\}$, and $\mathbf{a}^l = [a_m^l]$.

With a circular inclusion assumed inside a fiber, as sketched in Fig. 3.6, the field around the inclusion can be expanded as

$$V(\mathbf{r}) = \sum_{m\in\mathbb{Z}} \left[\bar{a}_m g_m^J(k_f, \bar{\mathbf{r}}_l) + \bar{b}_m g_m^{H^{(1)}}(k_f, \bar{\mathbf{r}}_l) \right], \tag{3.36}$$

where $\bar{\mathbf{r}}_l = \mathbf{r} - \bar{\mathbf{o}}_l$. Applying Graf's addition theorem, expansion coefficients are related by

$$\bar{a}_m = \sum_{n\in\mathbb{Z}} g_{n-m}^J(k_f, \bar{\mathbf{o}}_l - \mathbf{o}_l) c_n^l, \tag{3.37}$$

$$q_m^l = \sum_{n\in\mathbb{Z}} g_{n-m}^J(k_f, \mathbf{o}_l - \bar{\mathbf{o}}_l) \bar{b}_n. \tag{3.38}$$

Equation (3.38) is with condition $|\bar{\mathbf{o}}_l - \mathbf{o}_l| < r_l$, *i.e.*, points near the fiber boundary, and (3.37) is valid for the gray region in Fig. 3.6. Considering (3.26b) and the linear relation from the inclusion boundary conditions $\bar{b}_m = \bar{R}_m \bar{a}_m$, q_m^l can be written as a function of a_m^l

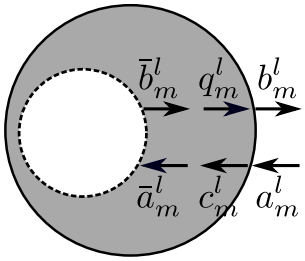

Fig. 3.6 Field representation for analyzing inclusion inside the fiber.

as

$$\mathbf{q}^l = \left[\mathbf{I} - \Phi\mathbf{R}'\right]^{-1} \Phi\mathbf{T}'\mathbf{a}^l \tag{3.39}$$

where $\mathbf{I}$ is the identity matrix, $\mathbf{R}' = \text{diag}\left\{R'_m\right\}$, $\mathbf{T}' = \text{diag}\left\{T'_m\right\}$, $\Phi = [\Phi_{m,n}]$, and

$$\Phi_{m,n} = \sum_{m'\in\mathbb{Z}} \bar{R}^l_{m'} g^J_{m'-m}(k_f, \mathbf{o}_l - \bar{\mathbf{o}}_l) g^J_{n-m'}(k_f, \bar{\mathbf{o}}_l - \mathbf{o}_l). \tag{3.40}$$

Equations (3.27), (3.30), (3.35) and (3.39) can be expressed in general form as

$$\mathbf{q}^l = \Pi^l \mathbf{a}^l, \tag{3.41}$$

where $\Pi^l = \text{diag}\{-R_m/T_m\}$ for missing fiber, $\Pi^l = \mathbf{T}^{-1}(\mathbf{g}_1\mathbf{R}\mathbf{g}_2 - \mathbf{R})$ for the displaced one, $\Pi^l = \text{diag}\left\{\left(\tilde{R}_m - R_m\right)/T_m\right\}$ for the shrunk/expanded one, and $\Pi^l = \left[\mathbf{I} - \Phi\mathbf{R}'\right]^{-1}\Phi\mathbf{T}'$ for the fiber with a circular inclusion inside. Now, since $\mathbf{q}^l$ has been expressed as a function of $\mathbf{a}^l$, to determine the equivalent source, the solution of $\mathbf{a}^l$ is needed.

3.4.2 Strategy to reach the field solution

In section 3.4.1, since defects are treated as sources placed inside sound fibers, the analysis gets to be the one of the undamaged structure. According to linearity of scattering, the field solution due to multiple sources is a summation of the ones when each source is acting independently, *i.e.*,

$$V(\mathbf{r}) = V^{inc}(\mathbf{r}) + \sum_{u\in\mathbb{D}} V^u(\mathbf{r}), \tag{3.42}$$

where V^{inc} is the field contribution from the exterior illuminating source and V^u from the equivalent one inside the u-th fiber. Methods for periodic structures are applicable to solve for V^{inc} [13, 14]. The solution of V^u is achieved through the decomposition based on CWEs.

The field due to the equivalent source is with expansion $\sum_{n\in\mathbb{Z}} q^u_n g^{H^{(1)}}_n(k_f, \mathbf{r}_u)$. Denoting V^u_n as the field response due to the cylindrical wave $g^{H^{(1)}}_n(k_f, \mathbf{r}_u)$, then (3.42) can be rewritten as

$$V(\mathbf{r}) = V^{inc}(\mathbf{r}) + \sum_{u\in\mathbb{D}}\sum_{n\in\mathbb{Z}} q^u_n V^u_n(\mathbf{r}). \tag{3.43}$$

In the vicinity of the fiber, V^{inc} and V^u_n could be expressed in CWEs as V in (3.25a), but with different coefficients, denoted by $a^{l,inc}_m$ and $a^{l,u}_{m,n}$, respectively. Sharing the same expansion bases, the coefficients of V, V^{inc} and V^u_n enjoy the relation

$$a^l_m = a^{l,inc}_m + \sum_{u\in\mathbb{D}}\sum_{n\in\mathbb{Z}} q^u_n a^{l,u}_{m,n},\ l \in \mathbb{D}. \tag{3.44}$$

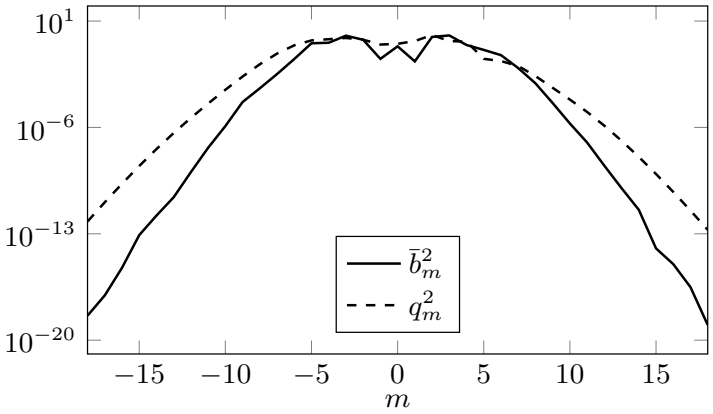

Fig. 3.7 Convergence of $\bar{b}_m^2$ and q_m^2, glass fiber, fiber period $d = 0.1$mm, $c = 0.25d$, $\lambda^{inc} = d/2$, planar-wave illumination with $\theta^{inc} = \pi/6$.

Together with (3.41), the solution of a_m^l is obtained

$$\mathbf{a} = (\mathbf{I} - \Lambda\Pi)^{-1}\,\mathbf{a}^{inc} \tag{3.45}$$

where $\mathbf{a} = [\mathbf{a}^l]$, $\Lambda = [a_{m,n}^{l,u}]$, $\Pi = \text{diag}\left\{\Pi^l\right\}$, and $\mathbf{a}^{inc} = [a_m^{l,inc}]$. Since only the coefficients of damaged fibers are concerned in (3.45) and the number of damaged fibers is small in usual situations, the size of the matrix to be inverted is expected to be bearable.

With the solution of $\mathbf{a}$, back to (3.41), q_m^l, $l \in \mathbb{D}$, can be obtained, and the final field solution follows (3.43). Since the illuminating source and the structure of the undamaged laminate are known in practice, a_m^{inc}, V^{inc}, $a_{m,n}^{l,u}$ and V_n^u can be computed and stored in advance. The method to calculate V^{inc} and a_m^{inc} is available in section 3.2 and the decomposition of sources into plane waves might be needed considering the types of sources. Taking advantage that $V_n^u(\mathbf{r}) = V_n^0(\mathbf{r} - ud\hat{x})$ and $a_{m,n}^{l,u} = a_{m,n}^{l-u,0}$, the computation of V_n^u and $a_{m,n}^{l,u}$ follows the application of ASM in subsection 3.3.2 where Q_m^0 is valued $\delta_{m,n}$.

3.5 Numerical results

The simulations performed here are with a laminate sandwiched by air, $d = 0.1$mm, $c = 0.25d$, $a = -b = d/2$. The matrix material is epoxy with $\Re(\epsilon_{rs}) = 3.6$, loss tangent 0.02 and $\mu_{rs} = 1$. Fibers are of graphite ($\Re\left(\epsilon_{rf}\right) = 12$, conductivity $\sigma = 330$ S/m, $\mu_{rf} = 1$) or glass ($\epsilon_{rf} = 6$, $\mu_{rf} = 1$). All types of defects are in consideration. Specifically, fibers with indexes -3 and 3 are missing, the center of the -1st fiber is displaced to $(-d + 0.2c, 0.2c)$, the 0-th fiber shrinks with $c_0 = 0.7c$, an air inclusion is inside the 2nd fiber with $\bar{\mathbf{o}}_2 = (2d + 0.1c, 0.1c)$, $\bar{c}_2 = 0.7c$.

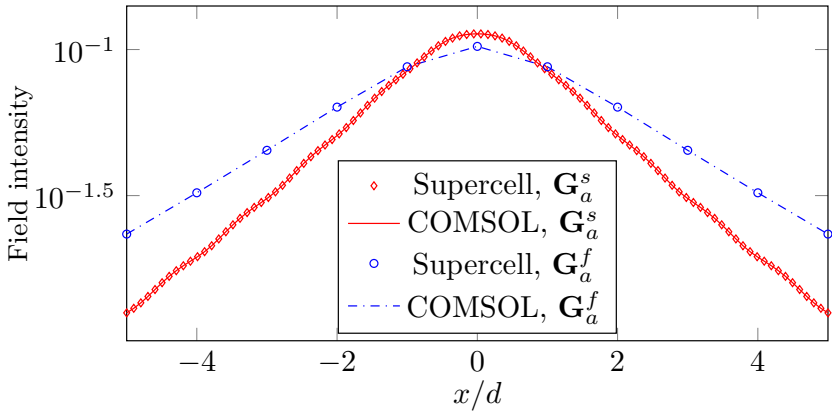

Fig. 3.8 Validation of the computation of the Green's function by comparing with COMSOL when the line source is above the laminate, $\mathbf{G}_a^s$ field values sampled in the slab with $z = 0.37d$, $-5d \leq x \leq 5d$, $\mathbf{G}_a^f$ at fiber centers.

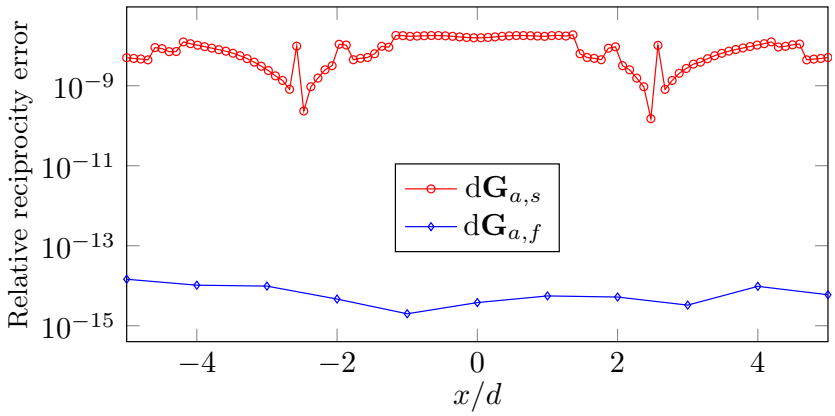

Fig. 3.9 Validation of the computation of the Green's function in cases with line source in the slab and fiber by checking reciprocity.

CWEs and PWEs, as infinite series, can be accurately approximated by their truncations in the analysis. Assuming a planar wave with unit amplitude illuminates the damaged laminate with angle $\theta^{inc} = \pi/6$, measured counter-clockwise from the z axis, absolute values of $\bar{b}_m^2$ and q_m^2 are shown in Fig. 3.7, where the amplitudes of coefficients exponentially decrease with increasing $|m|$ and the convergence rate of q_m^2 is slower than that of $\bar{b}_m^2$ due to the transformation in (3.38) with the Graf's addition theorem. Let us truncate CWEs and PWEs as $\sum_{m=-M}^{M}$ and $\sum_{m=-P}^{P}$, respectively. The strategy in subsection 2.7.1 is used to decide on M and P, where the knowledge that field values at Ω_s calculated from CWE and PWE should be the same is employed.

Accuracy of the computed Green's function, when the line source is above the laminate, is exhibited in Fig. 3.8. The laminate is with graphite fibers and the wavelength $\lambda^{inc} = 10d$.

The Green's function is the response of the sound laminate, approximated by an object including 51 fibers with the 2nd configuration in COMSOL. The line source position is $\mathbf{o}_s = (0, a+d)$. $\mathbf{G}_a^s$ is computed along the line in the slab with $z = 0.37d$, $-5d \le x \le 5d$, and $\mathbf{G}_a^f$ at -5th to 5th fiber centers, subscript a indicating source location. Results in Fig. 3.8 show that COMSOL and the supercell approach fit well with a line-source exterior illumination.

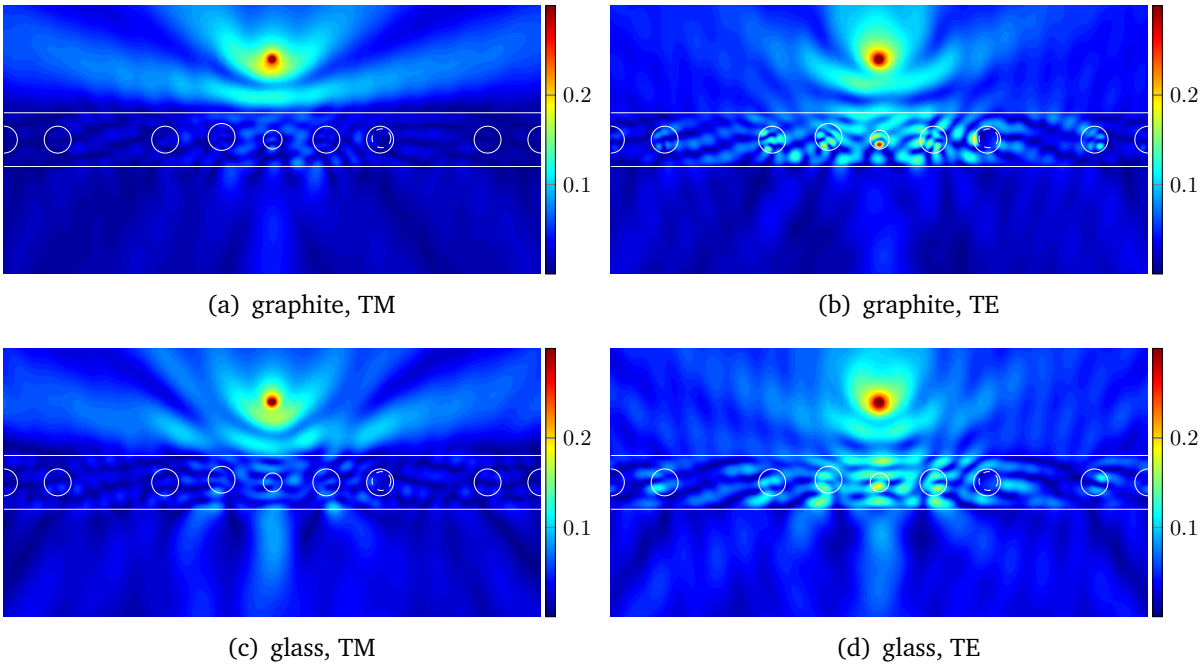

(a) graphite, TM (b) graphite, TE

(c) glass, TM (d) glass, TE

Fig. 3.10 Intensity of electric field in TM cases and magnetic field in TE cases with the illumination by the line source at $\mathbf{r}_s = (0, a+d)$, $\lambda^{inc} = d$.

When the line source is in the matrix or inside the fiber, the modeling accuracy is checked by testing for the reciprocity theorem. Since the materials are nonmagnetic, upon exchanging positions of source and observation, data should be the same. Let us define the relative reciprocity error $\mathrm{d}\mathbf{G}_{a,f} = \left|\mathbf{G}_a^f - \mathbf{G}_f^a\right| / \left|\mathbf{G}_a^f\right|$, with similar definition for $\mathrm{d}\mathbf{G}_{a,s}$. Results are shown in Fig. 3.9. The relative error is below 10^{-7}, even 10^{-13} for samples at fiber centers. Considering computation accuracy, the reciprocity theorem is checked.

A line-source at $\mathbf{r}_s = (0, a+d)$ excites the field $H_0^{(1)}(k_a r_s)/(4i)$ with wavelength $\lambda^{inc} = d$, $r_s = |\mathbf{r} - \mathbf{r}_s|$. Corresponding results are shown in Fig. 3.10, where the structure of the laminate is indicated by white lines and the amplitude is limited from 0 to 0.3 for easier appraisal. As is seen, the field smoothly propagates through the region of missing fibers. In TE cases, since the slab permittivity is larger than the one of air, the magnetic field is transmitted into the slab, but hardly emerges from it, which is seen from the boundary

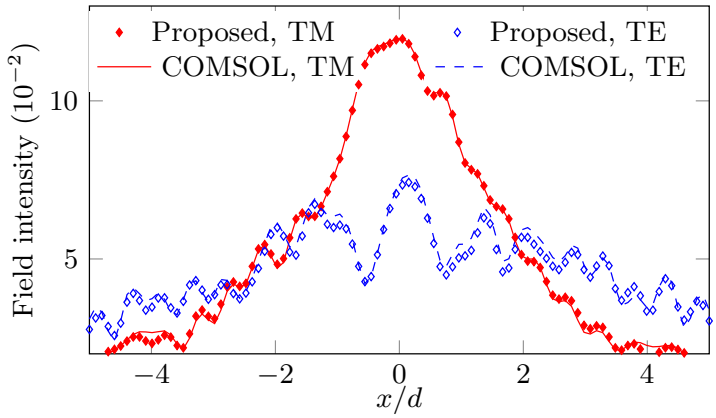

(a) graphite

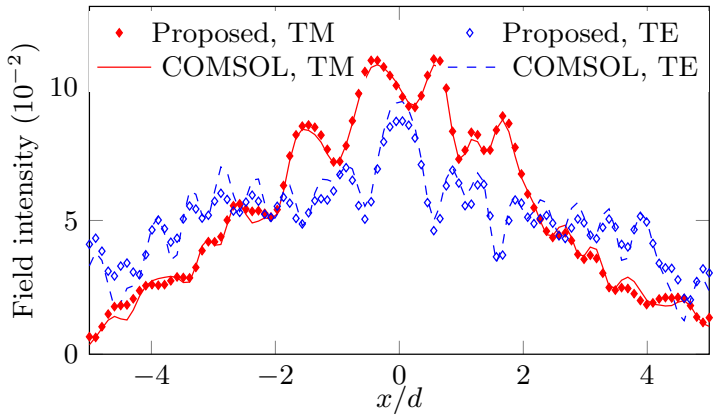

(b) glass

Fig. 3.11 Validation of the proposed modeling approach by comparing with COMSOL, line source at $\mathbf{r}_s = (0, a+d)$, $\lambda^{inc} = d$, field values sampled along $z = 0.75d$, $-5d \leq x \leq 5d$.

conditions. For the same reason, peak amplitudes are exhibited inside the fibers while a hole appears at the position of the air inclusion. This phenomenon does not arise in the TM case, since μ_j are equal in different regions.

Due to different permittivities, the resonance of the TE magnetic field in the slab is stronger than the one of the TM electric field, thus strong oscillations appear in the sampled field values along the line $-5d \leq x \leq 5d$, $z = 0.75d$, as shown in Fig. 3.11(a) and 3.11(b). Comparing with the FEM software COMSOL, where a finite object with 33 graphite fibers or 101 glass ones (including damaged ones) inserted is modeled and no periodic conditions are set at the side boundaries, good fits are observed, save small discrepancies at some points which might be caused by the approximated modeling object in COMSOL.

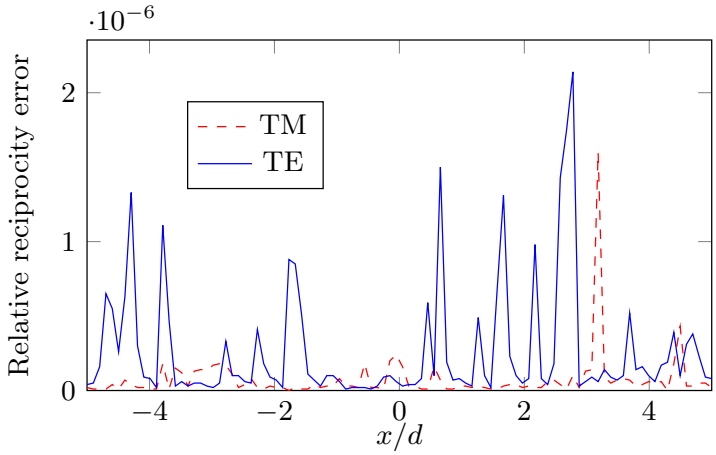

(a) graphite

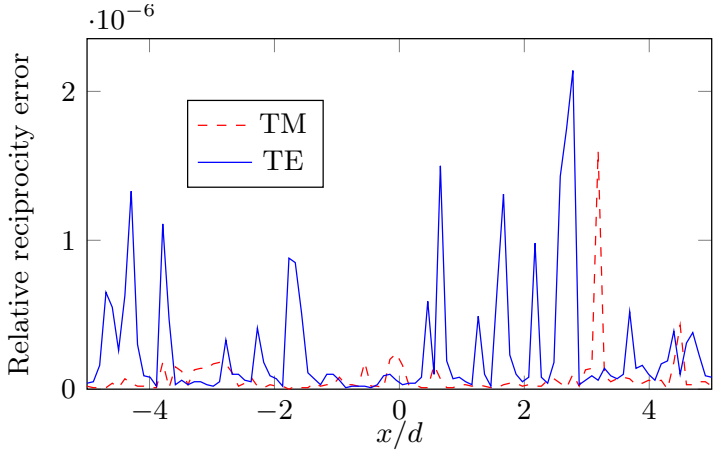

(b) glass

Fig. 3.12 Checking the reciprocity by exchanging the position of line source and observation points at Fig. 3.11, $\lambda^{inc} = d$.

Upon exchanging positions of source and observation, the relative reciprocity error $\tau = |V(\mathbf{r},\mathbf{r}_s) - V(\mathbf{r}_s,\mathbf{r})| \,/\, |V(\mathbf{r},\mathbf{r}_s)|$, where $V(\mathbf{r},\mathbf{r}_s)$ denotes the field value at $\mathbf{r}$ due to the source at $\mathbf{r}_s$, is less than 3×10^{-6}, as shown in Fig. 3.12.

About the efficiency of the proposed method, to obtain the results in Fig. 3.11(a) and 3.11(b) on a laptop (dual cores, clock speeds 2.9 GHz, memory 16 GB), less than 50 milliseconds are needed for each line graph. In comparison, $6 \sim 10$ seconds are required for graphite-fiber laminate with COMSOL, and more time, $10 \sim 17$ seconds, for glass-fiber one since glass is assumed lossless ($\sigma < 10^{-10}$ S/m in practice) and more fibers have to be modeled.

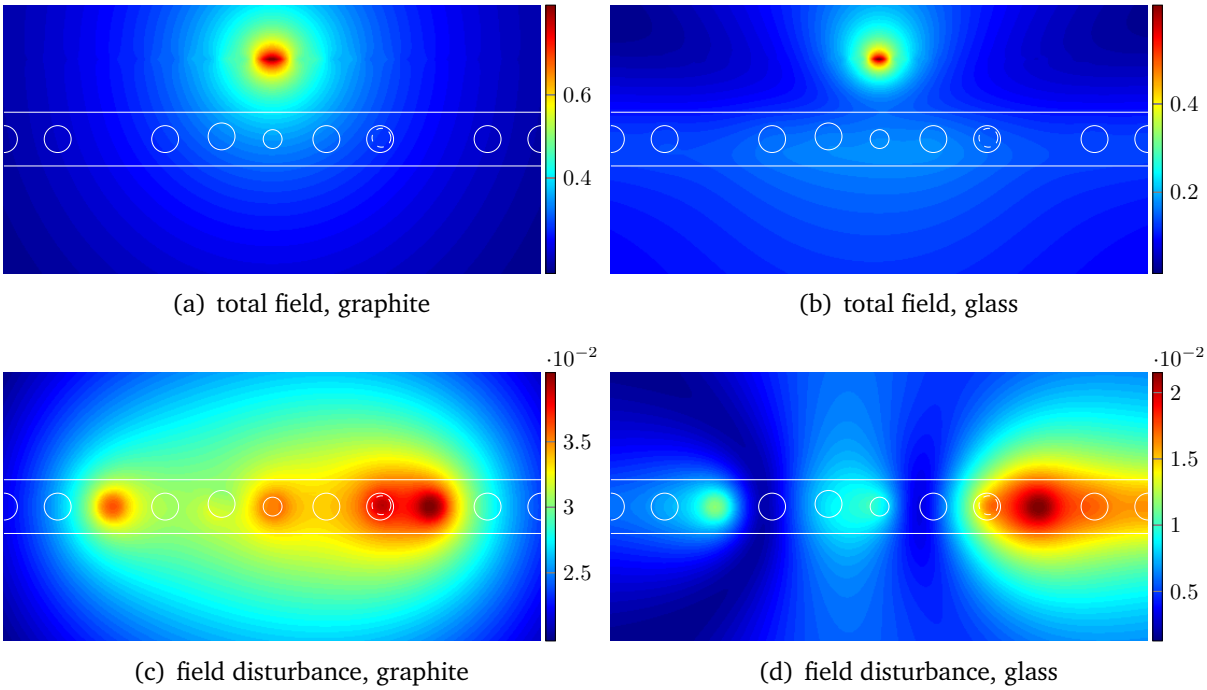

(a) total field, graphite (b) total field, glass

(c) field disturbance, graphite (d) field disturbance, glass

Fig. 3.13 Intensity of total field and field disturbance in sub-THz TM cases, line source at $\mathbf{r}_s = (0, a+d)$, $\lambda^{inc} = 100d$ with (a) and (c), $\lambda^{inc} = 10d$ with (c) and (d).

Sources below THz are often chosen because of lower cost and possibly better control. Fig. 3.13(a) shows the field response when the frequency $f = 30$ GHz and fiber material is graphite. Since the wavelength is much larger than the laminate thickness, $\lambda^{inc} = 100d$, almost no impacts show up on the wave propagation. Fig. 3.13(b) is with $f = 300$ GHz and glass fiber. The contour of the exciting wave is distorted by the laminate, but it is still hard to identity the locations of defects. Maps of field disturbance could clearly show the impact of the defects. From Fig. 3.13(c) and 3.13(d), we see that defects behave as sources and their scattering fields might merge as one beam due to small intervals (relative to the wavelength). Any region where defects impact a lot is revealed by these maps and the position of receivers could be set accordingly for purpose of imaging.

The Born approximation is often used in imaging to linearize the non-linear inverse problem [18] and the resulting modeling errors should be estimated. Field disturbances with missing fibers from the Born approximation are computed in the way illustrated in Appendix B and comparisons with the true solution, provided by the proposed approach, are shown in Fig. 3.14(a) and 3.14(b). The $-$3rd and 3rd fibers are missing. As is seen, peaks show up at corresponding positions and the Born approximation can yield a well-approximated solution with glass fiber and a smaller one when fiber is graphite.

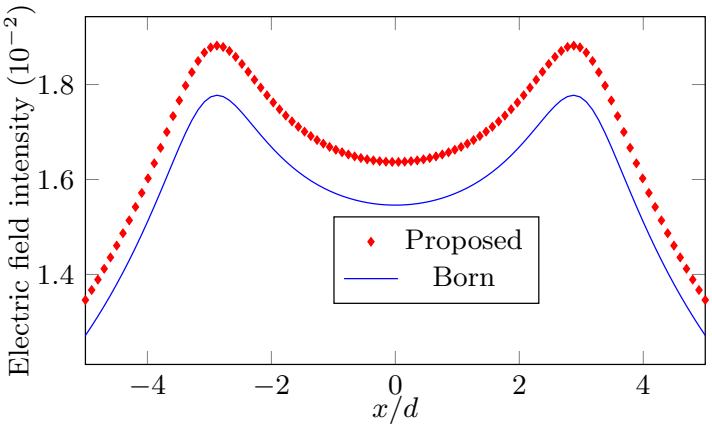

(a) graphite

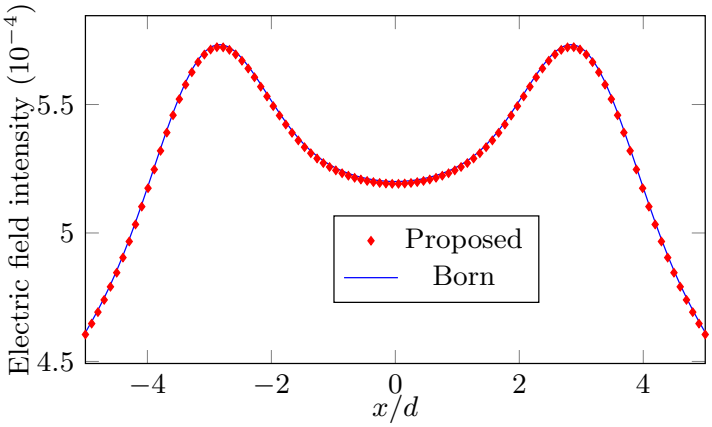

(b) glass

Fig. 3.14 Comparisons with results from the Born approximation, line source at $\mathbf{r}_s = (0, a + d)$, $\lambda^{inc} = 100d$, TM polarization, field values sampled along $z = 0.75d$, $-5d \leq x \leq 5d$.

Comparisons with the supercell approach, which was presented in chapter 2, is made. Assume fibers with indexes -5 and 5 are missing, the center of the -3rd fiber is displaced to $(-3d + 0.2c, 0.2c)$, the 0-th fiber shrinks with $c_0 = 0.7c$, an air inclusion is inside the 2nd fiber with $\bar{\mathbf{o}}_2 = (2d + 0.55c, 0.55c)$, $\bar{c}_2 = 0.2c$. With a planar-wave illumination, $\theta^{inc} = \pi/6$, the scattered fields computed by the equivalence theory and supercell (number of included fibers $L = 33$) approach are plotted in Fig. 3.15, where field values are sampled along $z = d$, $-10 \leq x \leq 10d$. As observed, results fit very well and these fits validates both the equivalence theory and supercell approach.

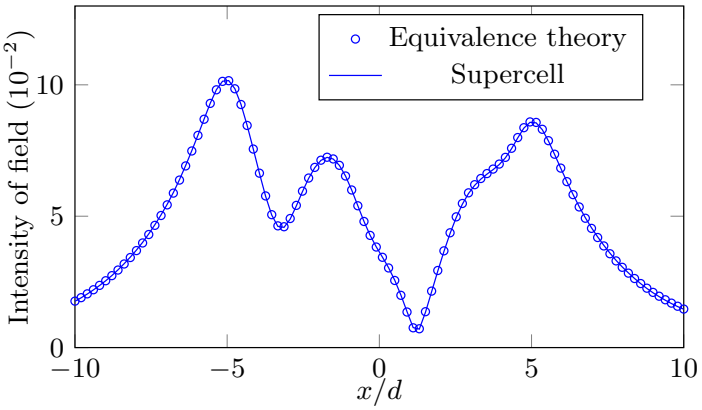

Fig. 3.15 Comparisons with results from the supercell approach, graphite fiber and epoxy slab, TM planar wave with $\theta^{inc} = \pi/6$, $\lambda^{inc} = 10d$, , field values sampled along $z = d$, $-10d \leq x \leq 10d$.

3.6 Summary

This chapter has been divided into two parts, the computation of the Green's function and modeling of damaged laminates with a variety of defects. The former deals with three cases (source above the laminate, in the slab or fiber) trying to access the full solution of the Green's function. The array scanning method is used where different phases are put on the periodic duplications of the source to have a quasi-periodic field distribution, the solution of which applies the method for periodic structures. The final solution follows an integration, after that effects from duplicated (or fictitious) sources are canceled.

Equivalence theory is applied to the fast and accurate modeling of damaged laminates affected by circular defects. The field disturbance due to these defects is equivalent to inserting fictitious line sources inside sound fibers. By decomposing the field response based on CWEs, the equivalent sources are determined and the field is a summation of solutions due to the exterior source and equivalent ones. Validations are realized through comparisons with COMSOL, while the accuracy is further checked by testing the reciprocity.

The present works establish a bridge between modeling damaged and undamaged periodic fiber-based laminates. Once some quantities computed with the undamaged structure, the field solution for the damaged one follows the computations in (3.43) and (3.45), emphasizing that no approximation is made. Since enjoying similar features, illumination of disorganized photonic crystals could be analyzed likewise.

Chapter 4

Modeling of multilayer damaged laminates with equivalence theory

In chapter 3, scatterings of single-layer laminates affected by a variety of defects are analyzed with equivalence theory. The extension to multilayer structures is made in this chapter, fiber orientations and periods in different layers, however, being restricted to be the same. As has been presented, defects are modeled as sources inside the initially sound fibers and the field is a summation of responses due to the incident wave and equivalent sources. While the exterior illumination can be analyzed through the combination of quasi-periodic theories described in section 3.2 and scattering matrices, which indicate mutual scatterings between layers, the inner sources are studied with the array scanning method. TM and TE polarized waves with defects as missing, displaced, shrunk, expanded fibers and circular inclusions inside fibers are in consideration. Modeling accuracy and efficiency are demonstrated by numerical results.

4.1 Configuration and formulation

Configurations of the undamaged structure is presented first and defects are then specifically described. The structure of the concerned multilayer laminate is sketched in Figure 4.1. Sandwiched by two half spaces from the top and bottom, each layer of the laminate is composed by periodically inserting same-oriented fibers inside a planar slab. In different layers, fiber radius, slab thickness and their composed materials can differ, but the same period is forced.

Assume L layers are stacked. Labeling them with integrals from 1 to L, the upper and lower half spaces are with indexes 0 and $L+1$, respectively, for convenience. Set the origin

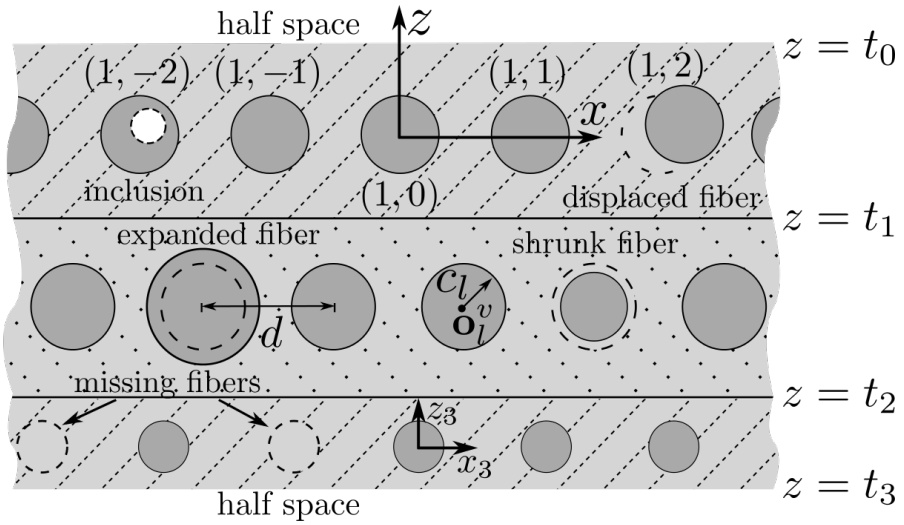

Fig. 4.1 Sketch of the damaged laminate with defects of concern, number of layers $L = 3$.

of the global coordinates system at the center of a sound fiber in the 1st layer and the local ones for each layer at the fiber centers $\mathbf{o}_l = (x_l^0, z_l^0)$ with conditions $t_{l+1} < z_l^0 < t_l$, $-d/2 < x_l^0 \leq d/2$, $z = t_l$ the lower boundary of the l-th layer and d fiber period. Indexing fibers in the l-th layer with integer couples (l, v), $v \in \mathbb{Z}$, the center of the (l, v)-th fiber $\mathbf{o}_l^v = (x_l^0 + vd\hat{x}, z_l^0)$, $\hat{x}$ unit vector along the x axis and all fibers in the l-th layer share same radius c_l.

Introducing defects, indexes of damaged fibers compose the set $\mathbb{D}$, *i.e.*, the v-th fiber in the l-th layer is damaged if $(l, v) \in \mathbb{D}$. A tilde is above notations related with damaged fibers, so for displaced ones $\tilde{\mathbf{o}}_l^v \neq (x_l^0 + vd\hat{x}, z_l^0)$, $\tilde{c}_l^v \neq c_l$ for the shrunk/expanded ones. Circular inclusion is indicated by its center $\bar{\mathbf{o}}_l^v$ and radius $\bar{c}_l^v$, a bar above corresponding notations.

All components, including inclusions, are linear, isotropic and homogeneous. Without losing the generality, half spaces and inclusions are assumed to be filled by air and missing fibers are “fibers" sharing the same material with the background slab. Fiber and slab materials are layer-dependent, characterized by permittivities ϵ_j^l (complex value for lossy cases) and permeabilities μ_j^l, $j = f$ standing for fiber and $j = s$ for slab.

With time dependence $\exp(-i\omega t)$, i imaginary unit, ω angular frequency, Transverse Magnetic (TM) electric fields or Transverse Electric (TE) magnetic fields are considered, which indicates a scalar scattering problem.

4.2 Field solution for exterior illuminations

Since different types of sources could be dealt by exploiting their plane-wave-expansions (PWEs) [19, 44], plane-wave illuminations are the only ones considered. For each layer, fields are expressed in CWEs or PWEs and behaviors of fiber array and slab boundaries are analyzed via multipole method and field matching, respectively. Scattering matrices, which indicate mutual scatterings between different layers, are computed by a recursive scheme and used to retrieve expansion coefficients in any layer.

4.2.1 Scattering matrix of fiber array and slab boundary

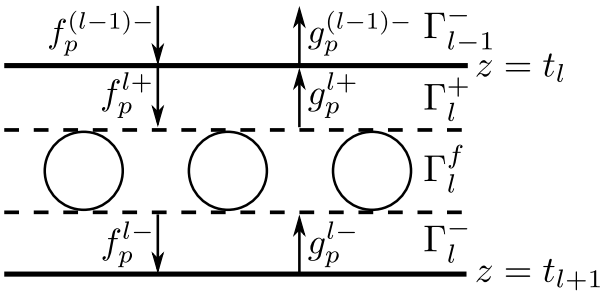

Fig. 4.2 Expansion of fields near slab boundaries into planar waves.

The fiber array divides each layer into three slices, region above the array $z_l^0 + c_l < z < t_l$, below it $t_{l+1} < z < z_l^0 - c_l$, and itself $z_l^0 - c_l < z < z_l^0 + c_l$, denoted by Γ_l^+, Γ_l^- and Γ_l^f, respectively. The Floquet theorem indicates the property $V(\mathbf{r} + d\hat{x}) = V(\mathbf{r})e^{i\alpha_0 d}$, based on which, as shown in Figure 4.2, fields in Γ_l^+ and Γ_l^- are expressed in PWEs as

$$V(\mathbf{r}) = \sum_{p\in\mathbb{Z}} \left[f_p^{l\pm} e^{-i\beta_p^l z_l} + g_p^{l\pm} e^{i\beta_p^l z_l} \right] e^{i\alpha_p x_l}. \tag{4.1}$$

where $\alpha_p = \alpha_0 + p2\pi/d$, $\alpha_0 = k_s^0 \sin\theta^{inc}$, k_s^0 being the wavenumber of the upper half space where the illumination comes from and θ^{inc} the incident angle which is measured counter-clockwise from the z axis. $\beta_p^l = \sqrt{(k_s^l)^2 - \alpha_p^2}$ defined in the top Riemann sheet ($\Im(\beta_p^l) > 0$). Signs "+", "−" correspond to Γ_l^+ and Γ_l^-, respectively.

Matching fields at the slab boundary $z = t_l$, expansion coefficients at two sides of the boundary have the relation

$$\begin{bmatrix} \mathbf{f}^{l+} \\ \mathbf{g}^{(l-1)-} \end{bmatrix} = \begin{bmatrix} \mathscr{D}^1_{(l-1)-,l+} & \mathscr{D}^2_{(l-1)-,l+} \\ \mathscr{D}^3_{(l-1)-,l+} & \mathscr{D}^4_{(l-1)-,l+} \end{bmatrix} \begin{bmatrix} \mathbf{f}^{(l-1)-} \\ \mathbf{g}^{l+} \end{bmatrix}. \tag{4.2}$$

where $\mathbf{f}^{l\pm}=[f_p^{l\pm}]$, $\mathbf{g}^{l\pm}=[g_p^{l\pm}]$, $\mathscr{D}^j_{(l-1)-,l+}=[\mathscr{D}^{j,p}_{(l-1)-,l+}]$, $j=1,2,3,4$, and

$$\mathscr{D}^{1,p}_{(l-1)-,l+}=\frac{2w_p^{l-1}e^{i\alpha_p(x_l^0-x_{l-1}^0)}e^{i\left[\beta_p^l(t_{l-1}-z_l^0)-\beta_p^{l-1}(t_{l-1}-z_{l-1}^0)\right]}}{w_p^{l-1}+w_p^l}$$
$$\mathscr{D}^{2,p}_{(l-1)-,l+}=\frac{-(w_p^{l-1}-w_p^l)e^{i2\beta_p^l(t_{l-1}-z_l^0)}}{w_p^{l-1}+w_p^l}$$
$$\mathscr{D}^{3,p}_{(l-1)-,l+}=\frac{(w_p^{l-1}-w_p^l)e^{-i2\beta_p^{l-1}(t_{l-1}-z_{l-1}^0)}}{w_p^{l-1}+w_p^l}$$
$$\mathscr{D}^{4,p}_{(l-1)-,l+}=\frac{2w_p^{l}e^{-i\alpha_p(x_l^0-x_{l-1}^0)}e^{i\left[\beta_p^l(t_{l-1}-z_l^0)-\beta_p^{l-1}(t_{l-1}-z_{l-1}^0)\right]}}{w_p^{l-1}+w_p^l}$$

where $w_p^l=\beta_p^l/\mu_s^l$ for TM cases and $w_p^l=\beta_p^l/\epsilon_s^l$ for TE ones. Since $\mathbf{f}^{l+}$, $\mathbf{g}^{(l-1)-}$ stand for waves scattered by the boundary and $\mathbf{f}^{(l-1)-}$, $\mathbf{g}^{l+}$ for incident ones, the matrix composed by $\mathscr{D}^j_{(l-1)-,l+}$ reveals the scattering property of the slab boundary. Such relation could be found among coefficients $\mathbf{f}^{l\pm}$, $\mathbf{g}^{l\pm}$ by analyzing the fiber array.

Let us express the total field in the vicinity of and inside the (l,v)-th fiber, respectively, as

$$V(\mathbf{r})=\sum_{m\in\mathbb{Z}}\left[a_m^{(l,v)}g_m^J\left(k_s^l,\mathbf{r}_l^v\right)+b_m^{(l,v)}g_m^{H^{(1)}}\left(k_s^l,\mathbf{r}_l^v\right)\right], \tag{4.3a}$$
$$V(\mathbf{r})=\sum_{m\in\mathbb{Z}}\left[c_m^{(l,v)}g_m^J\left(k_f^l,\mathbf{r}_l^v\right)+q_m^{(l,v)}g_m^{H^{(1)}}\left(k_f^l,\mathbf{r}_l^v\right)\right], \tag{4.3b}$$

where $\mathbf{r}_l^v$ is the relative position of the observation point $\mathbf{r}$ with respect to $\mathbf{o}_l^v$, *i.e.*, $\mathbf{r}_l^v=\mathbf{r}-\mathbf{o}_l^v$. $g_m^Z(k_j^l,\mathbf{r}_l^v)=Z_m(k_j,r_l^v)\exp(im\theta_l^v)$, (r_l^v,θ_l^v) polar coordinates of $\mathbf{r}_l^v$. Terms with Hankel functions stand for the waves scattered by the fiber (with coefficients $b_m^{(l,v)}$) or inner source (with $q_m^{(l,v)}$). Thus the contribution from the whole set of fibers in the l-th layer is

$$V_f^l(\mathbf{r})=\sum_{v\in\mathbb{Z}}\sum_{m\in\mathbb{Z}}b_m^{(l,0)}e^{i\alpha_0vd}g_m^{H^{(1)}}\left(k_s^l,\mathbf{r}_l^0-vd\hat{x}\right), \tag{4.4}$$

where the knowledge that $b_m^{(l,v)}=b_m^{(l,0)}e^{i\alpha_0vd}$ is made use of. The PWE form is

$$V_f^l(\mathbf{r})=\sum_{p\in\mathbb{Z}}\left(\sum_{m\in\mathbb{Z}}K_{m,p}^{l\pm}b_m^{(l,0)}\right)e^{i(\alpha_px_l\pm\beta_p^lz_l)}, \tag{4.5}$$

where $K_{m,p}^{l\pm} = 2(-i)^m \exp\left(\pm im\theta_p^l\right)/(d\beta_p^l)$, $\cos\theta_p^l = \alpha_p/k_s^l$. Signs + and − correspond to $z_l \geq 0$ and $z_l < 0$, respectively.

The field in the l-layer is composed by fields scattered by upper, lower slab boundaries and all fibers. The first two are valued by their PWEs with coefficients $\mathbf{f}^{l+}$ and $\mathbf{g}^{l-}$. Thus the total field in the l-th layer is

$$V(\mathbf{r}) = \sum_{p\in\mathbb{Z}} e^{i\alpha_p x_l}\left[f_p^{l+}e^{-i\beta_p^l z_l} + g_p^{l-}e^{i\beta_p^l z_l} + \left(\sum_{m\in\mathbb{Z}} K_{m,p}^{l\pm} b_m^{(l,0)}\right)e^{\pm i\beta_p^l z_l}\right]. \tag{4.6}$$

The comparison with (4.1) yields relations

$$\mathbf{g}^{l+} = \mathbf{g}^{l-} + \sum_{m\in\mathbb{Z}} K_{m,p}^{l+} b_m^{(l,0)}, \tag{4.7a}$$

$$\mathbf{f}^{l-} = \mathbf{f}^{l+} + \sum_{m\in\mathbb{Z}} K_{m,p}^{l-} b_m^{(l,0)}. \tag{4.7b}$$

The relation between $b_m^{(l,0)}$ and $\mathbf{f}^{l+}$, $\mathbf{g}^{l-}$ is then explored below by analyzing the fiber array with multipole method.

The field incident on the (l,v)-th fiber is composed by incident waves from $\Gamma_l^{\pm}$ and scattered fields by all other fibers in the l-th layer. Correspondingly, with the Jacobi-Anger expansion and application of the Graf's addition theorem, Rayleigh identities [25] are obtained,

$$a_m^{(l,0)} = \sum_{n\in\mathbb{Z}} S_{m-n}^l b_n^{(l,0)} + \sum_{p\in\mathbb{Z}}\left(J_{m,p}^{l+}\mathbf{g}^{l-} + J_{m,p}^{l-}\mathbf{f}^{l+}\right), \tag{4.8}$$

where $J_{m,p}^{l\pm} = (i)^m \exp(\mp im\theta_p^l)$ and S_{m-n}^l is the lattice sum. From fiber boundary conditions, coefficients in (4.3) are related by

$$b_m^{(l,v)} = R_m^l a_m^{(l,v)} + T_m^l q_m^{(l,v)}, \tag{4.9a}$$

$$c_m^{(l,v)} = T_m^{l,\prime} a_m^{(l,v)} + R_m^{l,\prime} q_m^{(l,v)}, \tag{4.9b}$$

where R_m^l, $R_m^{l,\prime}$, T_m^l, $T_m^{l,\prime}$ are reflection or transmission coefficients similarly defined as (2.35). Since no inner source is considered, $q_m^{(l,v)} = 0$ and we have $b_m^{(l,0)} = R_m^l a_m^{(l,0)}$. Combining it with (4.8), the solution for $\mathbf{b}^{(l,0)}$ is obtained as

$$\mathbf{b}^{(l,0)} = \left(\mathbf{I} - \mathbf{R}^l\mathbf{S}^l\right)^{-1}\mathbf{R}^l\left(\mathbf{J}^{l+}\mathbf{g}^{l-} + \mathbf{J}^{l-}\mathbf{f}^{l+}\right), \tag{4.10}$$

where $\mathbf{b}^{(l,0)} = [b_m^{(l,0)}]$, $\mathbf{R}^l = \text{diag}\{R_m^l\}$, $\mathbf{S}^l = [S_{m-n}^l]$, $\mathbf{J}^{l\pm} = [J_{m,p}^{l\pm}]$. The substitution of (4.10) into (4.7a) and (4.7b) generates the scattering matrix of the fiber array,

$$\begin{bmatrix} \mathbf{f}^{l-} \\ \mathbf{g}^{l+} \end{bmatrix} = \begin{bmatrix} \mathscr{D}_{l-,l+}^1 & \mathscr{D}_{l-,l+}^2 \\ \mathscr{D}_{l-,l+}^3 & \mathscr{D}_{l-,l+}^4 \end{bmatrix} \begin{bmatrix} \mathbf{f}^{l+} \\ \mathbf{g}^{l-} \end{bmatrix}, \tag{4.11}$$

where $\mathscr{D}_{l-,l+}^1 = \mathbf{I} + \Omega^{l-}\mathbf{R}^l\mathbf{J}^{l-}$, $\mathscr{D}_{l-,l+}^2 = \Omega^{l-}\mathbf{R}^l\mathbf{J}^{l+}$, $\mathscr{D}_{l-,l+}^3 = \Omega^{l+}\mathbf{R}^l\mathbf{J}^{l-}$, $\mathscr{D}_{l-,l+}^4 = \mathbf{I} + \Omega^{l+}\mathbf{R}^l\mathbf{J}^{l+}$, $\Omega^{l\pm} = \mathbf{K}^{l\pm}\left(\mathbf{I} - \mathbf{R}^l\mathbf{S}^l\right)^{-1}$, $\mathbf{K}^{l\pm} = [K_{m,p}^{l\pm}]$.

4.2.2 Recursive scheme

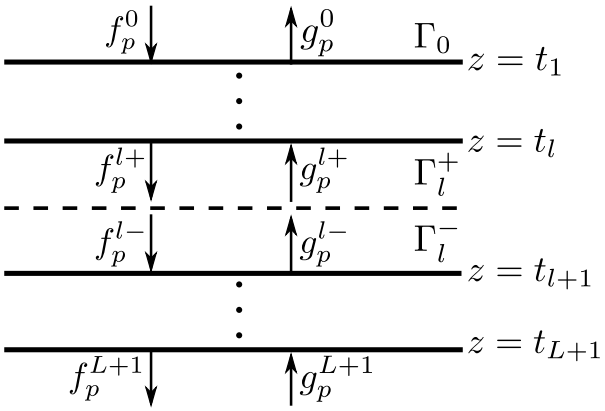

Fig. 4.3 Field expansions after treating fiber arrays as planar boundaries.

The computation of the scattering matrix linking two half spaces is illustrated as an example running the recursive scheme, the one for any two layers or slices following similar procedures.

As shown in Figure 4.3, a fiber array can be treated as a planar boundary, conditioned that PWE coefficients above and below it satisfy (4.11). Consequently, each layer has two slices and the laminate has $2L+2$ (including half spaces) ones in total. Assume $\mathscr{D}_{0,l+}^j$ compose the scattering matrix linking slices Γ_0 and Γ_l^+, *i.e.*,

$$\begin{bmatrix} \mathbf{f}^{l+} \\ \mathbf{g}^{0} \end{bmatrix} = \begin{bmatrix} \mathscr{D}_{0,l+}^1 & \mathscr{D}_{0,l+}^2 \\ \mathscr{D}_{0,l+}^3 & \mathscr{D}_{0,l+}^4 \end{bmatrix} \begin{bmatrix} \mathbf{f}^{0} \\ \mathbf{g}^{l+} \end{bmatrix}. \tag{4.12}$$

Together with (4.11), the expression of $\mathscr{D}^j_{0,l-}$ is derived as

$$\mathscr{D}^1_{0,l-} = \mathscr{D}^1_{l-,l+}\left(\mathbf{I} - \mathscr{D}^2_{0,l+}\mathscr{D}^3_{l-,l+}\right)^{-1}\mathscr{D}^1_{0,l+}, \tag{4.13a}$$

$$\mathscr{D}^2_{0,l-} = \mathscr{D}^2_{l-,l+} + \mathscr{D}^1_{l-,l+}\left(\mathbf{I} - \mathscr{D}^2_{0,l+}\mathscr{D}^3_{l-,l+}\right)^{-1}\mathscr{D}^2_{0,l+}\mathscr{D}^4_{l-,l+}, \tag{4.13b}$$

$$\mathscr{D}^3_{0,l-} = \mathscr{D}^3_{0,l+} + \mathscr{D}^4_{0,l+}\left(\mathbf{I} - \mathscr{D}^3_{l-,l+}\mathscr{D}^2_{0,l+}\right)^{-1}\mathscr{D}^3_{l-,l+}\mathscr{D}^1_{0,l+}, \tag{4.13c}$$

$$\mathscr{D}^4_{0,l-} = \mathscr{D}^4_{0,l+}\left(\mathbf{I} - \mathscr{D}^3_{l-,l+}\mathscr{D}^2_{0,l+}\right)^{-1}\mathscr{D}^4_{l-,l+}. \tag{4.13d}$$

Based on the obtained $\mathscr{D}^j_{0,l-}$, values of $\mathscr{D}^j_{0,(l+1)+}$ can be computed with (4.13) by replacing $\mathscr{D}^j_{0,l+}$, $\mathscr{D}^j_{l-,l+}$ as $\mathscr{D}^j_{0,l-}$ and $\mathscr{D}^j_{l-,(l+1)+}$, respectively. Running the above procedures recursively until $l = L+1$, the solution for $\mathscr{D}^j_{0,L+1}$ is obtained.

4.2.3 Retrieve expansion coefficients

The scattering matrix $\mathscr{D}^j_{0,L+1}$ links fields above and below the laminate and has the relation

$$\begin{bmatrix}\mathbf{f}^{L+1}\\ \mathbf{g}^0\end{bmatrix} = \begin{bmatrix}\mathscr{D}^1_{0,L+1} & \mathscr{D}^2_{0,L+1}\\ \mathscr{D}^3_{0,L+1} & \mathscr{D}^4_{0,L+1}\end{bmatrix}\begin{bmatrix}\mathbf{f}^0\\ \mathbf{g}^{L+1}\end{bmatrix}. \tag{4.14}$$

$\mathbf{f}^0$ stands for the amplitude of the incident wave, which is known, and $\mathbf{g}^{L+1}$ equal 0 because no field illuminates the laminate from the bottom. Thus we have $\mathbf{f}^{L+1} = \mathscr{D}^1_{0,L+1}\mathbf{f}^0$ and $\mathbf{g}^0 = \mathscr{D}^3_{0,L+1}\mathbf{f}^0$.

To reach the field solution in the whole space, expansion coefficients in each layer need to be retrieved. Based on $\mathbf{f}^0$, $\mathbf{g}^0$, coefficients could be computed with the aid of the scattering matrix $\mathscr{D}^j_{0,l\pm}$ by

$$\mathbf{g}^{l\pm} = (\mathscr{D}^4_{0,l\pm})^{-1}\left(\mathbf{g}^0 - \mathscr{D}^3_{0,l\pm}\mathbf{f}^0\right), \tag{4.15a}$$

$$\mathbf{f}^{l\pm} = \mathscr{D}^1_{0,l\pm}\mathbf{f}^0 + \mathscr{D}^2_{0,l\pm}(\mathscr{D}^4_{0,l\pm})^{-1}\left(\mathbf{g}^0 - \mathscr{D}^3_{0,l\pm}\mathbf{f}^0\right), \tag{4.15b}$$

or the transmitting matrix [45] $\mathscr{T}^j_{l\pm,0}$ which satisfies the equation

$$\begin{bmatrix}\mathbf{f}^{l\pm}\\ \mathbf{g}^{l\pm}\end{bmatrix} = \begin{bmatrix}\mathscr{T}^1_{l\pm,0} & \mathscr{T}^2_{l\pm,0}\\ \mathscr{T}^3_{l\pm,0} & \mathscr{T}^4_{l\pm,0}\end{bmatrix}\begin{bmatrix}\mathbf{f}^0\\ \mathbf{g}^0\end{bmatrix}, \tag{4.16}$$

so $\mathbf{f}^{l\pm} = \mathscr{T}^1_{0,l\pm}\mathbf{f}^0 + \mathscr{T}^2_{0,l\pm}\mathbf{g}^0$, $\mathbf{g}^{l\pm} = \mathscr{T}^3_{0,l\pm}\mathbf{f}^0 + \mathscr{T}^4_{0,l\pm}\mathbf{g}^0$. However, these two solutions suffer from ill-conditioned matrices and the resulting computational problems.

The retrieval method in [26] is applied here. Letting $\mathbf{g}^{L+1} = \mathbf{0}$ in

$$\begin{bmatrix} \mathbf{f}^{L+1} \\ \mathbf{g}^{l\pm} \end{bmatrix} = \begin{bmatrix} \mathscr{D}^1_{l\pm,L+1} & \mathscr{D}^2_{l\pm,L+1} \\ \mathscr{D}^3_{l\pm,L+1} & \mathscr{D}^4_{l\pm,L+1} \end{bmatrix} \begin{bmatrix} \mathbf{f}^{l\pm} \\ \mathbf{g}^{L+1} \end{bmatrix} \tag{4.17}$$

produces

$$\mathbf{g}^{l\pm} = \mathscr{D}^3_{l\pm,L+1} \mathbf{f}^{l\pm}. \tag{4.18}$$

Combining it with the equation from (4.12),

$$\mathbf{f}^{l\pm} = \mathscr{D}^1_{0,l\pm} \mathbf{f}^0 + \mathscr{D}^2_{0,l\pm} \mathbf{g}^{l\pm}, \tag{4.19}$$

$\mathbf{f}^{l\pm}$ and $\mathbf{g}^{l\pm}$ have the solutions

$$\mathbf{f}^{l\pm} = \left(\mathbf{I} - \mathscr{D}^2_{0,l\pm} \mathscr{D}^3_{l\pm,L+1}\right)^{-1} \mathscr{D}^1_{0,l\pm} \mathbf{f}^0, \tag{4.20a}$$

$$\mathbf{g}^{l\pm} = \mathscr{D}^3_{l\pm,L+1} \mathbf{f}^{l\pm}, \tag{4.20b}$$

which are stable in terms of calculation.

The substitution of $\mathbf{f}^{l\pm}$ and $\mathbf{g}^{l\pm}$ into (4.10) generates the solution of $b_m^{(l,0)}$ and $b_m^{(l,v)} = b_m^{(l,0)} e^{i\alpha_0 vd}$. With PWE and CWE coefficients, the full-field solution is obtained.

4.3 Computation of the Green's function

The equivalence theory requires the solution due to the source inside a fiber and the computation of the Green's function provides a way to reach it.

The Green's function, denoted by $G(\mathbf{r}, \mathbf{r}_s)$, is defined as the field solution at $\mathbf{r}$ when the line source at $\mathbf{r}_s$ emits field $H_0^{(1)}(k_j^l r_s)/(4i)$, j being s or f depending on the source location. The case $\mathbf{r}_s$ in the fiber is only considered here since damages on fibers are focused. Based on the knowledge $G(\mathbf{r} - vd\hat{x}, \mathbf{r}_s - vd\hat{x}) = G(\mathbf{r}, \mathbf{r}_s)$, the source can be assumed in the $(l, 0)$-th fiber. Since the inner source is a singularity of the structure, quasi-periodic theories could not be applied directly and ASM is applied.

As shown in Figure 4.4, a phased source-array is fabricated. All sources share same current except the one inside the (l, v)-th fiber is with phase $\exp(i\alpha_0 vd)$. From the identity

$$\frac{d}{2\pi} \int_{-\pi/d}^{\pi/d} e^{i\alpha_0 vd} \mathrm{d}\alpha_0 = \delta_{v,0}, \tag{4.21}$$

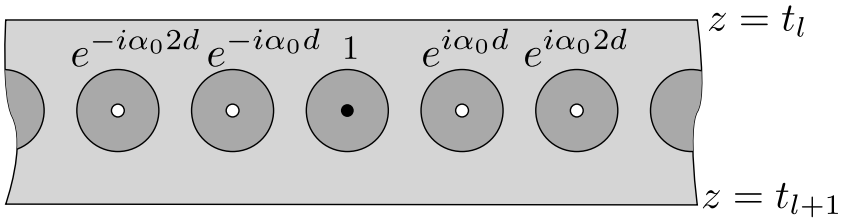

Fig. 4.4 Phase distribution in array scanning method, solid dot standing for the equivalent source and hollow ones for fictitious sources.

we can conclude that the impacts of fictitious sources can be canceled after an integration over the first Brillouin zone and the true field solution follows

$$G(\mathbf{r},\mathbf{r}_s) = \frac{d}{2\pi}\int_{-\pi/d}^{\pi/d} G(\mathbf{r},\mathbf{r}_s,\alpha_0,\infty)\mathrm{d}\alpha_0, \tag{4.22}$$

where $G(\mathbf{r},\mathbf{r}_s,\alpha_0,\infty)$ is the solution for the phased array. Numerical methods [38] are used to perform this integration, while the computation of the integrand is introduced next.

With the phased array, as expected, quasi-periodic theories become applicable. Due to the inner sources, $q_m^{(l,v)} = J_m(k_f^l\left|\mathbf{r}_s-\mathbf{o}_l^0\right|)e^{-im\arg\left(\mathbf{r}_s-\mathbf{o}_l^0\right)}/4i$, not zeros. Thus (4.7) is updated as

$$\mathbf{f}^{l-} = \mathbf{f}^{l+} + \Omega^{l-}\left[\mathbf{R}^l\left(\mathbf{J}^{l+}\mathbf{g}^{l-}+\mathbf{J}^{l-}\mathbf{f}^{l+}\right)+\mathbf{T}^l\mathbf{q}^{(l,0)}\right], \tag{4.23a}$$

$$\mathbf{g}^{l+} = \mathbf{g}^{l-} + \Omega^{l+}\left[\mathbf{R}^l\left(\mathbf{J}^{l+}\mathbf{g}^{l-}+\mathbf{J}^{l-}\mathbf{f}^{l+}\right)+\mathbf{T}^l\mathbf{q}^{(l,0)}\right]. \tag{4.23b}$$

Together with (4.18) and (4.19) (set $\mathbf{f}^0 = 0$, since no exterior source), the solution to $\mathbf{f}^{l\pm}$ and $\mathbf{g}^{l\pm}$ is obtained and defined as

$$\mathbf{g}^{l+} = \frac{\Theta_{l+}\mathscr{D}^3_{L+1,l-}\Psi_l^{-1}\Omega^{l-}+\Omega^{l+}}{\Xi_l-\Theta_{l+}\mathscr{D}^3_{L+1,l-}\Psi_l^{-1}\Theta_{l-}\mathscr{D}^2_{0,l+}}\mathbf{T}^l\mathbf{q}^l \tag{4.24a}$$

$$\mathbf{f}^{l-} = \frac{\Theta_{l-}\mathscr{D}^2_{0,l+}\Xi_l^{-1}\Omega^{l+}+\Omega^{l-}}{\Psi_l-\Theta_{l-}\mathscr{D}^2_{0,l+}\Xi_l^{-1}\Theta_{l+}\mathscr{D}^3_{L+1,l-}}\mathbf{T}^l\mathbf{q}^l \tag{4.24b}$$

$$\mathbf{f}^{l+} = D^2_{0,l+}\mathbf{g}^{l+} \tag{4.24c}$$

$$\mathbf{g}^{l-} = D^3_{l-,L+1}\mathbf{f}^{l-}, \tag{4.24d}$$

where $\Theta_{l\pm} = \mathbf{I}+\Omega^{l\pm}\mathbf{R}^l\mathbf{J}^{\pm}$, $\Xi_l = \mathbf{I}-\Omega^{l+}\mathbf{R}^l\mathbf{J}^{l-}\mathscr{D}^2_{0,l+}$, $\Psi_l = \mathbf{I}-\Omega^{l-}\mathbf{R}^l\mathbf{J}^{l+}\mathscr{D}^3_{L+1,l-}$.

To get the full-field solution, the laminate is divided into two parts, the layers below the l-th layer and the ones above it. The modeling of the former is similar with the one in section 4.3 by treating $\mathbf{f}^{l-}$ as coefficients for the incident wave, and the field solution

follows

$$\mathbf{f}^{l'\pm} = \left(\mathbf{I} - \mathscr{D}^2_{l-,l'\pm}\mathscr{D}^3_{l'\pm,L+1}\right)^{-1}\mathscr{D}^1_{l-,l'\pm}\mathbf{f}^{l-}, \tag{4.25a}$$

$$\mathbf{g}^{l'\pm} = \mathscr{D}^3_{l'\pm,L+1}\mathbf{f}^{l'\pm}, \tag{4.25b}$$

for $l' > l$. Layers above the l-th layer can be dealt with similarly and, for $l' < l$,

$$\mathbf{g}^{l'\pm} = \left(\mathbf{I} - \mathscr{D}^3_{l+,l'\pm}\mathscr{D}^2_{0,l'\pm}\right)^{-1}\mathscr{D}^4_{l+,l'\pm}\mathbf{g}^{l+}, \tag{4.26a}$$

$$\mathbf{f}^{l'\pm} = \mathscr{D}^2_{0,l'\pm}\mathbf{g}^{l'\pm}. \tag{4.26b}$$

Care should especially be on cases when $l' = 0$ and $l' = L+1$, where the solution is given by $\mathbf{f}^0 = \mathbf{0}$, $\mathbf{g}^0 = \mathscr{D}^4_{0,l+}\mathbf{g}^{l+}$ and $\mathbf{g}^{L+1} = \mathbf{0}$, $\mathbf{f}^{L+1} = \mathscr{D}^1_{l-,L+1}\mathbf{f}^{l-}$, respectively.

Associated CWE coefficients $b^{(l,0)}_{m,n}(\alpha_0,\infty)$ and $a^{(l,0)}_{m,n}(\alpha_0,\infty)$ are obtained with the substitution of $\mathbf{f}^{l\pm}$ and $\mathbf{g}^{l\pm}$ into (4.10) and (4.8). Then the full-field solution of $G(\mathbf{r},\mathbf{r}_s,\alpha_0,\infty)$ follows the computation of related PWEs or CWEs.

4.4 Defects modeled as equivalent sources

Following the equivalence theory in section 3.4, the field disturbance due to defects is equivalent to putting sources inside the initially well-organized fibers. According to the scattering linearity, the field solution is a summation of responses due to the incident wave and equivalent sources,

$$V(\mathbf{r}) = V^{inc}(\mathbf{r}) + \sum_{(l,v)\in\mathbb{D}} V^{(l,v)}(\mathbf{r}), \tag{4.27}$$

where V^{inc} and $V^{(l,v)}$ correspond to the exterior and equivalent source inside the (l,v)-th fiber, respectively. The CWE of source leads to the decomposition of $V^{(l,v)}(\mathbf{r})$ and the rewritten form of (4.27) as

$$V(\mathbf{r}) = V^{inc}(\mathbf{r}) + \sum_{(l,v)\in\mathbb{D}}\sum_{n\in\mathbb{Z}} q^{(l,v)}_n G_n(\mathbf{r},\mathbf{o}^v_l). \tag{4.28}$$

where $G_n(\mathbf{r},\mathbf{o}^v_l)$ as the field response due to the cylindrical wave $g^{H^{(1)}}_n(k^l_f,\mathbf{r}^v_l)$. The solution of $q^{(l,v)}_m$ is found from the combination of two linear relations between $a^{(l,v)}_m$ and $q^{(l,v)}_m$.

Let us assume that $a^{(l,v)}_m$, $a^{(l,v)}_{m,inc}$, $a^{(l,v)}_{m,n}$ are CWE coefficients corresponding to V, V^{inc}, and G_n, respectively. Setting $\mathbf{q}^{\mathbb{D}} = [q^{(l,v)}_m]$, $\mathbf{a}^{\mathbb{D}} = [a^{(l,v)}_m]$, $\mathbf{a}^{\mathbb{D}}_{inc} = [a^{(l,v)}_{m,inc}]$, and $\Lambda^{\mathbb{D}} = [a^{(l,v)}_{m,n}]$, $(l,v)\in\mathbb{D}$, we have

$$\mathbf{a}^{\mathbb{D}} = \mathbf{a}^{\mathbb{D}}_{inc} + \Lambda^{\mathbb{D}}\mathbf{a}^{\mathbb{D}}, \tag{4.29}$$

from the scattering linearity and

$$\mathbf{q}^{\mathbb{D}} = \Pi^{\mathbb{D}} \mathbf{a}^{\mathbb{D}}, \tag{4.30}$$

from the reformulation of fiber boundary conditions and the application of Graf's addition theorem. $\Pi^{\mathbb{D}} = \text{diag}\left\{\Pi^{(l,v)}\right\}$ and $\Pi^{(l,v)}$ is defined as $\text{diag}\left\{-R_m^l / T_m^l\right\}$, $\text{diag}\left\{\left(\tilde{R}_m^{(l,v)} - R_m^l\right) / T_m^l\right\}$, $(\mathbf{T}^l)^{-1}\left(\mathbf{g}_1^{(l,v)} \mathbf{R}^l \mathbf{g}_2^{(l,v)} - \mathbf{R}^l\right)$, and $\left[\mathbf{I} - \Phi^{(l,v)} \mathbf{R}^{l,\prime}\right]^{-1} \Phi^{(l,v)} \mathbf{T}^{l,\prime}$ for the missing, shrunk/expanded, displaced fiber and circular inclusion, respectively, where $\mathbf{I}$ is the identity matrix, $\mathbf{R}^l = \text{diag}\left\{R_m^l\right\}$, $\mathbf{T}^l = \text{diag}\left\{T_m^l\right\}$, $\mathbf{R}^{l,\prime} = \text{diag}\left\{R_m^{l,\prime}\right\}$, $\mathbf{T}^{l,\prime} = \text{diag}\left\{T_m^{l,\prime}\right\}$, $\mathbf{g}_1^{(l,v)} = [g_{n-m}^J(k_s, \mathbf{o}_l^v - \tilde{\mathbf{o}}_l^v]$, $\mathbf{g}_2^{(l,v)} = [g_{n-m}^J(k_s, \tilde{\mathbf{o}}_l^v - \mathbf{o}_l^v)]$, $\Phi^{(l,v)} = [\Phi_{m,n}^{(l,v)}]$, and

$$\Phi_{m,n}^{(l,v)} = \sum_{u \in \mathbb{Z}} \bar{R}_u^{(l,v)} g_{u-m}^J(k_f^l, \mathbf{o}_l^v - \bar{\mathbf{o}}_l^v) g_{n-u}^J(k_f^l, \bar{\mathbf{o}}_l^v - \mathbf{o}_l^v). \tag{4.31}$$

Then the solution for $\mathbf{q}^{\mathbb{D}}$ is given by

$$\mathbf{q}^{\mathbb{D}} = \left(\mathbf{I} - \Pi^{\mathbb{D}} \Lambda^{\mathbb{D}}\right)^{-1} \Pi^{\mathbb{D}} \mathbf{a}_{inc}^{\mathbb{D}}. \tag{4.32}$$

Involved quantities V^{inc}, $\mathbf{a}_{inc}^{\mathbb{D}}$ are computed by methods for the exterior illumination while the computation of G_n, $\Lambda^{\mathbb{D}}$ is similar with the one for the Green's function.

4.5 Truncation numbers

Table 4.1 Procedure to decide P and M for multilayer structures.

1.	Initialize the set of layer indexes $\mathbb{J} = [1, 2, \ldots, L]$, $M_l = M_l^{\max}$, $l \in \mathbb{J}$, $P = 0$, $\tau = 10^{-4}$, and the sampling points (x_l', z_l'), $x_l' = x_l^0$, $z_l' = (z_l^0 + t_l)/2$.
2.	Compute field values at (x_l', z_l'), $l \in \mathbb{J}$, from CWEs and PWEs, results denoted by V_p^l and V_c^l, respectively.
3.	If $\max\{\left\|V_p^l - V_c^l\right\|, l \in \mathbb{J}\} < \tau$, go to step 4; otherwise, update $P = P + 1$ and go to step 2.
4.	Update $M_l = M_l - 1$ for $l \in \mathbb{J}$ and compute corresponding V_p^l and V_c^l.
5.	$\mathbb{J} = \mathbb{J} \setminus \{l\}$ for ls satisfying $\left\|V_p^l - V_c^l\right\| < \tau$. If $\mathbb{J}$ is empty, stop; otherwise, repeat step 4.

PWEs and CWEs are infinite series and approximated by the truncations $\sum_{p=-P}^{P}$ and $\sum_{p=-M}^{M}$ in the computation. In subsection 2.7.1, P and M with single-layer structures are estimated by a numerical strategy benefiting from the knowledge that values of fields in the slab are the same, no matter that they are computed from PWEs or CWEs. For multilayer structures, since the geometry and composing material might differ, the optimal P and

M can be changed accordingly from one layer to another. The procedures to find the optimal truncation number of CWE (denoted by M_l for the l-th layer) and PWE (denoted by P for all layers) are sketched in Table 4.1, where the maximum value of M_l is given by formula $M_l^{\max} = \mathrm{Int}\left(\Re\left(4.05 \times \left(k_s^l c_l\right)^{1/3} + k_s^l c_l\right)\right) + 7$ [14], 7 as safety number. PWE truncation numbers for different layers are forced to be the same to facilitate the mode matching at slab boundaries.

4.6 Numerical results

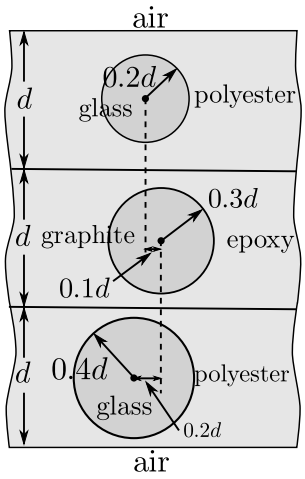

Fig. 4.5 Structure of the concerned 3-layer laminate, fiber period $d = 0.1$mm.

Simulations are firstly run with a 3-layer laminate, the undamaged structure of which is sketched in Fig. 4.5, where the fiber period $d = 0.1$mm, graphite is with relative permittivity $\Re(\epsilon_{rf}) = 12$ and conductivity $\sigma_f = 330$ S/m, glass with $\epsilon_{rf} = 6$, epoxy with $\epsilon_{rs} = 3.6 + i0.072$, and polyester with $\epsilon_{rs} = 2.8 + i0.056$. The relative permeability of all components equals 1.

About the truncation of PWEs and CWEs, applying the proposed numerical approach, with a plane-wave illumination upon the above mentioned laminate, wavelength $\lambda^{inc} = d$ and TM polarization, generated results are $P = 5$, $M_1 = 10$, $M_2 = 11$, $M_3 = 13$.

The solution to the Green's function is validated through comparisons with COMSOL, which as already said runs with a finite element method. Setting the line source at $\mathbf{o}_1^0$ and sampling field values along the line $-5d \le x \le 5d$, $z = d$, results are shown in Figure 4.6. Good fits are observed in both TM and TE cases, while the discrepancies might be due to the truncation of the laminate, 33 fibers in each layer, in the modeling of COMSOL. Reciprocity theorem is tested as well to check the modeling accuracy. Exchanging the position of source

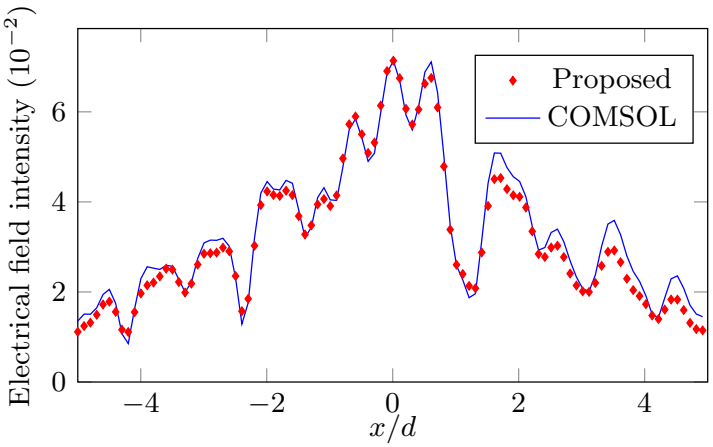

(a) TM

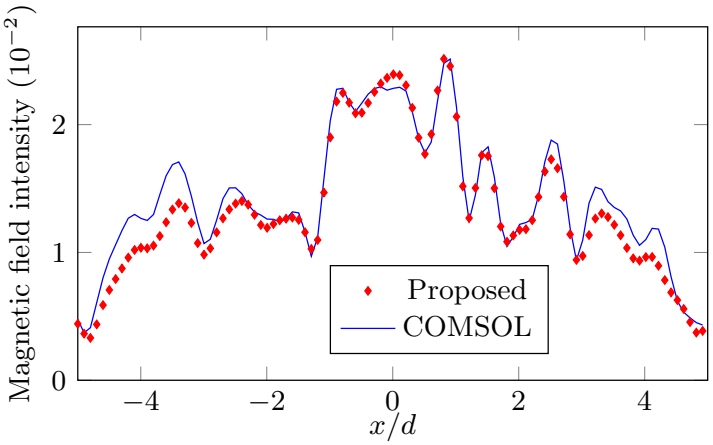

(b) TE

Fig. 4.6 Validation of the computation of the Green's function through comparisons with COMSOL, line source at $\mathbf{r}_s = (0,-d)$, $\lambda^{inc} = d$, fields sampled along $z = d$, $-5d \le x \le 5d$.

and observation points. The defined relative error $\tau = |G(\mathbf{r},\mathbf{r}_s) - G(\mathbf{r}_s,\mathbf{r})| \,/\, |G(\mathbf{r},\mathbf{r}_s)|$, is less than 1.5×10^{-8}.

Now, assume all kinds of mentioned defects happen in this laminate. Specifically, the $(1,-3)$-th and $(3,3)$-th fibers are missing, $\tilde{\mathbf{o}}_2^{-1} - \mathbf{o}_2^{-1} = (0.1d, 0.1d)$ for the displaced fiber, $\tilde{c}_2^0 = 0.7c_2$ for the shrunk fiber and $\tilde{\mathbf{o}}_1^2 - \mathbf{o}_1^2 = (0.1c_1, 0.1c_1)$, $\tilde{c}_1^2 = 0.7c_1$ for the circular inclusion. A line source at $\mathbf{r}_s = (0,d)$ illuminates this damaged laminate with wave $H_0^{(1)}(k_s^0 r_s)/(4i)$, $r_s = |\mathbf{r} - \mathbf{r}_s|$, wavelength $\lambda^{inc} = d$. In TM and TE polarizations, intensities of the total fields are shown in Figure 4.7, where the amplitude is cut at 0.3 for the easier appraisal. In TM case, most of the energy is reflected into the upper half space and little can penetrate into the laminate, while much more energy can propagate inside in the TE case.

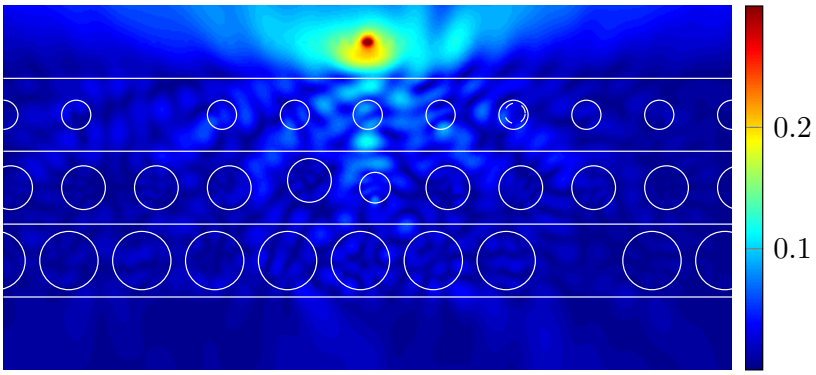

(a) TM

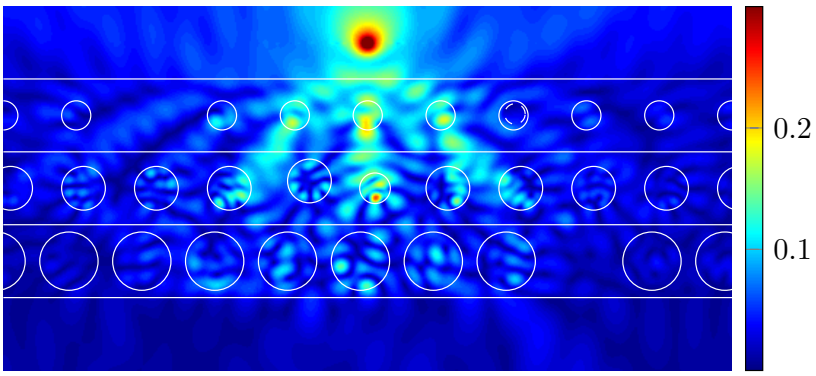

(b) TE

Fig. 4.7 Intensity of (a) electric field and (b) magnetic field with line source position $\mathbf{r}_s = (0, d)$, $\lambda^{inc} = d$, white lines indicating the laminate structure.

What is more, due to the difference of permittivity, strong resonances are observed and peaks appear inside the fiber for TE, which can be derived from boundary conditions. Such phenomenas do not happen in the TM case since the permeabilities are the same inside the laminate. Sampling 500 values along the line connecting centers of the $(2, -5)$-th and $(2, 5)$-th fibers, *i.e.*, $z = -d$, $-5d \leq x \leq 5d$, comparisons with results from COMSOL are shown in Figure 4.8. Good agreements are observed despite strong fluctuations due to the size of component, *i.e.*, slab thickness and fiber radius, are in the scale of wavelength.

When the wavelength is much larger than the component size, the field inside the fiber is slightly impacted by defects and the Born approximation can be used as described in Appendix B. Set $\lambda^{inc} = 100d$ and assume only missing fibers exist, no other types of defects. With TM polarization, comparisons of field disturbances are shown in Figure 4.9. The peak value appears at the position corresponding to the $(3, 3)$-th missing fiber due to its larger radius than the one of the other missing fiber.

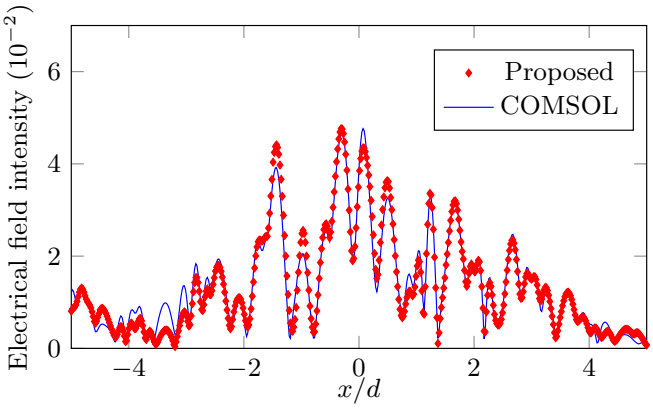

(a) TM

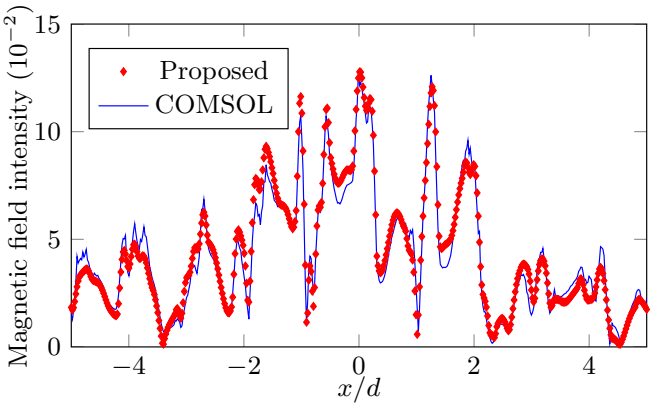

(b) TE

Fig. 4.8 Validation of the proposed approach on modeling the damaged laminate through comparisons with COMSOL, line source at $\mathbf{r}_s = (0, d)$, $\lambda^{inc} = d$, fields sampled along $z = -d$, $-5d \leq x \leq 5d$.

As mentioned in subsection 3.4.2, with related quantities stored, the modeling efficiency is high. Running on a laptop (dual cores, clock speeds 2.9 GHz, memory 16 GB), each line graph in Figure 4.6 and Figure 4.8 costs less than 50 milliseconds, while more than 6 seconds are needed for COMSOL.

Field disturbances with different layer numbers are investigated upon a laminate sharing same structure with the above one, except with $\epsilon_f^l = 6$, $c_l = d/4$, $\epsilon_s^l = 3.6 + 0.072$, $x_l^0 = 0$ for $l = 1, 2, \ldots, L$. With two missing fibers, indexed by $(L, -2)$ and $(L, 2)$, results are shown in Figure 4.10. Two cases are considered, $L = 3$ and $L = 8$. As seen, missing fibers behave like sources and the peak value in Figure 4.10(a) is larger than that in Figure 4.10(b). That is because, due to the reflection and losses in propagation, less energy would arrive at the damaged region for larger L. What is more, the energy spread wider for more layers and,

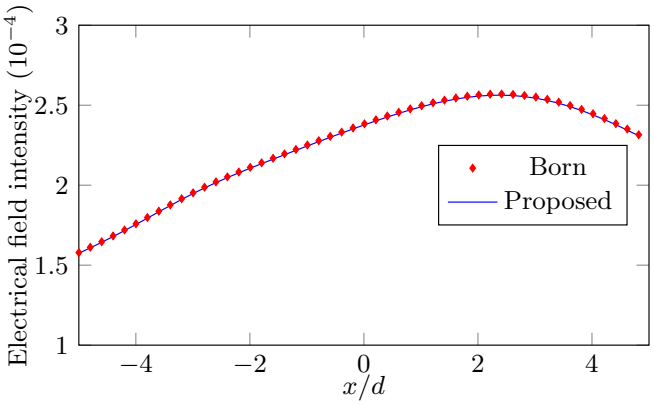

Fig. 4.9 Comparison of scattered field with results from the Born approximation, $(1,-3)$-th and $(3,3)$-th fibers missing, line source at $(0,d)$, $\lambda^{inc}=100d$, TM, fields sampled along $z=1.5d$, $-5d\leq x\leq 5d$.

in the modeling of COMSOL, the module size should be large to guarantee the accuracy. Maps of field disturbances can provide a guide to the imaging system. Usually, receivers are put in the upper half space to collect the data. However, small amplitudes are expected for the laminate having many layers and the data certainly are easily corrupted. Thus an imaging approach stable to noise is in need. Also, the energy distribution suggests that the central area is better to position receivers, as is in effect expected due to defect locations.

Generally, sources and receivers can only be put above the laminate in the testing system to collect the information. However, for the defects inside deep layers, the impacts of defects might be decayed significantly due to losses and, therefore, are not easy to be identified. Investigations are made on a 4-layer laminate by moving the missing fibers from layer to layer. Each layer of the laminate enjoys the same structure and composed materials. With graphite fibers and epoxy slabs, maps of anomalous field are drawn in Fig. 4.11, where the color ranges are the same and set as $(0,0.02)$ for a better appraisal. Due to lossy fibers, as the missing fibers move deeper, the amplitude of the anomalous field reaching the upper half space reduces a lot. When the missing fibers appear at the bottom layer, almost no hints of defects can be observed above the laminate. However, changing the fiber material to be the lossless glass, as shown in Fig. 4.12, the field decays much slower in the propagation than that with graphite fibers and, as a result, the impacts of defects can be observed above the laminate even the missing fibers locate at the bottom layer.

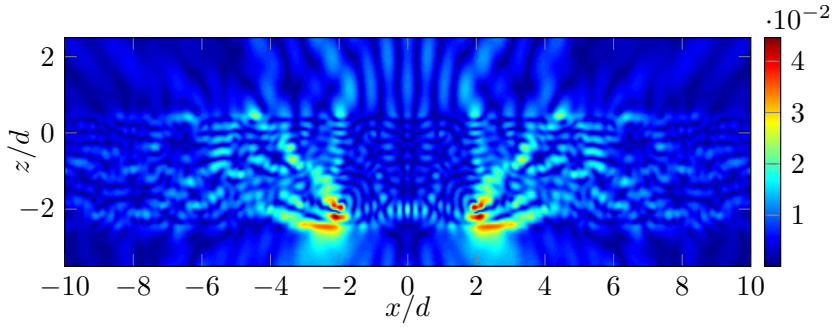

(a) 3-layer laminate

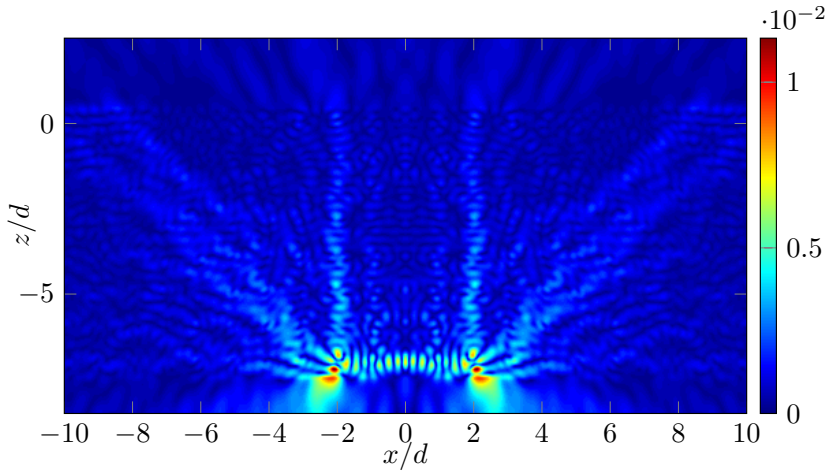

(b) 8-layer laminate

Fig. 4.10 Maps of anomalous field with the $(L,-2)$-th and $(L,2)$-th fibers missing, $L=3$ or 8, line source at $(0,d)$, $\lambda^{inc}=d$, TM, glass fiber and epoxy matrix.

4.7 Summary

Electromagnetic modeling of damaged multilayer fibered laminates is concerned in this chapter and the involved computation of the Green's function is introduced as well. The validation of the presented approach is made in a broad band by comparing results with those from a finite-element commercial software and the Born approximation.

The combination of array scanning method and scattering matrices yields the solution to the Green's function, which is an integration of responses due to different fabricated phased array. Scattering matrices, used to analyze the wave propagation through the laminate, are computed in a recursive fashion. Together with prior knowledge (incident wave and no illumination from the bottom), the expansion coefficients of fields in the whole region are stably retrieved.

The electromagnetic behaviors of circular defects are equivalent to putting sources inside the corresponding sound fibers, thus the field solution is a summation of responses due to the illuminating source and equivalent ones.

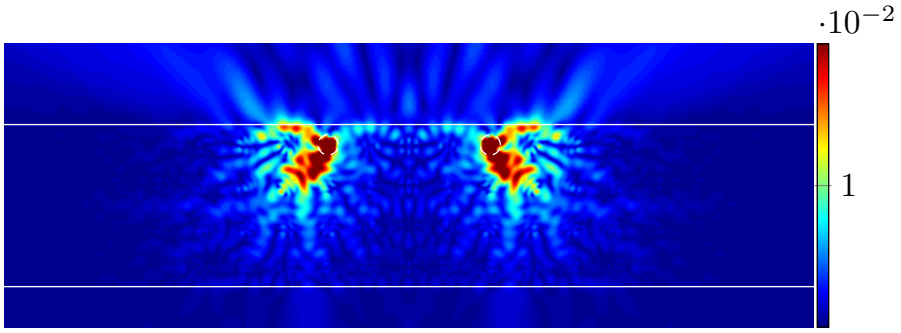

(a) $(1,-2)$-th and $(1,2)$-th fibers missing

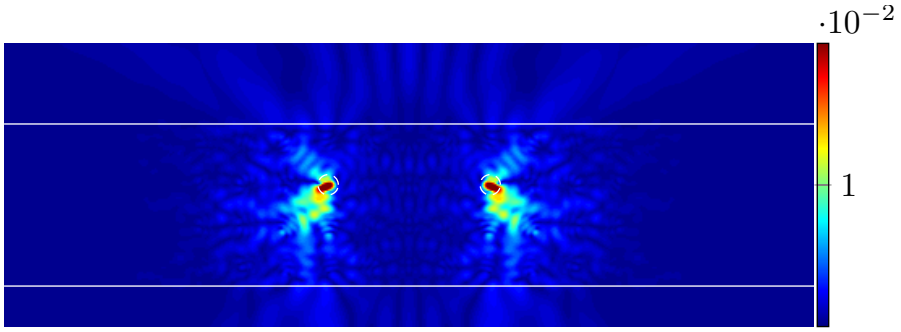

(b) $(2,-2)$-th and $(2,2)$-th fibers missing

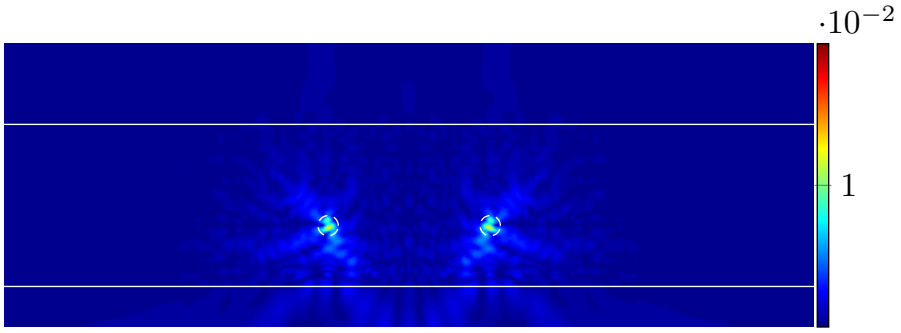

(c) $(3,-2)$-th and $(3,2)$-th fibers missing

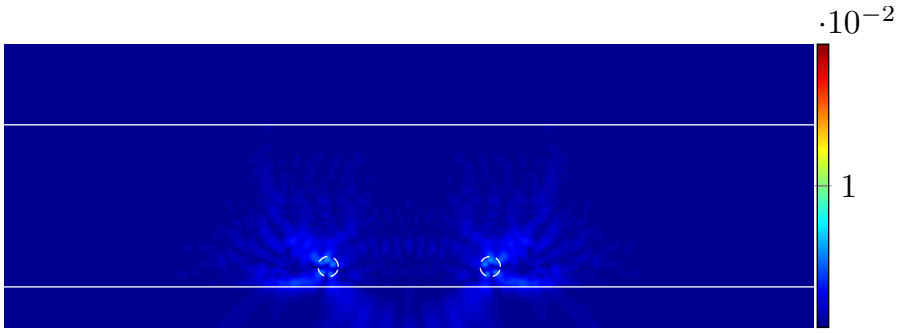

(d) $(4,-2)$-th and $(4,2)$-th fibers missing

Fig. 4.11 Maps of anomalous field with the $(l,-2)$-th and $(l,2)$-th fibers missing, $l = 1,2,3,4$, line source at $(0,d)$, $\lambda^{inc} = d$, TM, graphite fiber.

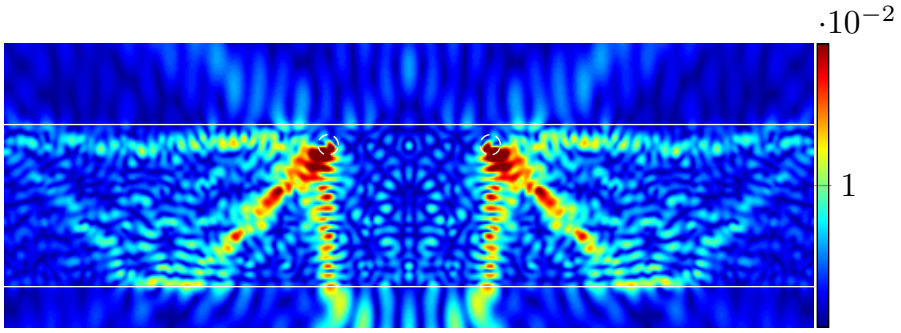

(a) $(1,-2)$-th and $(1,2)$-th fibers missing

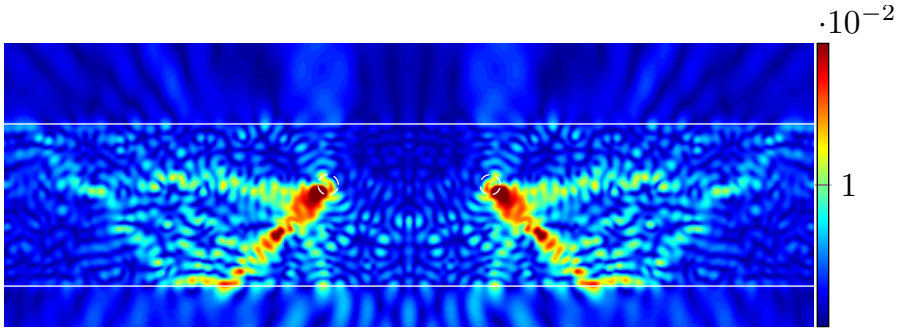

(b) $(2,-2)$-th and $(2,2)$-th fibers missing

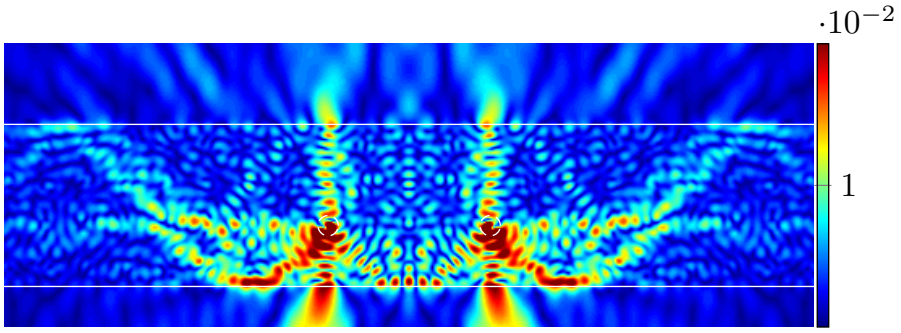

(c) $(3,-2)$-th and $(3,2)$-th fibers missing

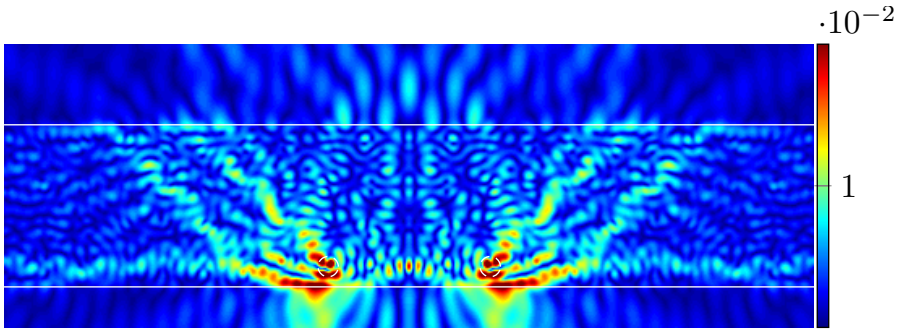

(d) $(4,-2)$-th and $(4,2)$-th fibers missing

Fig. 4.12 Maps of anomalous field with the $(l,-2)$-th and $(l,2)$-th fibers missing, $l = 1,2,3,4$, line source at $(0,d)$, $\lambda^{inc} = d$, TM, glass fiber.

Chapter 5

Locating damaged fibers with emphasis on exploration of joint sparsity

Defects are treated as sources inside the corresponding sound fibers in the direct modeling. Such treatment gives the possibility to locate missing, displaced, shrunk, expanded fibers and inclusions simultaneously, since all of them can be located via searching for equivalent sources. The equivalence theory also provides a link between the collected data and the expansion coefficients of equivalent sources, the nonzero elements of which indicate the index of damaged fibers. With data from sources and receivers in use, the solution from least square [27], MUltiple SIgnal Classification (MUSIC) [28], basic matching pursuit (BMP) [29] and an iterative, sparsity-constrained method [31] is developed herein.

Emphasis is put on the exploration of the joint sparsity [30] of the desired solution in cases with multiple sources. By properly measuring the joint sparsity with a mixture of l_2-norm and l_p-norm ($0 < p \leq 1$) and constraining the data discrepancy, the solution is obtained by solving an optimization problem with the application of the factorized gradient method [46]. The involved regularization parameter, which balances the data discrepancy and the sparsity level, is determined by the continuous L-curve method [46]. Various numerical simulations illustrate the effectiveness of this approach and its advantages vs other ones. Works presented in this chapter have been partly published in [32].

5.1 From direct modeling to imaging

Modeling the concerned defects as equivalent sources, the field solution is the summation

$$V(\mathbf{r}) = V^{inc}(\mathbf{r}) + \sum_{(l,v)\in\mathbb{D}} V^{(l,v)}(\mathbf{r}), \tag{5.1}$$

where V^{inc} and $V^{(l,v)}$ are field responses due to the exterior and equivalent source inside the (l,v)-th fiber, respectively, and $\mathbb{D}$ is the index set of damaged fibers. The decomposition of sources into cylindrical waves leads to the rewritten form

$$V(\mathbf{r}) = V^{inc}(\mathbf{r}) + \sum_{(l,v)\in\mathbb{D}} \sum_{m\in\mathbb{Z}} q_m^{(l,v)} G_m(\mathbf{r}, \mathbf{o}_l^v). \tag{5.2}$$

where $q_m^{(l,v)}$ are CWE coefficients of field scattered by the equivalent source. G_m behaves like the Green's function and is the solution for the expansion basis $g_m^{H^{(1)}}(k_f^l, \mathbf{r}_l^v)$.

However, in practice, the location (indexes) of damaged fibers is unknown and $\mathbb{D}$ is not available. Considering the fact that any fiber in the laminate might be damaged, the general form of (5.2) is

$$V(\mathbf{r}) = V^{inc}(\mathbf{r}) + \sum_{(l,v)\in\mathbb{F}} \sum_{m\in\mathbb{Z}} q_m^{(l,v)} G_m(\mathbf{r}, \mathbf{o}_l^v). \tag{5.3}$$

where $\mathbb{F}$ is the set of index (l,v) for all fibers, *i.e.*, $l = 1,2,\ldots,L$ and $v \in \mathbb{Z}$. $q_m^{(l,v)}$ are non-zero for damaged fibers and zero for the sound ones.

Mention that although an infinite set of fibers should be in detection in theory, since effects of the damaged region far from the concerned area can be neglected, only fibers near sources and receivers are focused onto in practice. Setting N_f as the number of focused-on fibers, with the knowledge about V^{inc} and G_m, the goal becomes to retrieve q_m^f, $f = 1,2,\ldots,N_f$, from the data of V. Then the indexes of damaged fibers are estimated from the position of non-zero entries.

Multiple sources and receivers are often used to acquire more information about the defects and to achieve better imaging performances. Assume sources subsequently work and, for each source, data are collected at all positions of receivers, *i.e.*, for each source, a data vector containing N_r is built, N_r number of receivers. Take data vectors as columns. The MSR (Multi-Static Response) [47] matrix dimensioned as $N_r \times N_s$, N_s number of sources in use, is composed as

$$\mathbf{V} = \begin{bmatrix} V_1^1 & V_1^2 & V_1^3 & \cdots & V_1^{N_s} \\ V_2^1 & V_2^2 & V_2^3 & \cdots & V_2^{N_s} \\ \vdots & \vdots & \vdots & \ddots & \vdots \\ V_{N_r}^1 & V_{N_r}^2 & V_{N_r}^3 & \cdots & V_{N_r}^{N_s} \end{bmatrix} \tag{5.4}$$

where V_i^s is the data collected by the i-th receiver when the j-th source is working, $i = 1,2,\ldots,N_r$, $s = 1,2,\ldots,N_s$. Compose the matrix $\mathbf{V}^{inc}$ from V^{inc} similarly and define $\mathbf{Y} = \mathbf{V} - \mathbf{V}^{inc}$, $\mathbf{G} = [G_m(\mathbf{r}_i, \mathbf{o}_l^v)]$, $\mathbf{r}_i$ the position of the i-th receiver, and $\mathbf{q} = [\mathbf{q}_{m,1}, \mathbf{q}_{m,2}, \ldots, \mathbf{q}_{m,N_s}]$,

$\mathbf{q}_{m,s} = [q_m^f]$, q_m^f coefficients associated with the s-th source. Then the equation in matrix form linking the collected data and the location of damaged fibers is simply written as

$$\mathbf{Y} = \mathbf{G}\mathbf{q}, \tag{5.5}$$

without noise corruption. The form considering the additive noise is

$$\mathbf{Y} = \mathbf{G}\mathbf{q} + \mathbf{N}_a, \tag{5.6}$$

where $\mathbf{N}_a = [N_{i,a}^s]$ and $N_{i,a}^s$ is the noise related with the i-th receiver and s-th source. The noise might comes from the uncertainty of the material parameters or the geometric positions of the structure being modeled. However, only the Gaussian random noise in measurements is considered herein.

5.2 Zero-order approximation

In the direct modeling, CWEs are truncated as $\sum_{m=-M}^{M}$ and the truncation number M has to be properly selected so that a tradeoff between the modeling accuracy and condition number of the to-be-inverted matrix (thus stability of the solution) is well made. Section 2 illustrates that the maximum value of M is given by the available formula $\text{int}\left(\left(k\sqrt{\epsilon_r}c\right)^{1/3} + k\sqrt{\epsilon_r}c\right)+7$, thus tends to zero at low frequencies [17] without considering the safety number 7.

With respect to this knowledge, an approximation (or a simplification), which is commonly used in fault detection [18, 48, 49], is applied by just letting M equals zero. Setting $M = 0$ and denoting corresponding matrices notations with the superscript 0, (5.5) can be reformulated as

$$\mathbf{Y} = \mathbf{G}^0\mathbf{q}^0 + \mathbf{N}^0, \tag{5.7}$$

where $\mathbf{N}^0$ is the resulting approximation error. Benefiting from this simplification, the dimensions of the matrices involved are largely reduced, which lightens the burden of the following reconstruction procedures. The fiber profile, indicating the defectuous status of fibers, can be observed from the line curve of $\mathbf{q}^0$, where peaks are expected to appear at elements corresponding to the damaged fibers.

To further simplify the notations, set $\mathbf{Z} = \mathbf{G}^0$, $\mathbf{S} = \mathbf{q}^0$ and $\mathbf{N} = \mathbf{N}^0 + \mathbf{N}_a$, then the data equation in the noisy case is updated as

$$\mathbf{Y} = \mathbf{Z}\mathbf{S} + \mathbf{N}. \tag{5.8}$$

5.3 Reconstruction algorithms

In this section, algorithms retrieving the information about indexes of damaged fibers from the MSR matrix are concerned. In addition to least square and MUSIC solutions, basic matching pursuit (BMP) is introduced as an example of subset selection methods. The sparsity structure of the desired $\mathbf{S}$ is also explored and details are given on related theories.

5.3.1 Least square

In cases where effects from additive noise and approximation errors can be neglected, the accurate $\mathbf{S}$ should satisfy the data equation $\mathbf{Y} = \mathbf{ZS}$ with small errors. Thus $\mathbf{S}$ is the solution to the minimization problem

$$\hat{\mathbf{S}} = \min ||\mathbf{Y} - \mathbf{ZS}||_F^2, \tag{5.9}$$

which is

$$\hat{\mathbf{S}} = \mathbf{Z}^H \left(\mathbf{ZZ}^H\right)^{-1} \mathbf{Y}. \tag{5.10}$$

The superscript H denotes the conjugate transpose operator. Letting $\mathbf{Z}^\dagger = \mathbf{Z}^H \left(\mathbf{ZZ}^H\right)^{-1}$, the s-th column of $\hat{\mathbf{S}}$, denoted by $\mathbf{S}_s$, satisfies $\mathbf{S}_s = \mathbf{Z}^\dagger \mathbf{Y}_s$, *i.e.*, the minimum l_2-norm solution to the equation $\mathbf{Y}_s = \mathbf{ZS}_s$. Thus, data vectors are independently dealt with and their couplings (between each other) are not considered.

5.3.2 MUSIC

The singular value decomposition (SVD) of $\mathbf{Y}$ reads as $\mathbf{Y} = \mathbf{U}\Lambda\mathbf{V}^H$, where $\mathbf{U}$ and $\mathbf{V}$ consist of left and right eigenvectors, respectively. $\Lambda = \text{diag}\left\{\sigma_j\right\}$ and σ_j is the j-th singular value, $j = 1, \ldots, \min\{N_r, N_s\}$. Eigenvectors (both left and right ones) corresponding to the K largest singular values compose the signal space $\mathbf{U}^s$ and $\mathbf{V}^s$, while all the rest construct the noise spaces $\mathbf{U}^n$ and $\mathbf{V}^n$.

However, K is unknown in practice and needs to be determined. It is shown that the plot of σ_j has a particular "L" shape and the optimal K corresponds to a point at the corner of the L-shape region, which is found by the discrete L-curve method in [50] here.

The estimation function of interest comes from the orthogonality of $\mathbf{U}^n$ with respect to the basis vector $\mathbf{Z}_f$, $f \in \mathbb{D}$. The correlation between $\mathbf{Z}_f$ and $\mathbf{U}^n$ can be measured by $\mathbf{Z}_f^H \mathbf{U}^n (\mathbf{U}^n)^H \mathbf{Z}_f$, thus the fiber profile can be obtained from the vector $\hat{\mathbf{s}}$ with its elements computed by the estimator

$$\hat{s}_f = \frac{1}{\mathbf{Z}_f^H \mathbf{U}^n (\mathbf{U}^n)^H \mathbf{Z}_f}, \tag{5.11}$$

Table 5.1 Retrieve **S** with M-BMP method.

1.	Initialization: residual $\mathbf{Y}_0^{\perp} = \mathbf{Y}$, empty index set $\mathbb{I}_0$, $k = 1$;
2.	Selection: $f_k = \arg\max_f ||\mathbf{Z}_f^H \mathbf{Y}_{k-1}^{\perp}||^2$;
3.	Update: $k = k+1$, $\mathbb{I}_k = \mathbb{I}_{k-1} \cup f_k$, $\mathbf{Y}_k^{\perp} = \left(\mathbf{I} - \mathbf{Z}_{f_k} \mathbf{Z}_{f_k}^H\right) \mathbf{Y}_{k-1}^{\perp}$;
4.	If the stopping criterion is satisfied, stop; otherwise, repeat step 2 and 3;
5.	Least square solution: $\hat{\mathbf{S}} = (\mathbf{Z}_{\mathbb{I}_k}^H \mathbf{Z}_{\mathbb{I}_k})^{-1} \mathbf{Z}_{\mathbb{I}_k}^H \mathbf{Y}$.

and peaks would be observed on the curve of $\hat{\mathbf{s}}$. In the case of non-normalized $\mathbf{Z}_f$, the following formula is used instead in this chapter,

$$\hat{s}_f = \frac{\mathbf{Z}_f \mathbf{Z}_f^H}{\mathbf{Z}_f^H \mathbf{U}^n (\mathbf{U}^n)^H \mathbf{Z}_f}. \tag{5.12}$$

5.3.3 M-BMP

The named M-BMP method is an extension of basic matching pursuit (BMP) and the first letter “M" stands for multiple sources [31]. The goal is to select a small set of columns of **Z** to represent **Y**. In this algorithm, first, the column best aligned with **Y** is selected, denoted as $\mathbf{Z}_{f_1}$. Then, one projects **Y** along the direction $\mathbf{Z}_{f_1}$ and the deduction of this projection from **Y** yields the residual $\mathbf{Y}_1^{\perp}$. This algorithm runs by consequently choosing the column.

Assume all columns of **Z** have been normalized. Concerning the k-th iteration, define the residual $R_{f,f_k} = \left(\mathbf{I} - \mathbf{Z}_f \mathbf{Z}_f^H\right) \mathbf{Y}_{k-1}^{\perp}$, then the column $\mathbf{Z}_f$, $f = 1, 2, \ldots, N_f$, reaching the minimum of R_{f,f_k} is selected. With the equation

$$||R_{f,f_k}||_F^2 = \mathrm{Tr}\left(R_{f,f_k}^H R_{f,f_k}\right) = ||\mathbf{Y}_{k-1}^{\perp}||_F^2 - \mathrm{Tr}\left((\mathbf{Y}_{k-1}^{\perp})^H \mathbf{Z}_f \mathbf{Z}_f^H \mathbf{Y}_{k-1}^{\perp}\right), \tag{5.13}$$

the minimization problem can turn to maximize the second term of (5.13), *i.e.*,

$$f_k = \arg\max_f ||\mathbf{Z}_f^H \mathbf{Y}_{k-1}^{\perp}||^2, \; f = 1, 2, \ldots, N_f. \tag{5.14}$$

Denote $\mathbb{I}_{k-1}$ as the index set of selected columns in the $(k-1)$-th iteration. If $f_k \notin \mathbb{I}_{k-1}$, $\mathbb{I}_k$ is updated as $\mathbb{I}_k = \mathbb{I}_{k-1} \cup \{f_k\}$. Otherwise, $\mathbb{I}_k = \mathbb{I}_{k-1}$. In any case, the new residual is $\mathbf{Y}_k^{\perp} = \left(\mathbf{I} - \mathbf{Z}_{f_k} \mathbf{Z}_{f_k}^H\right) \mathbf{Y}_{k-1}^{\perp}$.

The whole iterative process is summarized in Table 5.1, where the iteration might be stopped when a specified number of distinct columns is selected if the sparsity is known, or the Frobenius norm of $\mathbf{Y}_k^{\perp}$ is smaller than a threshold. The selected columns of **Z** compose

the matrix $\mathbf{Z}_{\mathbb{I}_k}$, based on which the actual solution of $\mathbf{S}$ is obtained by solving a least square problem.

5.3.4 Joint-sparsity-based approach

The imaging performances are expected to be better once more prior information about the testing system is input. Here, following distinct and significant information about the composition of the desired solution is going to be made use of.

(1) Each column of $\mathbf{S}$ is sparse, *i.e.*, most of elements are of zero value. This knowledge is from general cases where only a few damaged fibers affect the laminate.

(2) Different columns of $\mathbf{S}$ should enjoy same sparsity profile due to the independence of the position of damaged fibers with emitting sources.

In this subsection, the former information is first explored in cases with single source (the second information is not available) to present the idea of sparsity and related reconstruction algorithm. The common sparsity of columns is investigated later with multiple sources in use.

Imaging with single emitting source

With a single emitting source, $\mathbf{S}$ becomes a column vector composed of N_f entries. As described, if the l-th fiber is defectuous, the corresponding element in $\mathbf{S}$ is non-zero. However, in general situations, only few fibers are faulty and, as a result, a few non-zero elements appear in $\mathbf{S}$, *i.e.*, $\mathbf{S}$ is sparse.

To take advantage of this prior information, the sparsity level (or number of non-zero elements) is measured and the straightforward regularization is enforcing l_0-norm on $\mathbf{S}$, which is defined as

$$||\mathbf{S}||_0 = \#\{i, S_i \neq 0\} \tag{5.15}$$

counting the number of non-zero elements, S_i the i-th element of $\mathbf{S}$. Then, constraining the data discrepancy, the solution is obtained by running the optimization

$$\hat{\mathbf{S}} = \arg\min ||\mathbf{S}||_0, \text{ s.t. } ||\mathbf{Y} - \mathbf{Z}\mathbf{S}||_2^2 \leq \tau^2, \tag{5.16}$$

where the parameter τ is decided by the noise variance. Unfortunately, the exhaustive enumeration of all possible locations of non-zero entries is required in solving this l_0-norm optimization problem, *i.e.*, a NP hard problem [51]. An alternative sparsity measuring form

Table 5.2 Procedure to retrieve $\mathbf{S}$.

1.	Initialization: $\mathbf{S}^{(0)}$ and $k=0$;
2.	Update $\Pi(\mathbf{S}^{(k)})$ and $\beta^{(k)}$ based on the L-curve method, then $\mathbf{S}^{(k+1)}=\left[\mathbf{Z}^H\mathbf{Z}+\beta^{(k)}\Pi(\mathbf{S}^{(k)})\right]^{-1}\mathbf{Z}^H\mathbf{Y}$ and $k=k+1$;
3.	If $\left\|\mathbf{S}^{(k)}-\mathbf{S}^{(k-1)}\right\|_F<\zeta$, stop; otherwise, repeat step 2.

that is amenable to optimization algorithms is used. The l_p-norm [46] defined as

$$||\mathbf{S}||_p^p=\sum_{i=1}^{L}|S_i|^p\,,\ 0\le p\le 1, \tag{5.17}$$

could provide a good approximation of l_0-norm and the corresponding optimization problem

$$\hat{\mathbf{S}}=\arg\min||\mathbf{S}||_p^p,\ \text{s.t.}\ ||\mathbf{Y}-\mathbf{Z}\mathbf{S}||_2^2\le\tau^2, \tag{5.18}$$

is solved by applying the factored-gradient approach [46, 52] on the Lagrangian expression

$$\hat{\mathbf{S}}=\arg\min J(\mathbf{S})=||\mathbf{Y}-\mathbf{Z}\mathbf{S}||_2^2+\gamma||\mathbf{S}||_p^p, \tag{5.19}$$

where γ is the introduced Lagrangian multiplier or regularization parameter trading off the sparsity of $\mathbf{S}$ and the quality of data fit [53]. As γ increases, more weight would be put on the sparsity and vice versa.

Denote the gradient of (5.19) as $\nabla J(\mathbf{S})$. A necessary condition of the optimal $\mathbf{S}$ is $\nabla J(\mathbf{S})=0$, yielding

$$\nabla J(\mathbf{S})=2\mathbf{Z}^H\mathbf{Z}\mathbf{S}-2\mathbf{Z}^H\mathbf{Y}+2\beta\Pi(\mathbf{S})\mathbf{S}=0 \tag{5.20}$$

where $\beta=p\gamma/2$ and $\Pi(\mathbf{S})=\text{diag}\left\{\left|S_i^2+\epsilon\right|^{p/2-1}\right\}$. ϵ should be small enough not to affect the behavior of the solution; however, too small ϵ may cause ill-conditioned $\Pi(\mathbf{S})$. $\epsilon=10^{-3}\max\{S_i\}$ is shown proper by numerical experiments. Equation (5.20) suggests the following iterative formula

$$\mathbf{S}^{(k+1)}=\left[\mathbf{Z}^H\mathbf{Z}+\beta\Pi\left(\mathbf{S}^{(k)}\right)\right]^{-1}\mathbf{Z}^H\mathbf{Y}, \tag{5.21}$$

based on which the procedures retrieving $\mathbf{S}$ are summarized in Table 5.2, where $\mathbf{S}^{(k)}$ is the retrieved solution in the k-th iteration, the parameter ζ depends on the norm of $\mathbf{S}$, and the regularization parameter β, or γ, is updated at each iteration in order to ensure the tradeoff as mentioned being effectively forced.

Imaging with multiple emitting sources

Two ways dealing with multi-source cases are illustrated, one through simple reformations of involved matrices [54] to still apply the approach for single source and the other via the proper measurement of joint sparsity to dig the independence of the position of defects with sources. The second way is the only followed in this chapter, but a brief description of the first is given below because of its common use.

For the first way, $\mathbf{Z}$ is expanded as $\ddot{\mathbf{Z}} = \mathbf{I} \otimes \mathbf{Z}$, $\otimes$ denoting Kronecker product, while $\mathbf{Y}$, $\mathbf{S}$ and $\mathbf{N}$ are reformatted as a vector through the vectorization by taking columns one under another. Denote the reformatted matrices or vectors by adding two dots above the initial notations. Then (5.8) is rewritten as

$$\ddot{\mathbf{Y}} = \ddot{\mathbf{Z}}\ddot{\mathbf{S}} + \ddot{\mathbf{N}}. \tag{5.22}$$

Correspondingly, the updated optimization

$$\hat{\mathbf{S}} = \arg\min J(\mathbf{S}) = ||\ddot{\mathbf{Y}} - \ddot{\mathbf{Z}}\ddot{\mathbf{S}}||_2^2 + \gamma||\ddot{\mathbf{S}}||_p^p, \tag{5.23}$$

yields the solution of $\mathbf{S}$ and the fiber profile is the curve of vector $\hat{\mathbf{s}}$, where $\hat{\mathbf{s}} = [\hat{s}_f]$ and $\hat{s}_f = ||\hat{\mathbf{S}}^f||_2$, $f = 1, 2, \ldots, N_f$, $\hat{\mathbf{S}}^f$ being the f-th row of $\hat{\mathbf{S}}$.

As observed, after reformations, the method for single source can be directly applied to cases with multiple sources. However, the largely increased dimension of the involved matrices brings a possible heavy computational burden and the prior knowledge, joint sparsity of the solution, is not explored this way.

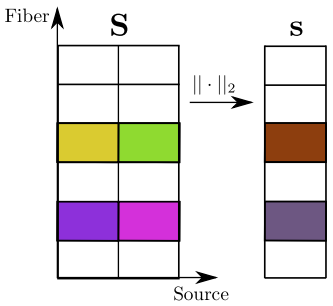

Fig. 5.1 Sketch of nonzero elements in $\mathbf{S}$ and the measurement of joint sparsity

An alternative approach, where the joint sparsity is properly measured, is implemented. Due to the independence from sources, the position of nonzero entries in $\mathbf{S}$ has the structure as sketched in Fig. 5.1. Rows corresponding to sound fibers would be zero in $\mathbf{S}$. To combine

the information among different columns, a l_2-norm is first enforced on each row of $\mathbf{S}$, such way compressing the joint sparsity into the sparsity of the generated vector $\mathbf{s}$.

Define the vector $\mathbf{s} = [s_f]$ and $s_f = ||\mathbf{S}^f||_2$, the superscript f denoting the f-th row. Measuring the sparsity of $\mathbf{s}$ by the p-norm, solving the optimization problem

$$\hat{\mathbf{S}} = \arg\min ||\mathbf{s}||_p^p, \text{ s.t. } ||\mathbf{Y} - \mathbf{Z}\mathbf{S}||_F^2 \leq \tau^2, \tag{5.24}$$

leads to the solution of $\mathbf{S}$. Apply the factored-gradient approach on the Lagrangian expression

$$\hat{\mathbf{S}} = \arg\min J(\mathbf{S}) = ||\mathbf{Y} - \mathbf{Z}\mathbf{S}||_F^2 + \gamma ||\mathbf{s}||_p^p. \tag{5.25}$$

Taking the gradient of the penalty function and letting it equal to zero, the same iterative formula (5.29) is obtained, except the definition of $\Pi(\mathbf{S})$ is now updated as [31, 46]

$$\Pi(\mathbf{S}) = \text{diag}\left\{||\mathbf{S}^f||_2^{p-2}\right\}, f = 1, 2, \ldots, N_f. \tag{5.26}$$

Then the algorithm runs with procedures in Table 5.2.

Reduce noise effects by mapping the data on signal space

Efforts are made to reduce the noise effects. In MUSIC algorithm, the noise space of the left eigenvectors, *i.e.*, $\mathbf{U}^n$, is used and its orthogonality to the basis vector $\mathbf{Z}_f$ leads the estimator of the fiber profile. Following a similar idea, the noise effects are reduced by exploiting the orthogonality of the noise to the signal space $\mathbf{V}^s$.

Pre-process the data matrix $\mathbf{Y}$ by multiplying $\mathbf{V}^s$ on its right side, then we have the rewritten version of the data equation

$$\mathbf{Y}\mathbf{V}^s = \mathbf{Z}\mathbf{S}\mathbf{V}^s + \mathbf{N}_a\mathbf{V}^s + \mathbf{N}^0\mathbf{V}^s, \tag{5.27}$$

and the term related with the additive noise is expected to be canceled. Equation (5.27) has the simple form

$$\mathbf{Y}_{sv} = \mathbf{Z}\mathbf{S}_{sv} + \mathbf{N}_{sv}, \tag{5.28}$$

with new notations $\mathbf{Y}_{sv} = \mathbf{Y}\mathbf{V}^s$, $\mathbf{S}_{sv} = \mathbf{S}\mathbf{V}^s$, and $\mathbf{N}_{sv} = \mathbf{N}^0\mathbf{V}^s$. Sharing the same equation form with (5.8), the information about the fiber profile can be retrieved with the algorithm described above.

Determination of regularization parameter with L-curve method

The regularization parameter γ is updated at each iteration in order to ensure the suitable tradeoff between the sparsity of the solution and data error in the optimization problem of (5.25).

At each iteration, $\mathbf{S}$ is updated by the formula

$$\mathbf{S}^{(k+1)} = \left[\mathbf{Z}^H\mathbf{Z} + \beta^{(k)}\Pi\left(\mathbf{S}^{(k)}\right)\right]^{-1}\mathbf{Z}^H\mathbf{Y}. \tag{5.29}$$

Denoting $\Pi(\mathbf{S}^{(k)}) = \Xi^{-2}(\mathbf{S}^{(k)})$ and $\mathbf{Z}^{(k)} = \mathbf{Z}\Xi(\mathbf{S}^{(k)})$, (5.29) is rewritten as

$$\mathbf{S}^{(k+1)} = \Xi(\mathbf{S}^{(k)})\left[(\mathbf{Z}^{(k)})^H\mathbf{Z}^{(k)} + \beta^{(k)}\mathbf{I}\right]^{-1}(\mathbf{Z}^{(k)})^H\mathbf{Y}, \tag{5.30}$$

which is the solution of the optimization problem

$$\min J^{(k)}(\mathbf{W}) = ||\mathbf{Y} - \mathbf{Z}^{(k)}\mathbf{W}||_F^2 + \beta^{(k)}||\mathbf{W}||_F^2 \text{ s.t. } \mathbf{S}^{(k+1)} = \Xi(\mathbf{S}^{(k)})\mathbf{W}. \tag{5.31}$$

Thus a l_2-norm optimization problem is solved at each iteration and the L-curve method introduced for finding the regularization parameter in a l_2-norm optimization [27] can be used.

As $\beta^{(k)}$ increases from 0 to ∞, $||\mathbf{W}||_F^2$ would decrease from $||\mathbf{Y} - \mathbf{Z}^{(k)}\mathbf{W}||_F^2$ to zero and, however, $||\mathbf{Y} - \mathbf{Z}^{(k)}\mathbf{W}||_F^2$ will monotonically increase. The L-curve proposes that as $\beta^{(k)}$ varies, the plot of $||\mathbf{W}||_F^2$ versus $||\mathbf{Y} - \mathbf{Z}^{(k)}\mathbf{W}||_F^2$ has a L shape and the optimal value of $\beta^{(k)}$ is located at the corner, *i.e.*, the point having the maximum curvature.

Setting $\rho(\beta^{(k)}) = ||\mathbf{Y} - \mathbf{Z}^{(k)}\mathbf{W}||_F^2$ and $\eta(\beta^{(k)}) = ||\mathbf{W}||_F^2$, the optimal $\beta^{(k)}$ locates at

$$\max_{\beta^{(k)}} \kappa(\beta^{(k)}) = \frac{\rho'\eta'' - \rho''\eta'}{[(\rho')^2 + (\eta')^2]^{3/2}} \tag{5.32}$$

where κ is the computed curvature and the symbol (double) prime denotes the (second) derivative. Denote $\mathbf{U}$, $\mathbf{V}$ as matrices consisting of left and right singular vectors of $\mathbf{Z}^{(k)}$, respectively, and σ_j as the j-th singular value. The solution of $\mathbf{W}$ has the expression

$$\mathbf{W}(\beta^{(k)}) = \sum_{s=1}^{N_s}\sum_{j=1}^{N_r}\left(\frac{\sigma_j\mathbf{U}_j^H\mathbf{Y}_s}{\sigma_j^2 + \beta^{(k)}}\right)\mathbf{V}_j. \tag{5.33}$$

Substitution into the expression of ρ and η gives the closed-form solution of their first and second derivatives.

5.4 Numerical results

Simulations are performed on a single-layer laminate and a multilayer one. All types of defects of interest, including missing, displaced, expanded, shrunk fibers and circular inclusions, are considered for each case. Only a wave with TM polarization is concerned however.

Three parameters, the parameter p and ζ, $\mathbf{S}^{(0)}$ in Table 5.2, need to be determined in the application of the joint-sparsity-based method. p should be in the range $0 < p \leq 1$. However, large p leads to a slow convergence rate while small one has the risk to have a local optimal solution. $p = 0.8$ is shown proper to provide a good tradeoff in numerical trials. ζ and $\mathbf{S}^{(0)}$ are set as 10^{-3} and $\mathbf{0}$ herein, respectively.

5.4.1 Single-layer laminate

Tests are made with a laminate in air composed of an epoxy slab (relative permittivity $\epsilon_{rs} = 3.6$, loss tangent $\tan\delta = 0.02$) and graphite fibers ($\epsilon_{rf} = 12$, conductivity $\sigma_f = 300$ S/m) (just mention that testing of graphite-fibered composites is of much interest [2].) The fiber period $d = 0.1$mm and the radius $c = 0.25d$. The slab is bounded by planes $z = 0.5d$ and $z = -0.5d$, while the global coordinate system is originated at the fiber center with index 0. Complex defects are assumed happening to better test the imaging capabilities. Specifically, the -5-th and 5-th fibers are assumed missing, the 0-th fiber is shrunk with radius $c_0 = 0.7c$, the -3rd fiber has a displacement of $(\delta x, \delta z) = (0.2c, 0.2c)$, and a circular inclusion with radius $0.2c$ and center $(0.55c + 2d, 0.55c)$ is inside the 2nd fiber.

First, the effects from zero-order approximation are first estimated. Put a line source emitting wave $H_0^{(1)}(k_0 r_s)/i4$ above the laminate at $\mathbf{r}_s = (0, d)$, i imaginary unit, k_0 wavenumber of upper half space and r_s the distance between the observation point and source. Varying the incident wavelength, the defined relative approximation error

$$\varepsilon(\lambda^{inc}) = ||\mathbf{Y} - \mathbf{Y}^0||_2 / ||\mathbf{Y}||_2 \tag{5.34}$$

is plotted in Fig 5.2(a), where $\mathbf{Y} = [Y_j]$, Y_j accurate solution of field value at $(-10d + jd/5, d)$, $j = 1, 2, \ldots, 100$, and $\mathbf{Y}^0$ is the data vector after approximation. With the increased wavelength, the relative error monotonically decreases and is $< 1\%$ when $\lambda^{inc}/d > 10^2$, *i.e.* the frequency $f < 30$ GHz which is the band fitting practical requirements. Comparing the intensity of sampled values when $f = 30$ GHz, the discrepancy is quite small and bearable as proved by the following imaging results.

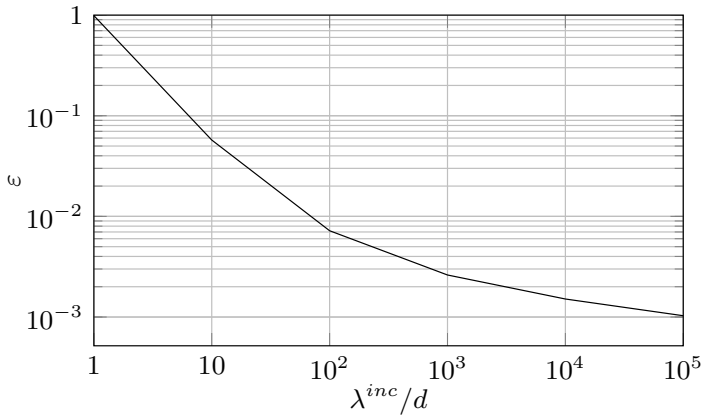

(a)

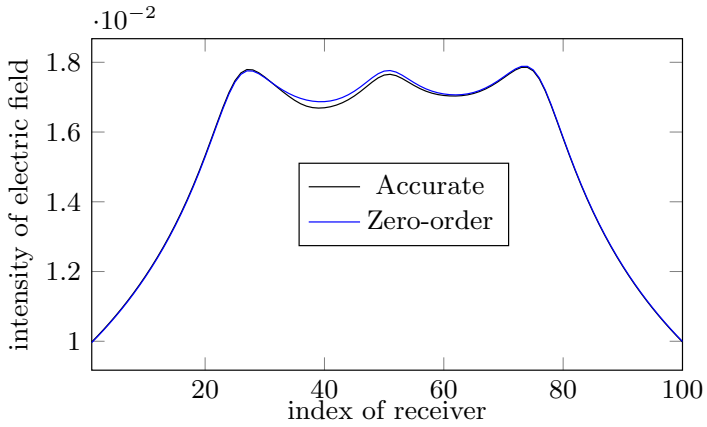

(b)

Fig. 5.2 Estimation of introduced errors due to the zero-order approximation, source at $\mathbf{r}_s = (0, d)$, (a) the defined relative error versus changed wavelength, (b) comparisons of field intensity with $\lambda^{inc} = 100d$.

Add more sources, 100 in total, to get more information about the defects. The sources share same position with receivers (observation points). By sequentially exciting sources, the received measurement vectors compose the MSR data matrix. Take the singular value decomposition of the data matrix, the distribution of singular values is shown in Fig. 5.3. Although five fibers are damaged, only three main values appear due to the small size of the circular inclusion and the small displacement of the displaced fiber. Therefore, in MUSIC and the joint-sparsity method, singular vectors corresponding to these three values compose the signal space. Remark that the determination of signal and noise spaces is not decided manually, but employing the numerical L-curve method (not the analytical one described in this chapter) in [50].

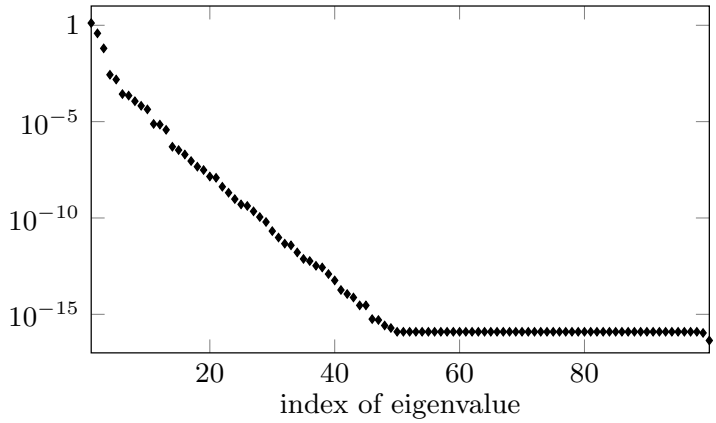

Fig. 5.3 Distribution of singular values of the data matrix, $\lambda^{inc} = 100d$.

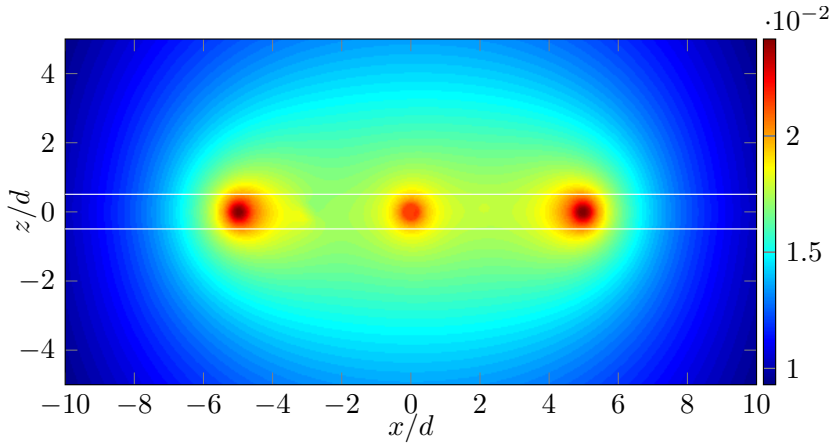

Fig. 5.4 Map of anomalous field when $\lambda^{inc} = 100d$, line source at $(0, d)$, white lines indicating the slab boundaries, graphite fiber and epoxy matrix.

When the line source is at $\mathbf{r}_s = (0, d)$, the effects of defects can be observed from the map of the anomalous field in Fig. 5.4, where two missing fibers and the shrunk fiber behave like sources and, due to the small distance between each other, their scattered fields are merged as one beam. As the size of inclusion and the displacement of the displaced fiber is small, there is no obvious conclusion.

With collected data from multiple sources and receivers, assuming the signal-noise-ratio (SNR) is 40dB, the detection results are shown in Fig. 5.5, where the true index of damaged fibers is indicated by the vertical dashed lines. As seen, the least square solution fails to detect the defects. It is hard to say if the 0-th fiber is damaged from the curve though one peak appears at the corresponding position. Three damages are found by M-BMP, but the location of missing fibers is misplaced. The poor performances of least square and M-BMP might be due to the effect of noise and approximation error. Since the wavelength is much

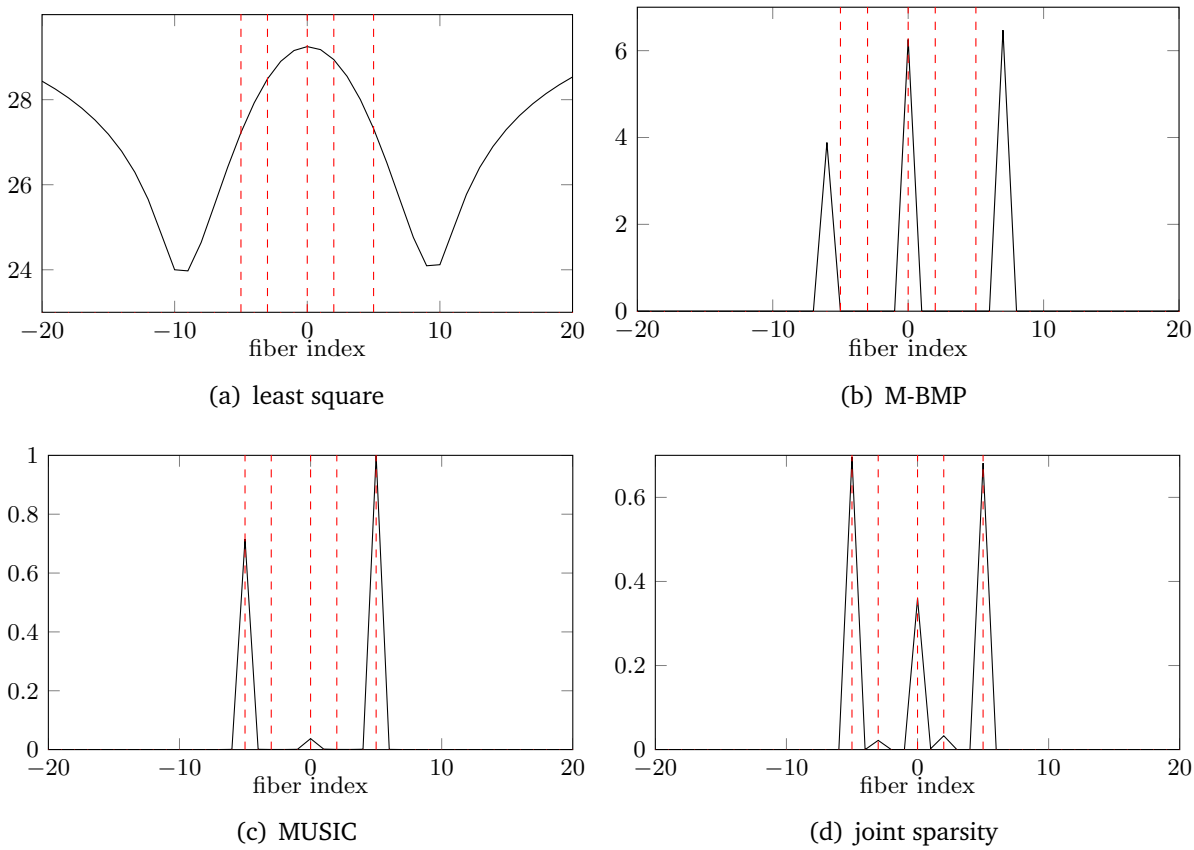

(a) least square (b) M-BMP

(c) MUSIC (d) joint sparsity

Fig. 5.5 Imaging results with different reconstruction algorithms, $\lambda^{inc} = 100d$, vertical dashed lines indicating the true index of damaged fibers.

larger than the fiber period, different basis vectors are only with small difference. As a result, if the algorithm is not robust enough, pseudo peak or shifted ones would show up. For MUSIC, the noise effect has been reduced through the utilization of signal space, so a better detection result is obtained. From the normalized estimation results, we can see that two missing fibers and the shrunk one are accurately located. However, due to the low energy of the equivalent source, the displaced fiber and inclusion are not found at all. Making use of more information about the desired solution, the joint-sparsity-based approach has the advantage to find fibers mixed with large and small defects. As observed, all damaged fibers are accurately estimated.

Lower-frequency waves are preferred in practice due to the low cost on equipments. Letting the incident wavelength $\lambda^{inc} = 1000d$, *i.e.* the frequency $f = 3$ GHz, the map of anomalous field and the imaging results are shown in Fig. 5.6 and Fig. 5.7. As the wavelength is larger, the defects would less impact the propagation of the wave. Consequently, the amplitude of the map in Fig. 5.6 is smaller than the one in Fig. 5.4. That brings up

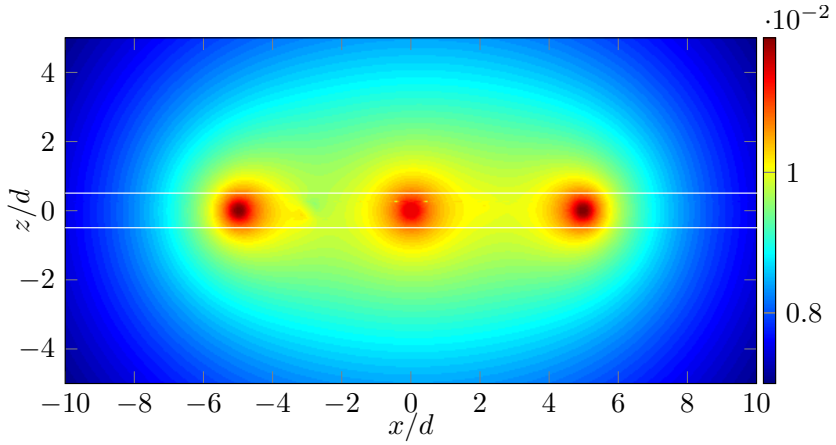

Fig. 5.6 Map of anomalous field when $\lambda^{inc} = 1000d$, $\mathbf{r}_s = (0, d)$, white lines indicating the slab boundaries, graphite fiber and epoxy matrix.

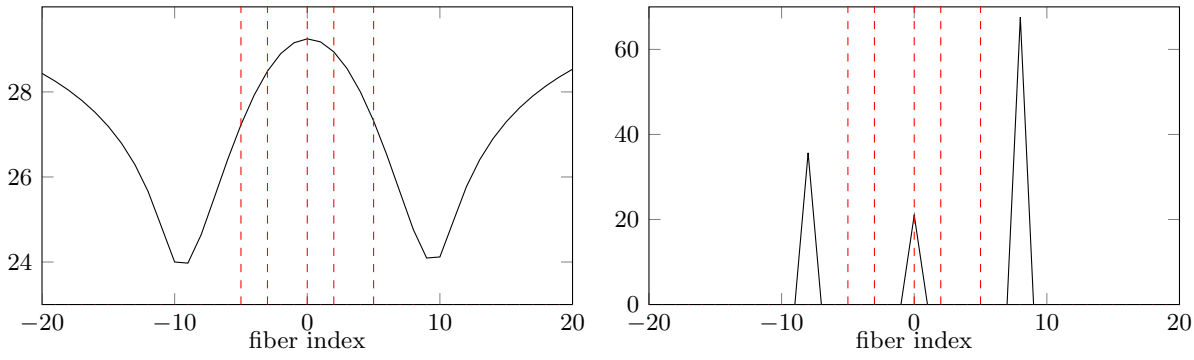

(a) least square (b) M-BMP

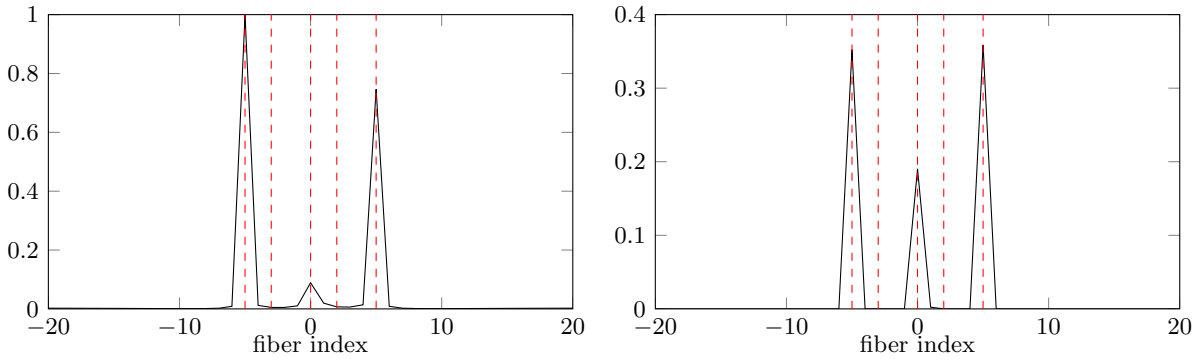

(c) MUSIC (d) joint sparsity

Fig. 5.7 Imaging results with different reconstruction algorithms, $\lambda^{inc} = 1000d$, vertical dashed lines indicating the true index of damaged fibers.

the challenge of imaging algorithms. The solutions from least square and M-BMP still cannot provide an estimation of defects. MUSIC has the same performance as the one with

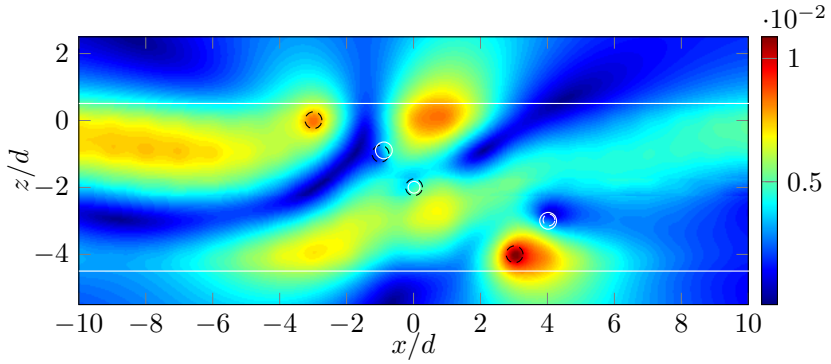

Fig. 5.8 Map of anomalous field when $\lambda^{inc} = 10d$, line source at $(0, d)$, glass fiber and epoxy matrix, white lines standing for the laminate boundaries and defects and black ones for the initially undamaged fibers.

$\lambda^{inc} = 100d$, except slight sidelobes near peaks. Exploring the joint sparsity, although three of defects can be correctly identified, the two small ones are lost.

5.4.2 Multilayer laminate

A 5-layer laminate with glass ($\epsilon_{rf} = 6$) fibers embedded is tested. The structure of layers is identical. For each layer, the fiber period $d = 0.1$mm, radius $c = 0.25d$, and the slab thickness equals d. Assume that the $(1,-3)$-th and $(5,3)$-th fibers are missing, the $(2,-1)$-th fiber is with displacement $(\delta x, \delta z) = (0.1d, 0.1d)$, the $(3,0)$-th fiber is shrunk with radius $0.7c$, and an inclusion is inside the $(4,4)$-th fiber with radius $0.7c$.

With a line source illumination from the upper half space, the map of the anomalous field is drawn in Fig. 5.8 when $\lambda^{inc} = 10d$. The impact from missing fibers seems stronger than from others and the most impacted region above the laminate is $-5d < x < 4d$.

Similarly with the imaging system for the single-layer laminate, 100 sources and receivers uniformly positioned along $z = d$, $-10d \le x \le 10d$ are utilized to collect the information, and SNR=40dB. The singular-value distribution of the data matrix is shown in Fig. 5.9. Five defects appear as main values while one of them is relatively small. From the imaging results in Fig. 5.10, we can see the relatively small one corresponds to the displaced fiber. Least square collapses in this case. M-BMP accurately estimates three damaged fibers, but the displaced fiber is lost and one pseudo-peak emerges at the position of $(5,2)$-th fiber, which is undamaged. MUSIC gives an good estimation of all defects except the displaced fiber and, benefiting from the exploration of joint sparsity, this displaced fiber is finally found in Fig. 5.10.

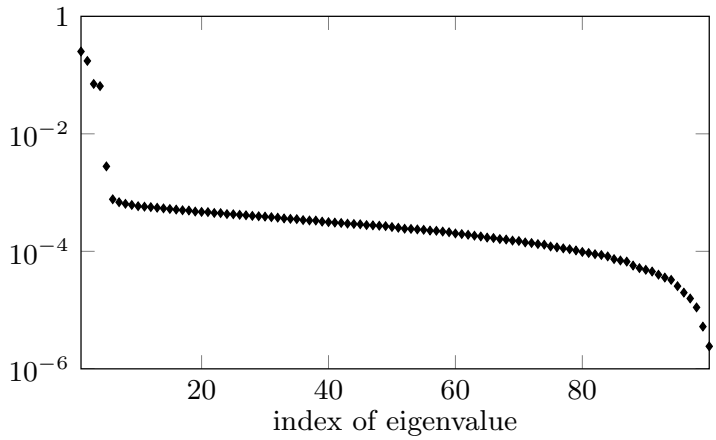

Fig. 5.9 Distribution of singular values of the data matrix, $\lambda^{inc} = 10d$.

An investigation about the location of damages is made on the same laminate, except the fiber material is changed as graphite. Assume two missing fibers with index $(l, -1)$ and $(l, 2)$ appear and l changes from 1 to 4 (the damages “move" deeper and deeper). With the same distribution of sources and receivers, setting $N = 2$, the testing results are shown in Fig. 5.11. As observed, when $l \leq 3$, the missing fibers are correctly located. However, due to the material losses, the field disturbance due to damages in deep layers are hard to be observed and, as a result, the testing system fails when $l = 4$.

5.5 Summary

With the equivalence theory, several types of damaged fibers are located simultaneously in this chapter. As defects are modeled as equivalent sources inside the initially undamaged fibers, the goal turns to simply finding the equivalent sources instead of the complicated details of defects. The data are collected by receivers with multiple sources in function. Reconstruction algorithms including least square, basic matching pursuit, MUSIC and the joint-sparsity-based approach provide the estimations.

Numerical results on single-layer and multilayer laminates show the advantages of exploring the joint sparsity, especially on identifying the defects with little field disturbance. However, when the frequency is quite low, like $f = 3$ GHz in Fig. 5.7, the imaging resolution still needs improvements.

The uniqueness of the inverse problem concerned here is not fully addressed yet, and should be done on that aspect via numerical tests.

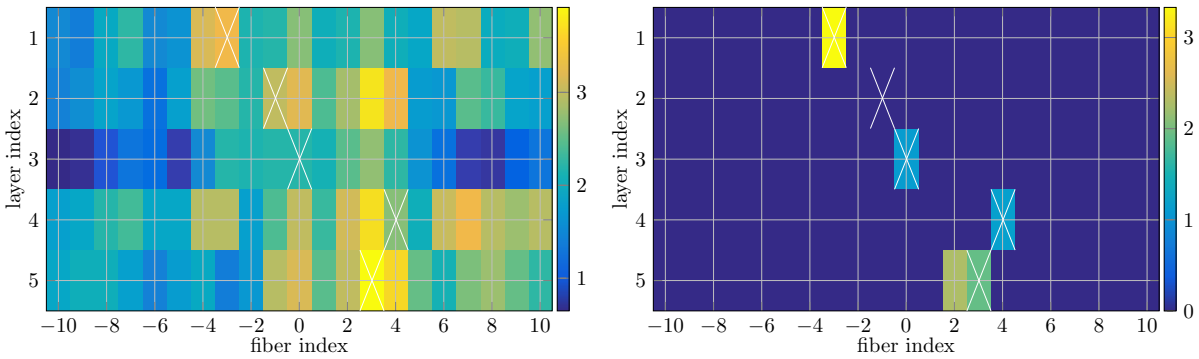

(a) least square

(b) M-BMP

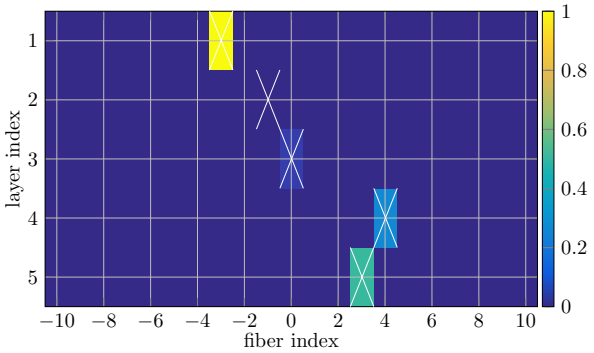

(c) MUSIC

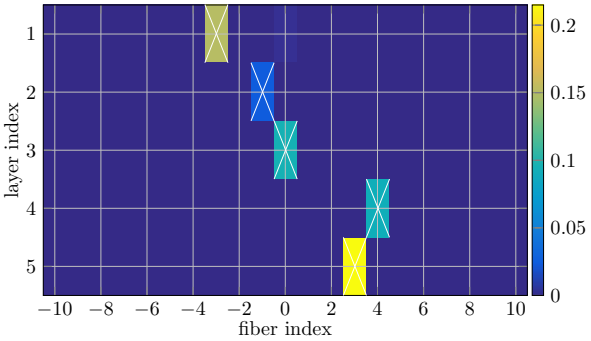

(d) joint sparsity

Fig. 5.10 Imaging results of defects in the 5-layer laminate, $\lambda^{inc} = 10d$, cross lines indicating the true index of damaged fibers.

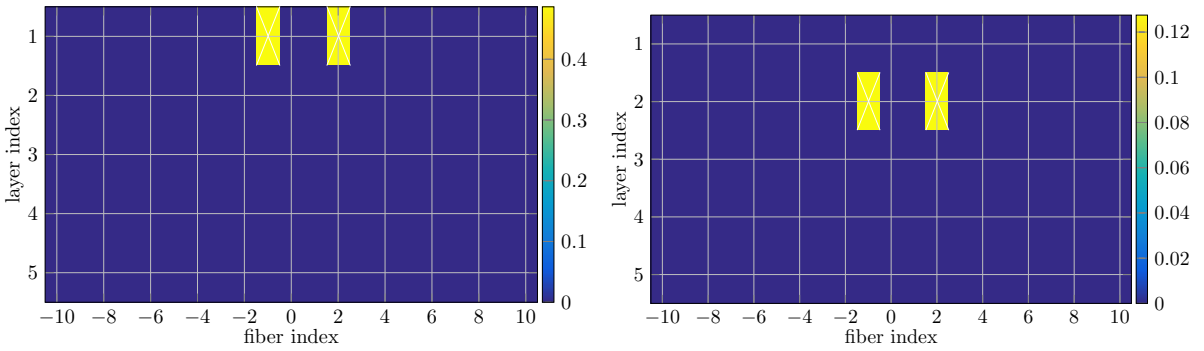

(a) damages at the 1st layer

(b) damages at the 2nd layer

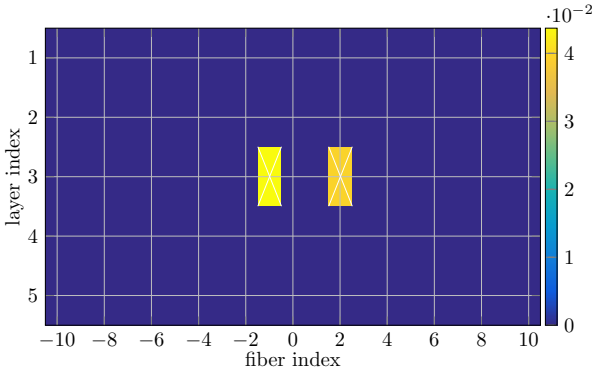

(c) damages at the 3rd layer

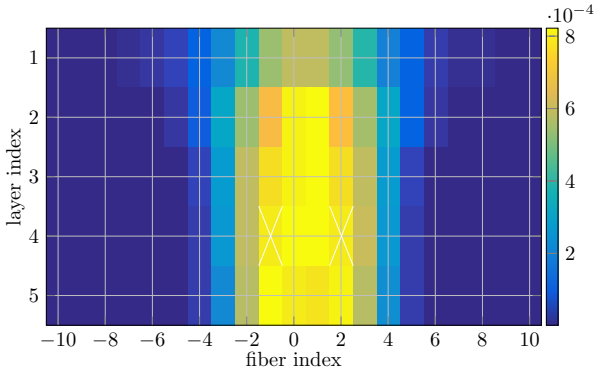

(d) damages at the 4th layer

Fig. 5.11 Imaging results of the 5-layer laminate in cases with missing fibers moving deeper and deeper, $\lambda^{inc} = 10d$, cross lines indicating the true location of damaged fibers.

Chapter 6

Conclusion and Perspectives

Conclusion

The fast modeling and high-resolution imaging of defects in fiber-reinforced multilayered laminates are focused onto in this thesis. Each layer of the laminate is assumed to be composed of periodically positioned circular cylindrical fibers embedded inside a homogeneous slab. Fiber orientations in adjacent layers are limited to be the same. Numerical results show the applicability of the proposed approaches on analyzing various fiber and slab materials, such as glass, graphite fibers and epoxy or polyester slabs. The achieved works are expected to enrich the understanding of electromagnetic behaviors due to defects and detection performances with several imaging algorithms.

The work starts with the direct modeling of single-layer laminates. For the undamaged structure, the combination of periodic fibers and a homogeneous slab generates a composite enjoying the periodic property, which enables the application of Floquet-theorem-based methods. However, this periodicity is destroyed if any defect inside. Taking a truncation of the laminate centered at defective region as an elementary cell (named supercell) and repeating the cell periodically, a non-periodic structure is turned into one with periodicity, so that methods developed for periodic structures, based on Floquet theorem, can be brought to bear. However, fictitious defects are also periodically arranged beside the real ones, which requires that the transverse size of the supercell is large enough so that the field inside, near the defects, can be accurately approximated. Such modeling approach is directly used to tackle plane-wave illuminations with TM or TE polarization.

Line-source illuminations are approached by expanding the emitting wave into planar ones, the overlap of corresponding responses reconstituting the true field solution. The reconstitution, actually an integration, is completed with the help of numerical methods. The singularities, including poles and branch cuts, of the integrand tend to prevent the

computation from high efficiency, however, which can be indeed avoided by detouring the integration path. An efficient computational method with respect to multiple integrations is also concerned. When the distance between observation points is much smaller than the wavelength, the plots of related integrands would have similar shape, indicating that most of sampling points of the integration variable are common. Such a similarity provides the possibility to carry out multiple integrations simultaneously. The discrepancy of different integrands is considered as well by building the set of observation points in the numerical algorithms. The set is initialized as the indexes of all observation points and updated during the computation by deducting the elements satisfying the requirement of accuracy.

Plane/cylindrical wave expansions of fields in all regions of the laminate pave the way to the foundation of the modeling. However, these infinite series are impossible to be operated with, thus have to be truncated properly without losing accuracy. The truncation number for CWEs is estimated by the formula in [18], and the one for PWEs is determined by the proposed numerical strategy where the knowledge that field values computed from CWEs and PWEs should be the same in the slab, is made proper use of.

Although the supercell-based approach could provide a well approximated solution, the required supercell size can be large, especially in cases with lossless materials and low-frequency incident waves. Since the computation complexity is a cube of the supercell size, the modeling efficiency is not guaranteed. This led us to develop an alternative approach so as to give a fast solution.

Only missing, displaced, expanded, shrunk fibers and circular inclusions are considered. Benefiting from aforementioned circular shapes, their scattering behaviors are conveniently analyzed via the expansion of fields into cylindrical waves, while fiber boundary conditions and the Graf's addition theorem are applied in order to find linear relations between expansion coefficients. The equivalence theory comes from the reformulation of these relations and the impacts of defects are modeled as equivalent sources set inside the corresponding sound fibers. According to the linearity of scattering, the final solution is but a summation of responses due to the exterior illuminating source and interior equivalent ones. As a result, after the equivalence, the investigated object changes from the damaged laminates to its initially sound structure.

While the exterior illumination could be analyzed with methods for periodic structures, the array scanning method is utilized to find the solution for inner sources. Repeating the source along the line connecting fiber centers with fiber period, the periodicity destroyed by the source is recovered and the field distribution becomes quasi-periodical by additionally putting a specific phase on each source. The fabricated phased array is analyzed with

quasi-periodic theories and the final solution follows an integration over the first Brillouin zone.

The efforts paid on the modeling of single-layer laminates are easily profited from for multilayer structures. In different layers, the material and size of composed fibers and slabs might differ in order to improve the stiffness and resistance to corrosion. Treating types of defects as equivalent sources inside the fibers, the total field is a summation of contributions from the illuminating source and the equivalent ones, the analysis of which is conducted via building up the scattering matrices. For each layer, expressing fields in PWEs, the linear relations between expansion coefficients are found by matching modes on slab boundaries and analyzing the fiber array with multipole method. The scattering matrix for each layer is obtained from these linear relations and the one linking different layers is computed with a recursive scheme. The prior knowledges, covering the incident wave and no illumination from the bottom, play the key role and scattering matrices make it possible to reach the solution of expansion coefficients of all layers.

The equivalence theory provides an efficient way not only to the accurate and fast modeling of damaged laminates but also about the possibility of locating types of defects simultaneously. Since the defects' electromagnetic behaviors are explained as the consequence of sources inside fibers, the goal now becomes finding fibers which include equivalent sources, instead of reconstructing the electromagnetic parameters (like relative permittivity or conductivity) of the whole laminate, as described in many references.

Four popular algorithms are used to find the indexes of damaged fibers from the data collected by receivers above the laminate. The minimization of the data discrepancy leads to the least square solution. Making use of the orthogonality of the basis vector with respect to the noise space of data matrix, MUSIC provides the estimation of fiber profile by scanning all basis vectors. A classical subset selection method, basic matching pursuit, is utilized as well. Each selected index is achieved by sequentially mapping the data on all basis vectors and selecting the one having the minimum residual. Emphasis is put on the utilization of the joint-sparsity of the desired solution. Measuring the sparsity through the mixture of l_2-norm and l_p-norm ($0 < p \leq 1$), the solution is obtained by minimizing the penalty function, in which the tradeoff between the sparsity and data discrepancy is made by deriving the regularization parameter with L-curve method. This optimization problem here is iteratively solved by applying the factored-gradient approach.

All theories above have been illustrated by various numerical results. For the direct modeling, the finite-element software COMSOL provides the reference for the validation, and the accuracy of the solution is checked by testing the reciprocity theorem. Imaging performances are considered by examples on both single-layer and multilayer laminates.

Perspectives

In the present works, only defects with circular cross sections are concerned. However, the available solution of the Green's function provides the possibility to analyze irregularly-shaped damages with a method of moments and proper field integral formulation. Similar methodology applies on analyzing arbitrarily-shaped periodic unit (not limited by the circular cross section) with the periodic Green's function [55, 56] of the layered medium. Only plane waves and line sources are considered here, yet other types could be operated by exploiting their PWEs [24, 44].

In this thesis, to reduce the complexity and difficulty in modeling and imaging, fiber orientations in adjacent layers are constrained be the same. However, as the ultimate goal of such an investigation, the full 3D analysis intrinsic to the laminate topology (like various fiber orientations, volumetric inclusions) and source type (like current loop in practice or dipole related with the dyadic Green's function) needs to be investigated. The work presented in [1], where undamaged multi-layered laminates with arbitrarily rotated fibers (thus 3D topology) are accurately and efficiently analyzed, can be the first step in modeling. Although only illuminations by planar wave and Gaussian beam are considered in [1], 3D sources might be handled with the exploration of PWE or the application of ASM for dipole (the arrangement of fictitious phased dipoles on a planar surface and a 2D Sommerfeld integration are expected).

Since enjoying similar features, illumination of disorganized photonic-crystal fibers (PCFs) could be analyzed likewise. In PCFs, the advantageous optical properties arise from the existence of photonic band gaps, the frequency bands in which propagating-wave solutions are not allowed [25, 57]. One of the exciting applications of PCFs is to confine the light to the introduced defects in a photonic band gap, named defect mode or quasimodes with a complex frequency. The equivalence theory presented in this thesis actually provides a helpful tool for calculation of the modes of localized defects. Selecting the frequency so as the matrix in (4.32) is singular, the desired defect modes could be approached. Similarly, the equivalent theory applies on a mode analysis to characterize the acoustic behaviors of a poroelastic layer leading to high acoustic absorption [58].

At large scale, the homogenization of the undamaged single-layer laminate has been achieved in [9] and for a multilayer it is possible to operate from layer to layer, while the defects might act as inclusions inside the layered homogeneous plates. Then the scattered field can be recovered with the preferred quasimode expansion method in [59] due to its capacity to mode analysis and accuracy.

For the imaging, a super-resolution (relative to the Rayleigh limit) is pursued by the exploration of the named joint sparsity of the desired solution in this thesis. Other ap-

proaches can be applied as well to enhance the resolution. [60] states that an enhancement of imaging resolution via (if accurate enough by the present approach) homogenization of a sound laminate is expected, conditioned that far-field measurements are utilized. Also, the resonance in the structure at (or near) frequencies of defect modes is potentially leading to super-resolved imaging [61].

To conclude on the latter issue, the results presented in the thesis may be far from being enough to conclude about feasibility in the real world, since questions as reliability with respect to scarce uncertain data and the related one of optimal configurations of measurements have not been considered in their full depth in the present thesis. But it is foreseen that a combination of careful computational modeling (the defect modes possibly, the presently developed approaches) and proper priors (at first sight, mostly around sparsity) should enable super-resolution of defects in a fibered laminate as considered herein, in a broad frequency range.

Appendix A

Graf's addition theorem

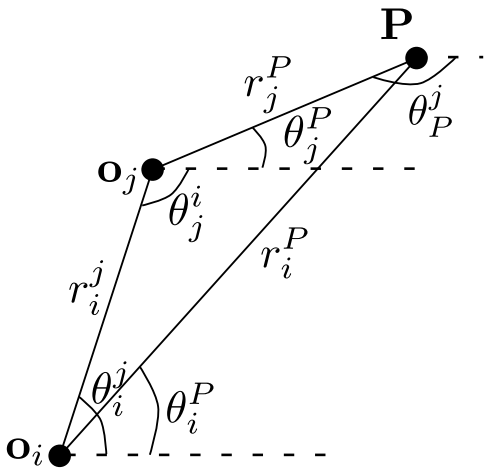

Fig. A.1 Application of the Graf's addition theorem.

Field near fibers are expanded into cylindrical waves and the expression is based on the local coordinate system originated at the fiber center. However, in the analysis of fiber array, expressing the field in the local coordinate system of another fiber is often required. The Graf's addition theorem [33] is used to make this transformation.

As sketched in Fig. A.1, $\mathbf{o}_i$ and $\mathbf{o}_j$ are centers of two fibers and $\mathbf{P}$ is the observation position. The distances between them satisfy $r_j^P < r_i^j < r_i^P$.

Assume the field value at $\mathbf{P}$ is with expression

$$V(\mathbf{P}) = H_m^{(1)}(kr_i^P)e^{im\theta_i^P}, \tag{A.1}$$

where (r_i^P, θ_i^P) are polar coordinates of $\mathbf{P}$ in the local coordinate system originated at $\mathbf{o}_i$. With condition $r_j^P < r_i^j$, (A.1)can be transformed as an equation expressed in the coordinate

system associated with $\mathbf{o}_j$, as

$$V(\mathbf{P}) = \sum_{n\in\mathbb{Z}} H_{m-n}(kr_i^j)e^{i(m-n)\theta_i^j} J_n(kr_j^P)e^{in\theta_j^P}. \tag{A.2}$$

Another form of (A.2) using θ_j^i, instead of θ_i^j, is given as

$$V(\mathbf{P}) = \sum_{n\in\mathbb{Z}} H_{n-m}(kr_i^j)e^{i(m-n)\theta_j^i} J_n(kr_j^P)e^{in\theta_j^P}. \tag{A.3}$$

Contrarily, we assume the field value at $\mathbf{P}$ is with expression

$$V(\mathbf{P}) = H_m^{(1)}(kr_j^P)e^{im\theta_j^P}, \tag{A.4}$$

and are trying to transform the expression into the one in the coordinate system originated at $\mathbf{o}_i$. Since $r_i^P > r_i^j$, the above procedures cannot be operated and an alternative way applying the Graf's addition theorem is developed.

Making use of the identity $H_m^{(1)}(kr_j^P)e^{im\theta_j^P} = (-1)^m H_m^{(1)}(kr_j^P)e^{im\theta_P^j}$, V is expressed in the coordinate system originated at $\mathbf{P}$. Applying the Graf's addition theorem with condition $r_i^P > r_i^j$, we have

$$\begin{aligned} H_m^{(1)}(kr_j^P)e^{im\theta_j^P} &= (-1)^m \sum_{n\in\mathbb{Z}} H_{n-m}(kr_i^P)e^{i(m-n)\theta_i^P} J_n(kr_i^j)e^{in\theta_i^j} \\ &= \sum_{n\in\mathbb{Z}} H_{m+n}(kr_i^P)e^{i(m+n)\theta_i^P} J_n(kr_i^j)e^{-in\theta_i^j} \\ &= \sum_{n\in\mathbb{Z}} J_{n-m}(kr_i^j)e^{i(m-n)\theta_i^j} H_n(kr_i^P)e^{in\theta_i^P}, \end{aligned} \tag{A.5}$$

which is the expression of V in the coordinate system about $\mathbf{o}_i$.

Appendix B

Born approximation with missing fibers

This appendix illustrates the application of the Born approximation in section 4.6 and involved notations have been defined in Chapter 4.

With missing fibers, the field disturbance can be valued via the Lippman-Schwinger formulation e.g., [32]

$$\tilde{V}(\mathbf{r}) - V(\mathbf{r}) = \sum_{(l,v)\in\mathbb{D}} \int_{D_l^v} G(\mathbf{r},\mathbf{r}_s') \left[(k_f^l)^2 - (k_s^l)^2 \right] \tilde{V}(\mathbf{r}_s') d\mathbf{r}_s', \tag{B.1}$$

where D_l^v is the cross-section of the (l,v)-th fiber, V stands for the field solution with the sound laminate and $\tilde{V}$ for the one with the damaged laminate. With large wavelengths, $\tilde{V}(\mathbf{r}_s') \approx V(\mathbf{r}_s')$, thus

$$\tilde{V}(\mathbf{r}) - V(\mathbf{r}) \approx \sum_{(l,v)\in\mathbb{D}} \int_{D_l^v} G(\mathbf{r},\mathbf{r}_s') \left[(k_f^l)^2 - (k_s^l)^2 \right] V(\mathbf{r}_s') d\mathbf{r}_s'. \tag{B.2}$$

Sampling fields above the laminate, G has the PWE expression with coefficients g_p^0. Expanding the field inside the fiber into cylindrical waves, one has $V(\mathbf{r}_s') = \sum_{m\in\mathbb{Z}} C_m^{(l,v)} g_m^J(k_s^l, \mathbf{r}_l^v)$. Substituting expressions of G and V into the integrand, the integration over D_l^v in (B.2) has a closed-form solution, and

$$\tilde{V}(\mathbf{r}) - V(\mathbf{r}) = \frac{d}{4i} \int_{-\pi/d}^{\pi/d} \sum_{(l,v)\in\mathbb{D}} \sum_{m\in\mathbb{Z}} \Phi_m^{(l,v)}(\alpha_0) C_m^{(l,v)} d\alpha_0. \tag{B.3}$$

$\Phi_m^{(l,v)}$ is the m-th column of $\Phi^{(l,v)}$, which is defined by

$$\Phi^{(l,v)} = \Gamma^{(l,v)} \mathscr{D}^4_{0,l+} \frac{\Theta_{l+} \mathscr{D}^3_{L+1,l-} \Psi_l^{-1} \Omega^{l-} + \Omega^{l+}}{\Xi_l - \Theta_{l+} \mathscr{D}^3_{L+1,l-} \Psi_l^{-1} \Theta_{l-} \mathscr{D}^2_{0,l+}} \mathbf{T}^l \mathbf{J} \tag{B.4}$$

where $\Gamma^l = \left[e^{i\left(\alpha_p(x - vd) + \beta_p^0(z - t_1)\right)} \right]$ and $\mathbf{J} = \text{diag}\left\{ k_f c J_{m+1}(k_f c) J_m(k_s c) - k_s c \cdot J_m(k_f c) J_{m+1}(k_s c) \right\}$. The integration in (B.3) is computed by numerical methods, such as QUADCC [39].

References

[1] C. Li, D. Lesselier, and Y. Zhong, "Full-wave computational model of electromagnetic scattering by arbitrarily rotated 1-D periodic multilayer structure," *IEEE Transactions on Antennas and Propagation*, vol. 64, no. 3, pp. 1047–1060, 2016.

[2] H. Heuer, M. Schulze, M. Pooch, S. Gäbler, A. Nocke, G. Bardl, C. Cherif, M. Klein, R. Kupke, R. Vetter, F. Lenz, M. Kliem, C. Bülow, J. Goyvaerts, T. Mayer, and S. Petrenz, "Review on quality assurance along the CFRP value chain – Non-destructive testing of fabrics, preforms and CFRP by HF radio wave techniques," *Composites Part B: Engineering*, vol. 77, pp. 494–501, 2015.

[3] E. G. Nesvijski, "Some aspects of ultrasonic testing of composites," *Composite Structures*, vol. 48, no. 1, pp. 151–155, 2000.

[4] S.-E. Mechraoui, A. Laksimi, and S. Benmedakhene, "Reliability of damage mechanism localisation by acoustic emission on glass/epoxy composite material plate," *Composite Structures*, vol. 94, no. 5, pp. 1483–1494, 2012.

[5] V. P. Vavilov, "Modeling and characterizing impact damage in carbon fiber composites by thermal/infrared non-destructive testing," *Composites Part B: Engineering*, vol. 61, pp. 1–10, 2014.

[6] R. Zoughi, *Microwave Non-Destructive Testing and Evaluation Principles*. Kluwer, Netherlands: Springer, 2012.

[7] C. L. Holloway, M. S. Sarto, and M. Johansson, "Analyzing carbon-fiber composite materials with equivalent-layer models," *IEEE Transactions on Electromagnetic Compatibility*, vol. 47, no. 4, pp. 833–844, 2005.

[8] Y. Zhong, M. Lambert, D. Lesselier, and X. Chen, "Electromagnetic response of anisotropic laminates to distributed sources," *IEEE Transactions on Antennas and Propagation*, vol. 62, no. 1, pp. 247–256, 2014.

[9] C. Li, *Electromagnetic modeling and simulation of fiber-reinforced periodically-structured planar laminates*. PhD thesis, University Paris-Sud, Sept. 2015, http://www.theses.fr/2015PA112219.

[10] J. Wang, B. Zhou, B. Chen, C. Gao, and L. Shi, "3D weakly conditionally stable FDTD method for analyzing periodic structures," *IEEE Transactions on Antennas and Propagation*, vol. 61, no. 7, pp. 3917–3921, 2013.

[11] J. Wang, B. Zhou, L. Shi, C. Gao, and B. Chen, "Efficiency-improved LOD-FDTD method for solving periodic structures at oblique incidence," *IEEE Microwave and Wireless Components Letters*, vol. 23, no. 10, pp. 521–523, 2013.

[12] J. Tyrus, M. Gosz, and E. DeSantiago, "A local finite element implementation for imposing periodic boundary conditions on composite micromechanical models," *International Journal of Solids and Structures*, vol. 44, no. 9, pp. 2972–2989, 2007.

[13] C. Li, D. Lesselier, and Y. Zhong, "Electromagnetic small-scale modeling of composite panels involving periodic arrays of circular fibers," *Applied Physics A*, vol. 117, no. 2, pp. 567–572, 2014.

[14] J.-P. Groby, A. Wirgin, L. De Ryck, W. Lauriks, R. Gilbert, and Y. Xu, "Acoustic response of a rigid-frame porous medium plate with a periodic set of inclusions," *The Journal of the Acoustical Society of America*, vol. 126, no. 2, pp. 685–693, 2009.

[15] K. Yasumoto, *Electromagnetic Theory and Applications for Photonic Crystals*. Boca Raton, FL, USA: CRC Press, 2005.

[16] N. B. Piller and O. J. Martin, "Increasing the performance of the coupled-dipole approximation: a spectral approach," *IEEE Transactions on Antennas and Propagation*, vol. 46, no. 8, pp. 1126–1137, 1998.

[17] Z. Liu, C. Li, D. Lesselier, and Y. Zhong, "Electromagnetic modeling of a periodic array of fibers embedded in a panel with single fiber missing," in *International Workshop on Electromagnetic Nondestructive Evaluation (ENDE)* (Y. N. *et al.*, ed.), Studies in Applied Electromagnetics and Mechanics, (Sendai), pp. 149 – 156, IOS Press, Sep. 2015.

[18] J.-P. Groby and D. Lesselier, "Localization and characterization of simple defects in finite-sized photonic crystals," *Journal of the Optical Society of America A*, vol. 25, no. 1, pp. 146–152, 2008.

[19] K. Watanabe, Y. Nakatake, and J. Pištora, "Accurate analysis of electromagnetic scattering from periodic circular cylinder array with defects," *Optics Express*, vol. 20, no. 10, pp. 10646–10657, 2012.

[20] Z. Liu, C. Li, D. Lesselier, and Y. Zhong, "Electromagnetic modeling of periodically-structured fiber-reinforced single-layer laminate with multiple fibers missing," *Applied Physics A*, vol. 122, no. 12, p. 993, 2016.

[21] Z. Liu, C. Li, D. Lesselier, and Y. Zhong, "Electromagnetic modeling of damaged single-layer fiber-reinforced laminates," *IEEE Transactions on Antennas and Propagation*, vol. 65, no. 4, pp. 1855 – 1866, 2017.

[22] L. C. Botten, N.-A. P. Nicorovici, A. A. Asatryan, R. C. McPhedran, C. M. de Sterke, and P. A. Robinson, "Formulation for electromagnetic scattering and propagation through grating stacks of metallic and dielectric cylinders for photonic crystal calculations. part II. Properties and implementation," *Journal of the Optical Society of America A*, vol. 17, no. 12, pp. 2177–2190, 2000.

[23] L. C. Botten, N.-A. P. Nicorovici, A. A. Asatryan, R. C. McPhedran, C. M. de Sterke, and P. A. Robinson, "Formulation for electromagnetic scattering and propagation through grating stacks of metallic and dielectric cylinders for photonic crystal calculations. part I. Method," *Journal of the Optical Society of America A*, vol. 17, no. 12, pp. 2165–2176, 2000.

[24] F. Capolino, D. R. Jackson, and D. R. Wilton, "Fundamental properties of the field at the interface between air and a periodic artificial material excited by a line source," *IEEE Transactions on Antennas and Propagation*, vol. 53, no. 1, pp. 91–99, 2005.

[25] S. Wilcox, L. Botten, R. McPhedran, C. Poulton, and C. M. de Sterke, "Modeling of defect modes in photonic crystals using the fictitious source superposition method," *Physical Review E*, vol. 71, no. 5, p. 056606, 2005.

[26] C. Li, D. Lesselier, and Y. Zhong, "Recursive matrix schemes for composite laminates under plane-wave and Gaussian beam illumination," *Journal of the Optical Society of America B*, vol. 32, no. 8, pp. 1539–1549, 2015.

[27] P. C. Hansen and D. P. O'Leary, "The use of the L-curve in the regularization of discrete ill-posed problems," *SIAM Journal on Scientific Computing*, vol. 14, no. 6, pp. 1487–1503, 1993.

[28] R. Schmidt, "Multiple emitter location and signal parameter estimation," *IEEE Transactions on Antennas and Propagation*, vol. 34, no. 3, pp. 276–280, 1986.

[29] S. F. Cotter, B. Rao, K. Kreutz-Delgado, and J. Adler, "Forward sequential algorithms for best basis selection," *IEE Proceedings-Vision, Image and Signal Processing*, vol. 146, no. 5, pp. 235–244, 1999.

[30] O. K. Lee, H. Kang, J. C. Ye, and M. Lim, "A non-iterative method for the electrical impedance tomography based on joint sparse recovery," *Inverse Problems*, vol. 31, no. 7, p. 075002, 2015.

[31] S. F. Cotter, B. D. Rao, K. Engan, and K. Kreutz-Delgado, "Sparse solutions to linear inverse problems with multiple measurement vectors," *IEEE Transactions on Signal Processing*, vol. 53, no. 7, pp. 2477–2488, 2005.

[32] Z. Liu, C. Li, D. Lesselier, and Y. Zhong, "Electromagnetic retrieval of missing fibers in periodic fibered laminates via sparsity concepts," in *24th European Signal Processing Conference (EUSIPCO)*, (Budapest), pp. 345–349, IEEE Xplore, Aug. 2016.

[33] W. C. Chew, *Waves and Fields in Inhomogeneous Media*. New York, NY, USA: IEEE Press, 1995.

[34] A. Oppenheim, A. Willsky, and S. Nawab, *Signals and Systems*. New Jersey, NJ, USA: Prentice Hall, 1997.

[35] K. Watanabe and Y. Nakatake, "Spectral-domain formulation of electromagnetic scattering from circular cylinders located near periodic cylinder array," *Progress In Electromagnetics Research B*, vol. 31, pp. 219–237, 2011.

[36] J. Kong, *Electromagnetic Wave Theory*. New York, NY, USA: Wiley, 1986.

[37] A. Selmi, "Void effect on carbon fiber epoxy composites," in *International Conference on Emerging Trends in Engineering and Technology (ICETET)*, (London), pp. 179–183, May 2014.

[38] P. Gonnet, "Increasing the reliability of adaptive quadrature using explicit interpolants," *ACM Transactions on Mathematical Software*, vol. 37, no. 3, p. 26, 2010.

[39] QUADCC [Online]. Available: https://fr.mathworks.com/matlabcentral/fileexchange/35489-quadcc.

[40] COMSOL, *Multiphysics Users Guide, Version 4.3*. COMSOL AB, Stockholm, Sweden, 2012.

[41] K. Yasumoto and K. Yoshitomi, "Efficient calculation of lattice sums for free-space periodic Green's function," *IEEE Transactions on Antennas and Propagation*, vol. 47, no. 6, pp. 1050–1055, 1999.

[42] R. Denlinger, Z. Gimbutas, L. Greengard, and V. Rokhlin, "A fast summation method for oscillatory lattice sums," *Journal of Mathematical Physics*, vol. 58, no. 2, p. 023511, 2017.

[43] W. C. Chew and C.-C. Lu, "The use of Huygens' equivalence principle for solving the volume integral equation of scattering," *IEEE Transactions on Antennas and Propagation*, vol. 41, no. 7, pp. 897–904, 1993.

[44] J. Yang, L.-W. Li, K. Yasumoto, and C.-H. Liang, "Two-dimensional scattering of a Gaussian beam by a periodic array of circular cylinders," *IEEE Transactions on Geoscience and Remote Sensing*, vol. 43, no. 2, pp. 280–285, 2005.

[45] C. Li, D. Lesselier, and Y. Zhong, "Full-wave model and numerical study of electromagnetic plane wave scattering by multilayered, fiber-based periodic composites," *Radio Science*, vol. 50, no. 7, pp. 688–697, 2015.

[46] B. D. Rao, K. Engan, S. F. Cotter, J. Palmer, and K. Kreutz-Delgado, "Subset selection in noise based on diversity measure minimization," *IEEE Transactions on Signal Processing*, vol. 51, no. 3, pp. 760–770, 2003.

[47] G. Rodeghiero, P.-P. Ding, Y. Zhong, M. Lambert, and D. Lesselier, "Fast calculation of electromagnetic scattering in anisotropic multilayers and its inverse problem," in *International Workshop on Electromagnetic Nondestructive Evaluation (ENDE)* (Z. *et al.*. Chen, ed.), Studies in Applied Electromagnetics and Mechanics, (Xi'an), pp. 151 – 158, IOS Press, 2015.

[48] A. Brancaccio and R. Solimene, "Fault detection in dielectric grid scatterers," *Optics express*, vol. 23, no. 7, pp. 8200–8215, 2015.

[49] A. Brancaccio, G. Leone, and R. Solimene, "Fault detection in metallic grid scattering," *JOSA A*, vol. 28, no. 12, pp. 2588–2599, 2011.

[50] P. C. Hansen, T. K. Jensen, and G. Rodriguez, "An adaptive pruning algorithm for the discrete L-curve criterion," *Journal of Computational and Applied Mathematics*, vol. 198, no. 2, pp. 483–492, 2007.

[51] R. G. Baraniuk, "Compressive sensing [lecture notes]," *IEEE Signal Processing Magazine*, vol. 24, no. 4, pp. 118–121, 2007.

[52] B. D. Rao and K. Kreutz-Delgado, "An affine scaling methodology for best basis selection," *IEEE Transactions on Signal Processing*, vol. 47, no. 1, pp. 187–200, 1999.

[53] R. Tibshirani, "Regression shrinkage and selection via the lasso," *Journal of the Royal Statistical Society. Series B (Methodological)*, pp. 267–288, 1996.

[54] Z. Liu, X. Wang, G. Zhao, G. Shi, J. Lin, and Z. Gao, "Wideband DOA estimation based on sparse representation — An extension of l_1-SVD in wideband cases," in *IEEE International Conference on Signal Processing, Communication and Computing (ICSPCC)*, (Kunming), pp. 1–4, IEEE Xplore, 2013.

[55] K. A. Michalski and J. R. Mosig, "Multilayered media Green's functions in integral equation formulations," *IEEE Transactions on Antennas and Propagation*, vol. 45, no. 3, pp. 508–519, 1997.

[56] D. Wang, E. K. N. Yung, R. S. Chen, D. Z. Ding, and W. C. Tang, "On evaluation of the Green function for periodic structures in layered media," *IEEE Antennas and Wireless Propagation Letters*, vol. 3, no. 1, pp. 133–136, 2004.

[57] R. Faggiani, A. Baron, X. Zang, L. Lalouat, S. A. Schulz, B. O'Regan, K. Vynck, B. Cluzel, F. De Fornel, T. F. Krauss, and L. Philippe, "Lower bound for the spatial extent of localized modes in photonic-crystal waveguides with small random imperfections," *Scientific Reports*, vol. 6, p. 27037, 2016.

[58] T. Weisser, J.-P. Groby, O. Dazel, F. Gaultier, E. Deckers, S. Futatsugi, and L. Monteiro, "Acoustic behavior of a rigidly backed poroelastic layer with periodic resonant inclusions by a multiple scattering approach," *The Journal of the Acoustical Society of America*, vol. 139, no. 2, pp. 617–629, 2016.

[59] B. Vial, F. Zolla, A. Nicolet, and M. Commandré, "Quasimodal expansion of electromagnetic fields in open two-dimensional structures," *Physical Review A*, vol. 89, no. 2, p. 023829, 2014.

[60] H. Ammari, E. Bonnetier, and Y. Capdeboscq, "Enhanced resolution in structured media," *SIAM Journal on Applied Mathematics*, vol. 70, no. 5, pp. 1428–1452, 2009.

[61] H. Ammari and H. Zhang, "A mathematical theory of super-resolution by using a system of sub-wavelength Helmholtz resonators," *Communications in Mathematical Physics*, vol. 337, no. 1, pp. 379–428, 2015.

Publications

JOURNAL PAPERS

Submitted and in preparation

Z. Liu, D. Lesselier, and Y. Zhong, "Electromagnetic imaging of defects in layered fiber-reinforced laminates", *IEEE Transactions on Antennas and Propagation*, in preparation.

Z. Liu, C. Li, D. Lesselier, and Y. Zhong, "Fast electromagnetic modeling of damaged layered fiber-reinforced laminates", *Journal of Computational Physics*, in preparation.

Z. Liu, C. Li, D. Lesselier, and Y. Zhong, "Fast full-wave analysis of damaged periodic fiber-reinforced laminates", *IEEE Transactions on Antennas and Propagation*, submitted.

Published

Z. Liu, C. Li, D. Lesselier, and Y. Zhong, "Electromagnetic modeling of damaged single-layer fiber- reinforced laminates", *IEEE Transactions on Antennas and Propagation*, 65(4):1855-1866, 2017.

Z. Liu, C. Li, D. Lesselier, and Y. Zhong, "Electromagnetic modeling of single-layer fiber-reinforced laminate with defects of missing fibers", *Applied Physics A*, 122(12):993, 2016.

CONFERENCE PAPERS

Oral Presentations

Z. Liu, D. Lesselier, C. Li, Y. Zhong, "Electromagnetic modeling and imaging of damaged layered fiber-based laminates", *2017 International Applied Computational Electromagnetics*

Society Symposium, ACES, Suzhou, accepted.

Z. Liu, C. Li, D. Lesselier, and Y. Zhong, "Computational modeling and imaging of damaged fibered laminates from low frequency to resonance", *22th International Workshop on Electromagnetic Non-Destructive Evaluation, ENDE,* Saclay, accepted.

Z. Liu, C. Li, D. Lesselier, and Y. Zhong, "Electromagnetic modeling and imaging of missing fibers in periodic fibered laminates", *2ème Edition des Doctoriales de la COFREND*, Marne-la-Vallée, Nov. 2016.

Z. Liu, C. Li, D. Lesselier, and Y. Zhong, "From small-scale modeling to imaging of disorganized periodic structures", *21th International Workshop on Electromagnetic Non-Destructive Evaluation, ENDE*, Lisbon, Sept. 2016.

Z. Liu, C. Li, D. Lesselier, and Y. Zhong, "Electromagnetic near-field imaging of missing fibers in periodic fiber-reinforced laminates", *Progress In Electromagnetics Research Symposium, PIERS*, Shanghai, Aug. 2016. IEEE Conf. Publ., doi: 10.1109/PIERS.2016.7735485, 3946.

Z. Liu, C. Li, D. Lesselier, and Y. Zhong, "Electromagnetic modeling of a periodic array of fibers embedded in a panel with single fiber missing", *Electromagnetic Non-Destructive Evaluation (XIX)*, Studies in Applied Electromagnetics and Mechanics, Eds. N. Yusa *et al.*, IOS Press, Amsterdam, 2016. ISBN 978-1-61499-638-5, doi: 10.3233/978-1-61499-639-2-149, 149-156.

Poster Presentations

Z. Liu, C. Li, D. Lesselier, and Y. Zhong, "Electromagnetic non-destructive testing of damaged fibered-reinforced composite laminates", *COFREND DAYS 2017*, Strasbourg, May 2017.

Z. Liu, C. Li, D. Lesselier, and Y. Zhong, "Electromagnetic modeling of fiber-reinforced single-layer laminate with multiple fibers removed", *7th International Conference on Metamaterials, Photonic Crystals and Plasmonics, META*, Torremolinos, July 2016.

Z. Liu, C. Li, D. Lesselier, and Y. Zhong, "Nondestructive testing of fiber array with multiple missing fibers", *Assemblée générale ≪ Interférences d'Ondes≫, GDR ONDES*, Lyon, Oct. 2015.

université PARIS-SACLAY
ÉCOLE DOCTORALE
Sciences et technologies de l'information et de la communication (STIC)

Titre : Modélisation électromagnétique et imagerie d'endommagements de laminés composites à renforcement de fibres

Mots clefs : modélisation électromagnétique, imagerie électromagnétique, structure périodique, contrôle non destructif

Résumé : On s'intéresse à la modélisation électromagnétique et à l'imagerie de stratifiés fibreux périodiques désorganisés. Les stratifiés ont des couches multiples et chaque couche est composée en incorporant périodiquement des fibres cylindriques dans une dalle homogène. Le matériau et la taille de la fibre peuvent changer de couche en couche, mais les périodes et les orientations sont obligées d'être identiques. Les fibres manquantes, déplacées, expansées, rétrécies et / ou circulaires détruisent la périodicité et les méthodes pour les structures périodiques deviennent inapplicables. La méthodologie Supercell fournit une structure périodique fictive, de sorte que la solution du champ partout dans l'espace peut être modélisée avec précision, à condition que la supercellule soit suffisamment grande. Cependant, l'efficacité de l'approche basée sur la supercellule n'est pas garantie en raison de la grande taille possible. Par conséquent, une approche alternative basée sur la théorie de l'équivalence est proposée, où les dommages sont équivalents à des sources dans les zones initialement intactes. Ensuite, le champ est une synthèse des réponses en raison de l'onde incidente et des sources équivalentes. Sur la base de la théorie de l'équivalence, l'emplacement des dommages se retrouve par recherche de sources équivalentes. Avec plusieurs sources et récepteurs en utilisation, quatre algorithmes de reconstruction, comprenant une solution moindres carrés, une solution "basic matching pursuit", MUSIC, et une approche itérative explorant la parcimonie conjointe de la solution désirée, permettent de récupérer les indices des fibres endommagées. Divers résultats numériques illustrent la disponibilité et la précision de l'approche de la modélisation et des performances d'imagerie haute résolution.

Title : Electromagnetic modeling and imaging of damages of fiber-reinforced composite laminates

Keywords : electromagnetic modeling, electromagnetic imaging, periodic structure, nondestructive testing

Abstract : Electromagnetic modeling and imaging of disorganized periodical fibered laminates are concerned. Laminates have multiple layers and each layer is composed by periodically embedding cylindrical fibers in a homogeneous slab. Fiber material and size might change from layer to layer, but periods and orientations are forced to be the same. Missing, displaced, expanded, shrunk fibers and/or circular inclusions destroy the periodicity and methods for periodic structures become inapplicable. Supercell methodology yields a fictitious periodic structure, so as the field solution everywhere in space can be accurately modeled, provided the supercell be large enough. However, the efficiency of supercell-based approach is not guaranteed because of the possible large size. Hence, an alternative approach based on equivalence theory is proposed, where the damages are equivalent to sources inside the initially undamaged ones. Then the field is a summation of responses due to the incident wave and equivalent sources. Based on the equivalence theory, the location of damages is found via searching of equivalent sources. With multiple sources and receivers in use, four reconstruction algorithms, including least square, basic matching pursuit, MUSIC, and an iterative approach exploring the joint sparsity of the desired solution, are used to retrieve the indexes of damaged fibers. Various numerical results illustrate the availability and accuracy of the modeling approach and high-resolution imaging performances.

Université Paris-Saclay
Espace Technologique / Immeuble Discovery
Route de l'Orme aux Merisiers RD 128 / 91190 Saint-Aubin, France